Chapter 15
Neuronal Basis of Non-Invasive Functional Imaging: From Microscopic Neurovascular Dynamics to BOLD fMRI

Anna Devor, David A. Boas, Gaute T. Einevoll, Richard B. Buxton, and Anders M. Dale

Abstract With the growing recognition of the complexity of neurovascular coupling, research has focused on the "neurovascular unit", a close association between neurons, astrocytes and blood vessels. A number of experimental tools have been developed for probing the neurovascular unit in animal models, providing the potential for a much deeper understanding of these fundamental physiological mechanisms. In this chapter, we review some of the available experimental and computational methods and present a multi-level conceptual framework for analyzing and interpreting a wide range of experimental measurements. We then discuss

A. Devor, Ph.D. (✉)
Departments of Neurosciences and Radiology, University of California San Diego, La Jolla, CA 92093-0662, USA

Martinos Center for Biomedical Imaging, Massachusetts General Hospital, Harvard Medical School, Charlestown, MA, USA
e-mail: adevor@ucsd.edu

D.A. Boas, Ph.D.
Martinos Center for Biomedical Imaging, Massachusetts General Hospital (MGH), Harvard Medical School, 13th Street Building 149, Charlestown, MA 02129, USA
e-mail: dboas@nmr.mgh.harvard.edu

G.T. Einevoll
Norwegian University of Life Sciences, Department of Mathematical Sciences and Technology, Aas, Norway
e-mail: Gaute.Einevoll@umb.no

R.B. Buxton, Ph.D.
Department of Radiology, University of California San Diego, La Jolla, CA 92093-0677, USA
e-mail: rbuxton@ucsd.edu

A.M. Dale, Ph.D.
Departments of Neurosciences and Radiology, University of California San Diego, San Diego, CA 92103-8756, USA
e-mail: amdale@ucsd.edu

I.-Y. Choi and R. Gruetter (eds.), *Neural Metabolism In Vivo*, Advances in Neurobiology 4, DOI 10.1007/978-1-4614-1788-0_15,

our working hypotheses regarding the regulation of blood flow and neurophysiological correlates of fMRI signals. Finally, we discuss how multimodal imaging, along with valid physiological models, can ultimately be used to obtain quantitative estimates of physiological parameters in health and disease and provide an outlook for the future directions in neurovascular research.

Keywords Imaging • Neurovascular • Neurometabolic • CBF • CMRO2 • LFP • CSD • MUA • fMRI • BOLD • Optical • Microscopy • Hemodynamic • Neurovascular unit • Extracellular potential • Forward modeling • Laminar population analysis

15.1 Introduction

The brain is a highly energy demanding organ, and neurovascular coupling is a critical component linking neuronal activity to blood flow and the delivery of glucose and oxygen for energy metabolism. A better characterization of these connections is important for understanding how these relationships may change with disease. In addition, understanding in a quantitative way how neuronal activity drives changes in blood flow and energy metabolism is critical for laying a solid physiological foundation for interpreting functional neuroimaging studies in humans. In particular, functional magnetic resonance imaging (fMRI) based on the blood oxygenation level dependent (BOLD) response has become a widely used tool for exploring brain function, and yet the physiological basis of this technique is still poorly understood. The primary physiological phenomenon that leads to the BOLD effect is that cerebral blood flow (CBF) increases much more than the cerebral metabolic rate of oxygen ($CMRO_2$), increasing local blood oxygenation and causing a slight increase of the MRI signal due to different magnetic properties of oxy- and deoxyhemoglobin. Although the goal of fMRI studies is usually to assess changes in neuronal activity, the signal measured depends on the relative changes in CBF and $CMRO_2$. For this reason, it is difficult to interpret the magnitude of the BOLD response as a quantitative reflection of the magnitude of the change in neuronal activity without a deeper understanding of how neuronal activity, CBF and $CMRO_2$ are connected. For example, if the BOLD responses to two tasks are different, or the response is different in disease, does that mean the underlying neuronal responses are different or that the vascular or metabolic responses are different?

The simplest picture one could imagine for this physiological coupling is that changes in neuronal activity drive changes in energy metabolism which then drive changes in blood flow. However, a large body of work over the last decade indicates that this simple picture is almost certainly wrong. While molecules produced by increased energy metabolism (CO_2, lactate, H^+, etc.) do have a vasoactive effect, much of the acute CBF response under healthy conditions appears to be driven by molecules related to neuronal signaling. In short, rather than a linear chain of events, blood flow and energy metabolism appear to be driven in parallel by neuronal activity. Because the BOLD response depends on changes in both CBF and $CMRO_2$,

a quantitative understanding of exactly which aspects of neuronal activity drive the CBF and $CMRO_2$ changes is critical for interpreting the BOLD response. For example, the primary energy cost of neuronal signaling is thought to be associated with the need to pump ions (particularly sodium) across cell membranes to restore ion gradients that are degraded in neuronal signaling. For this reason $CMRO_2$ may simply respond to the net energy cost of the evoked activity. However, if the CBF response is primarily driven by aspects of synaptic activity in a feed-forward manner, the balance of these changes, and the resulting BOLD response, could differ depending on the details of the changes in neuronal activity.

With the growing recognition of the complexity of neurovascular coupling, research has focused on the "neurovascular unit", a close association between neurons, astrocytes and blood vessels. A number of experimental tools have been developed for probing the neurovascular unit in animal models, providing the potential for a much deeper understanding of these fundamental physiological mechanisms. In this chapter, we review some of the available experimental and computational methods, discuss our working hypotheses regarding the regulation of blood flow and neurophysiological correlates of fMRI signals, and provide an outlook for the future directions in neurovascular research. Our goal is not to provide an exhaustive list of the available methodologies but rather to illustrate how multimodal data can be combined in a theoretical framework in a way where the result is greater than the sum of its parts. Along the way we offer practical guidelines for use of each one of the technologies, describe modeling approaches, and suggest references for further in-depth reading on each subject. Although the main intention is to target an audience of graduate students, the authors hope that this chapter has something to offer to each reader, whether they look for technical advice, a piece of evidence or a conceptual framework. Enjoy the reading!

15.2 Measurement Theory: Measured Parameters and Their Relationship to the Underlying Physiological Variables

Below we provide an overview of our optical and electrophysiological tools and discuss their advantages and shortcomings. The technological aspects of fMRI are described in detail in a number of other chapters in this volume, and also in publications elsewhere (Brown et al. 2007). When considering these methods, it is important to keep in mind that the signals we can measure usually are not direct measurements of the physiological quantities of interest, such as blood flow or energy metabolism. Moreover, different measurement modalities can reflect different aspects of the same physiological process. For example, an increase in neuronal activity can be measured as an increase in spike count, synaptic release, or generation of local field potential (LFP). For this reason, there is a measurement theory associated with each technique that relates the measured signals to more basic physiological quantities, indicated by the arrows in Fig. 15.1. This often involves assumptions about the physical measurements or the underlying physiology, and to use these techniques effectively it is

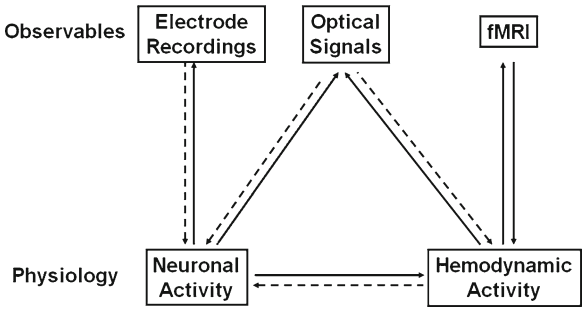

Fig. 15.1 Relationship between measurements to the underlying physiological variables. *Solid lines* indicate mappings that are "well-posed" (i.e., have a unique solution), while *dashed lines* indicate mappings that are "ill-posed" (i.e., have multiple solutions)

important to understand the assumptions and potential limitations (Dale and Halgren 2001). In addition, a recurring theme in this chapter is that the combination of two or more methods in a multi-modal imaging approach often can provide more quantitative or specific information than either technique alone. Examples are the combination of techniques sensitive to blood oxygenation changes (optical or BOLD signals) with a CBF measurement to make possible estimation of $CMRO_2$ changes (see Sect. 15.3.3.2), or measurements of spiking and synaptic response for extraction of activity of specific neuronal populations (see Sect. 15.3.2.3).

15.2.1 Optical Imaging

Optical imaging provides a versatile set of tools for studying cerebral physiology, providing measures of neuronal, metabolic, and vascular processes from the subcellular level up to the intact human brain. Although intrinsic optical changes associated with neuronal and metabolic activity have been recognized for over 50 years, Optical Intrinsic Signal Imaging (OISI) was introduced to measure functional architecture of the cortex *in vivo* only in 1986 (Grinvald et al. 1986). This technique uses a camera to image hemoglobin-induced changes in the absorption of visible light that is reflected from the cortex (either through a cranial window, thinned skull, or intact skull), and provides a spatial resolution ranging from ~10 μm on the cortical surface to hundreds of μm in cortical layers II–III. By measuring the absorption changes at multiple wavelengths of light and given knowledge of the path length of light through the tissue, it is possible to quantify absolute hemoglobin concentration changes (Kohl et al. 2000; Dunn et al. 2003). Blood flow can be imaged with Laser Speckle Contrast Imaging (LSCI) (Dunn et al. 2001; Draijer et al. 2008) by exploiting the dynamic fluctuations that moving red blood cells impose on the random interference pattern of the reflected laser light. By combining measures of blood flow and hemoglobin concentration changes, it is possible to estimate the changes in the $CMRO_2$ during brain activation (Dunn et al. 2005; Royl et al. 2008). These techniques are generally employed in animal models using invasive procedures that usually require thinning of the skull or a cranial window, and readily enable simultaneous electrophysiological measurements (Devor et al. 2003). Near Infrared

Spectroscopy (NIRS) works on a similar principle but enables the measurement of the hemoglobin concentrations through the intact skull of humans by using near infrared light (700–900 nm) (Villringer and Chance 1997; Strangman et al. 2002). The greater penetration depth arises from the fact that the near infrared light is only weakly absorbed by hemoglobin, allowing a detectable portion of the incident light to reach the brain, interrogate the hemoglobin concentrations, scatter back to the surface of the scalp, and be detected. This greater scattering, however, reduces the spatial resolution dramatically ranging from ~5 to 10 mm on the cortex of human infants to ~10–20 mm on the cortex of adult humans. NIRS can be combined with fMRI to estimate evoked changes in $CMRO_2$ (Huppert et al. 2009), and with EEG and MEG (Dale et al. 2000) to explore neurovascular coupling in humans non-invasively (Ou et al. 2009). A major limitation of all of these optical methods is a lack of laminar (i.e. depth) resolution and thus it is not possible to distinguish, e.g., superficial cortical responses from deeper cortical responses.

Significantly improved *in vivo* lateral and depth resolution of the cerebral microvascular network and the response of individual microvessels to brain activation were demonstrated in 1998 with 2-photon laser scanning microscopy (Kleinfeld et al. 1998). While 2-photon microscopy enables ~1 μm lateral and depth resolution of vessel diameter and red blood cell velocity, it is limited by a ~600 μm depth penetration. Optical Coherence Tomography (OCT) shows promise to overcome this issue by using interferometric detection to enhance detection sensitivity enabling a penetration depth of 1 mm or more and increased detection rate (Huang et al. 1991; Drexler et al. 1999). Combined with Doppler detection techniques (Leitgeb et al. 2003; White et al. 2003; Bizheva et al. 2004), it is possible to form volumetric images of red blood cell velocity spanning several cubic millimeters with ~10 μm resolution in ~10 s. This OCT methodology is being used extensively in studies of the retina (Huber et al. 2007) and is finding application in the cortex (Aguirre et al. 2006; Chen et al. 2008; Srinivasan et al. 2009; Srinivasan et al. 2010a; Srinivasan et al. 2010b). Optical imaging is used also for direct measurements of neuronal activity by employing fluorescent sensors of voltage or ionic concentrations (Tsien 1981; Miller 1988; Ross 1989; Grinvald and Hildesheim 2004; Baker et al. 2005). The most popular indicators are voltage- and calcium-sensitive dyes. While both can be applied extrinsically, significant progress has been recently made in development of genetically encoded calcium indicators with sufficient sensitivity for detection of single spikes (Wallace et al. 2008).

Below we choose to focus on a number of microscopic techniques, which have been successfully used by us and others for optical imaging of neuronal, vascular and metabolic activity.

15.2.1.1 Combined Spectral Imaging of Blood Oxygenation and Laser Speckle Imaging of Blood Flow

When OISI is performed using a number of different illumination wavelengths (referred to thereafter as “spectral” imaging), it enables estimation of changes in

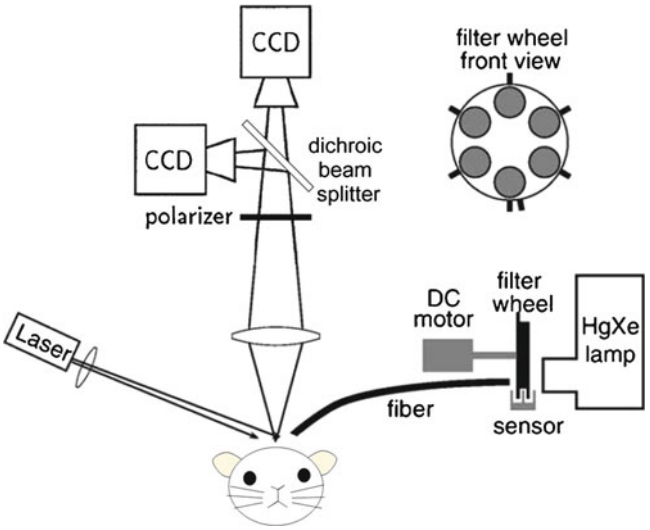

Fig. 15.2 Double-camera setup for simultaneous spectral and laser speckle measurements

oxyhemoglobin (ΔHbO), deoxyhemoglobin (ΔHb) and total hemoglobin (ΔHbT) (Devor et al. 2003; Dunn et al. 2003; Devor et al. 2005; Dunn et al. 2005; Boas et al. 2008). Spectral imaging can be combined with LSCI (referred to thereafter as "laser speckle" imaging) for concurrent 2-dimensional mapping of blood flow (Dunn et al. 2001; Bolay et al. 2002; Dunn et al. 2003; Ayata et al. 2004; Dunn et al. 2005). Simultaneous imaging of blood flow, volume and oxygenation allows for calculation of $CMRO_2$ (see Sect. 15.3.3.2 below).

During simultaneous spectral and laser speckle measurements, the detected light is split via a dichroic mirror, filtered and directed towards two dedicated detectors for imaging of blood oxygenation and speckle contrast respectively (Fig. 15.2). In our system, the filtering is achieved by passing light below 650 nm to the spectral detector, and 780 nm light (FWHM of 10 nm) to the speckle detector.

For spectral imaging n different bandpass filters ($n=6$ in our imager) are placed on a multi-position filter wheel, mounted on a DC motor. In the imager used by Dunn et al. (2003, 2005) and Devor et al. (2003, 2005, 2007, 2008b), the center wavelengths of the filters range between 560 and 610 nm at 10-nm intervals. Illuminating light from a tungsten-halogen light source (Oriel, Spectra-Physics) is directed through the filter wheel, coupled to a 12 mm fiber bundle. Images of ~6×12 mm area are acquired by a cooled 16 bit CCD camera (Cascade 512B, Photometrics). Image acquisition is triggered at ~13 Hz by individual filters in the filter wheel passing through an optic sensor. The image set at each wavelength is averaged across trials and the averaged data are converted to changes in HbO and Hb at each pixel using the modified Beer Lambert relationship:

$$\Delta A(\lambda,t) = \left(\varepsilon_{HbO}(\lambda)\Delta C_{HbO}(t) + \varepsilon_{HbR}(\lambda)\Delta C_{HbR}(t)\right)D(\lambda) \tag{15.1}$$

where $\Delta A(\lambda,t) = \log(R_o/R(t))$ is the attenuation at each wavelength, R_o and $R(t)$ are the measured reflectance intensities at baseline and time t, respectively, ΔC_{HbO} and ΔC_{Hb} are the changes in concentrations of HbO and Hb, respectively, and ε_{HbO} and ε_{Hb} are the molar extinction coefficients. This equation is solved for ΔC_{HbO} and ΔC_{Hb} using a least-squares approach. The differential pathlength factor, $D(\lambda)$, accounts for the fact that each wavelength travels slightly different pathlengths through the tissue due to the wavelength dependence of scattering and absorption in the tissue, and is estimated using the approach of Kohl et al. (2000) through Monte Carlo simulations of light propagation in tissue. Baseline concentrations of 60 μM and 40 μM are assumed for HbO and Hb, respectively (Mayhew et al. 2000; Jones et al. 2002). Dunn et al. (2005) indicates that the results for relative hemoglobin changes are only weakly sensitive to these assumed baseline values.

A laser diode (785 nm, 80 mW) is used as a light source for speckle imaging. Raw speckle images are acquired by a high-speed (~120 Hz) 8-bit CMOS camera (A602f, Basler) with an exposure time of 5 ms and in-plane resolution of ~20 μm. The speckle contrast is defined as the ratio of the standard deviation to the mean pixel intensities, $\sigma/\langle I\rangle$ within a localized region of the image (Briers 2001). Speckle contrast is calculated in a series of laser speckle images as described in Dunn et al. (2001, 2005) following spatial smoothing using 5×5 pixel sliding window (Dunn et al. 2001; Dunn et al. 2005). Numerous theoretical advances have recently been made in speckle imaging as reviewed in (Draijer et al. 2008).

Spectral imaging in the brain detects not only changes in hemoglobin oxygenation, but also other perfusion- and metabolism-related signals, including changes in cytochrome oxidation and light scattering. However, at visible wavelengths, such as within the 560–610 nm window used in our imager, the hemoglobin in blood is the most significant absorber (Frostig et al. 1990; Grinvald 1992; Narayan et al. 1994; Narayan et al. 1995; Malonek and Grinvald 1996; Nemoto et al. 1999; Vanzetta and Grinvald 1999). At longer wavelengths, at which Hb and HbO have negligible absorbance, light-scattering effects dominate.

The biggest limitation of the spectral and laser speckle imaging, common for all CCD-based optical methods, is the lack of laminar resolution. The signal at every pixel represents a weighted sum of the response though the whole depth of light penetration (with the highest sensitivity to the cortical surface) (Polimeni et al. 2005). As a result, the spatial resolution in the XY plane is somewhat ambiguous: while on the surface it is determined by the size of the CCD chip, it gradually decreases with the cortical depth due to light scattering in the tissue. One can use complementary optical methods such as OCT (Aguirre et al. 2006; Chen et al. 2008; Srinivasan et al. 2009; Srinivasan et al. 2010a; Srinivasan et al. 2010b), LOT (Hillman et al. 2004; Hillman et al. 2007) and 2-photon microscopy (Kleinfeld et al. 1998; Takano et al. 2006; Chaigneau et al. 2007; Devor et al. 2007; Devor et al. 2008b) to gain depth-resolved images.

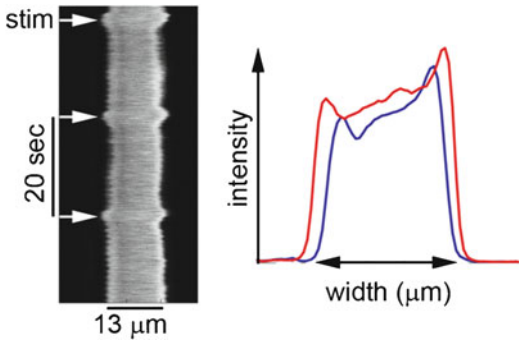

Fig. 15.3 Line-scan diameter measurement

15.2.1.2 Two-Photon Measurements of Single-Vessel Vascular Dynamics

Two-photon microscopy has been employed to image changes in diameter and velocity of blood flow in single arterioles evoked by neuronal, glial and pharmacological stimuli *in vitro* (Simard et al. 2003; Zonta et al. 2003; Cauli et al. 2004; Mulligan and MacVicar 2004; Filosa et al. 2006; Rancillac et al. 2006) and *in vivo* (Faraci and Breese 1993; Kleinfeld et al. 1998; Chaigneau et al. 2003; Kleinfeld and Griesbeck 2005; Takano et al. 2006; Chaigneau et al. 2007; Boas et al. 2008). *In vivo* the cerebral blood flow and vascular diameter changes can be imaged from the cortical surface to as deep as 600 μm below the pia mater of the cortex – down to layer IV in rat cerebral cortex (Kleinfeld et al. 1998). To visualize the vasculature and to track movement of red blood cells (RBCs), dextran-conjugated fluorescent dyes (such as fluorescein or Texas Red) are injected intravenously. In our practice, a 4x air objective (Olympus XLFluor4x/340, NA = 0.28) is used to obtain images of the surface vasculature across the entire cranial window to aid in navigating in the XY-plane. 10x (Zeiss Achroplan, NA = 0.3), Super20x (Olympus, NA = 0.95) and 40x (Olympus, NA = 0.8) water-immersion objectives are used for subsequent high-resolution imaging and line-scan measurements of vessel diameter and RBC velocity.

Measurements of vessel diameter. Absolute vessel diameter is measured by obtaining a planar image stack, or by using continuous line scans to gauge rapid changes over time (Fig. 15.3). The diameter changes are captured by repeated line scans across the vessel that form a space-time image when stacked sequentially (Fig. 15.3, *left*). Diameters are extracted from profile changes (Fig. 15.3, *right*: compare blue (*baseline*) to *red* (*peak dilation*)). By scanning longer distances across multiple vessels, or when using advanced scanning algorithms (Gobel et al. 2007), one can obtain the diameter changes of multiple vessels in a single space-time image. In this case, the scanning direction may not always be perpendicular to the vessel axis for each of the measured vessels when using this approach. However, the fractional diameter change is unaffected and the absolute diameter D can be obtained by $D = D_m \sin\theta$, where D_m is the measured diameter, and θ is the angle between the scan

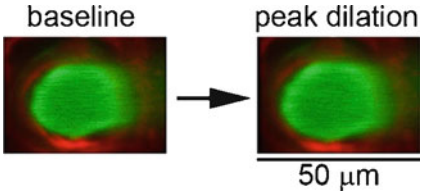

Fig. 15.4 Frame-scan diameter measurement. Intravascular lumen and astrocytic endfeet are in green and red, respectively

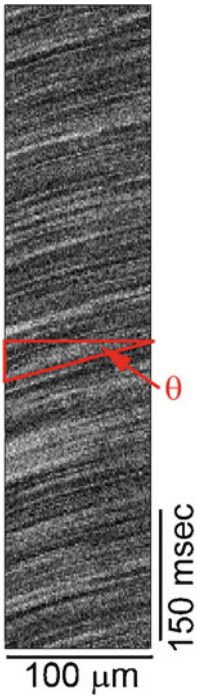

Fig. 15.5 Measurement of RBC velocity

line and the axis of the vessel. In practice, when scanning in a single plane, the number of simultaneously measured vessels is limited to vessels in focus. The diameter can also be estimated from the image time series of a diving vessel obtained in a frame scanning mode by counting the number of pixels above a pre-set intensity threshold (Fig. 15.4). A scan rate of 150 Hz or video-rate frame mode while maintaining diffraction limited spatial resolution is sufficient to capture relatively slow diameter changes.

Measurements of RBC velocity. Intravenously injected dextran-conjugated fluorescent dyes label the plasma leaving RBCs visible as dark shadows on bright fluorescent background (Fig. 15.5). The speed of the RBCs is captured by repeated line scans along the axis of the vessel that form a space-time image when stacked sequentially and leads to the generation of streaks caused by the motion of RBCs. High scan rate (above 1 KHz) is required for capturing of fast arterial flow. The speed of RBCs is given by the reciprocal of the slope of these streaks and the direction

of flow is determined from the sign of the slope (Fig. 15.4, velocity = $1/\tan\theta$). An algorithm based on singular value decomposition is used to automate the calculation of speed from the line-scan data (Kleinfeld et al. 1998). Given both measurements of diameter and velocity one can calculate flux (number of RBCs per second) (Devor et al. 2008a) that might have a more direct relationship to the MRI pulsed Arterial Spin Labeling (ASL) measure of blood flow (Brown et al. 2007).

15.2.1.3 Optical Coherence Tomography (OCT)

OCT is an important clinically established biomedical imaging modality that uses broadband near-infrared light to provide depth-resolved, cross-sectional images of tissue to depths > 1 mm and with resolutions in the range of 1–10 μm (Huang et al. 1991; Drexler et al. 1999). With OCT, the light source is split into two beams. One of the beams of light travels through the sample arm and is focused into the tissue by a lens similar to 2-photon microscopy but generally with a smaller numerical aperture. This light is scattered as it travels deeper into the tissue and a portion of this scattered light is collected by the focusing lens. In parallel, the other beam of light travels an equivalent path length in the reference arm but is reflected by a mirror. The light reflected back in the reference arm and the sample arm are mixed and produce an interference pattern. The OCT signal is derived from the interference fringes. This heterodyne method used in OCT allows detection of signals smaller than one part in 10^{-10}, or −100 dB. Such exquisite sensitivity allows deeper imaging than multi-photon microscopy and suggests that OCT may be sensitive to weak changes in scattered light associated with functional activation in the cortex. Depth resolution is achieved by using a broadband light source that has a coherence length on the order of 1–10 μm. When the light has a short coherence length, the interference between the sample and reference arms occurs only when the path length of light in each arm is matched. Thus, by varying the path length of the reference arm, it is possible to probe the amount of light scattered at different depths in the sample with a depth resolution given by the coherence length. This is the classical time-domain OCT that required a moving mirror in the reference arm. Recently, spectral (White et al. 2003; Wojtkowski et al. 2003) and frequency (Leitgeb et al. 2003; Vakoc et al. 2005) domain OCT methodology were introduced that do not require moving parts or a time varying delay line and thus enable up to 100x faster signal acquisition.

This only gives signal along the axis of the optical beam. A small numerical aperture is used to maintain a small lateral profile of the beam over a long axial distance of 500–1,000 μm. A higher numerical aperture would give a lateral resolution of ~1 μm but then the signal could only be acquired over a few micrometers in the axial direction. Cross-sectional images are generated by scanning the optical beam across the tissue in the same fashion that 2-photon microscopy generates images. If the scattering particle in the tissue is moving, such as RBCs, then the scattered light has a Doppler frequency shift that can be detected as a phase shift versus time thus enabling Doppler OCT to image RBC velocity (Leitgeb et al. 2003;

White et al. 2003; Bizheva et al. 2004). Overall, OCT imaging is analogous to ultrasound B-mode imaging, except that it uses light rather than acoustical waves.

Few studies exist to date using OCT imaging to study functional activation in neuronal tissues. Maheswari et al. showed depth resolved stimulus specific profiles of slow processes during functional activation in the cat visual cortex (Maheswari et al. 2003). They attributed these signals to variation in scattering due to localized structural changes such as capillary dilation and cell swelling. This was further supported by recent studies from our group which showed spatial and temporal agreement between the evoked OCT signal changes and the multi-spectral images of hemoglobin changes (Aguirre et al. 2006; Chen et al. 2008). Further, Chen et al. observed a delay in the OCT signal at superficial depths relative to the multi-spectral hemoglobin changes suggestive of retrograde vasodilation (Chen et al. 2008). Evoked scattering changes can be observed also on a fast scale corresponding to propagation of action potentials (Lazebnik et al. 2003; Akkin et al. 2004; Fang-Yen et al. 2004). These and other studies have generated tremendous recent interest in OCT as a potential tool for imaging of both fast and slow functional signals of neuronal and vascular origins.

15.2.1.4 Optical Imaging of pO_2

A recent optical approach exploits O_2-dependent quenching of a phosphorescence molecule for the *in vivo* imaging of O_2 content in living tissue (Dunphy et al. 2002; Smith et al. 2002). The technique is attractive because the calibration between the phosphorescent lifetime and the partial pressure of oxygen (pO_2) is absolute (Dunphy et al. 2002), and it can be applied to measure both intravascular and tissue oxygenation. To obtain local measures of pO_2, the phosphorescence molecule must be introduced into the blood stream or into the tissue. A pulse of light is introduced into the tissue at the appropriate wavelength to excite an electron out of the ground state of the phosphorescent molecule. The excited state electron transitions into a triplet state that has a "forbidden" transition back to the ground state that can take from one to hundreds of microseconds (depending on the molecule), releasing a red-shifted phosphorescent photon in the process. Measuring these phosphorescent photons reveals an exponential decay profile described by a single lifetime. This long lifetime increases the probability of collisions between molecular oxygen and the excited phosphorescent molecule providing a non-radiative decay pathway. The longer the electron stays in the excited state, the greater the probability of it decaying non-radiatively. Thus, oxygen has the effect of decreasing the apparent lifetime of the phosphorescent decay. A greater concentration of oxygen increases the probability of collisions and thus further decreases the phosphorescent lifetime. The lifetime relationship with the partial pressure of oxygen follows the Stern-Volmer relation,

$$\frac{\tau_o}{\tau} = 1 + k\tau_o \, pO_2 \tag{15.2}$$

where τ and τ_o is the phosphorescent lifetime at a particular partial pressure of oxygen pO_2 and at $pO_2=0$ respectively, and k is the second-order rate constant related to the frequency of collisions of the excited-state phosphor with molecular oxygen.

Intravascular imaging of pO_2 can be performed with a thermoelectrically cooled CCD camera (Sakadzic et al. 2009) or using confocal imaging (Yaseen et al. 2009). The camera frame rate is synchronized with the triggering rate of the pulsed laser used for excitation of phosphorescence. The light is collected by the low magnification infinity corrected objective (e.g., Olympus XL Fluor 4x/340, 0.28 NA) and an image is created on the CCD sensor by a 100 mm focal length tube lens. Ambient light and phosphorescence excitation light are suppressed with a 650 nm high pass filter. The light from the pulsed laser is coupled into the multimode fiber and typically 5–10 mJ/cm^2 is delivered to the brain tissue at an angle with respect to the cranial window surface. For estimation of phosphorescence lifetimes, 4×4 binning of the CCD pixels is used and the CCD exposure time is set to 50 μs. A sequence of 25 frames is acquired with variable delay times with respect to the laser Q-switch opening. The first frame (200 μs before the laser pulse) is used to subtract the background light from the phosphorescence intensity images, and the delays of the remaining 24 frames are divided into three groups: initial 10 acquisitions with 5 μs increments in delay following the laser pulse, followed by 10 acquisitions with 20 μs increments in delay and four acquisitions with 400 μs increments in delay (Sakadzic et al. 2009). In addition to single photon excitation of O_2-sensitive probes, 2-photon excitation is now being employed to achieve better depth penetration and higher spatial localization (Mik et al. 2004; Finikova et al. 2008).

Oxygenation data alone cannot be used to infer $CMRO_2$, because a mere increase in blood flow without a concurrent increase in local O_2 metabolism would raise O_2 concentration in the tissue and blood. However, $CMRO_2$ can be calculated given simultaneous measurements of flow and oxygenation. For example, $CMRO_2$ can be calculated by combining phosphorescence lifetime imaging with laser speckle imaging (Fig. 15.6) (Sakadzic et al. 2009). $CMRO_2$ can also be calculated from simultaneous spectral and laser speckle imaging (Dunn et al. 2003; Dunn et al. 2005), or (on a more macroscopic scale) from interleaved BOLD and ASL fMRI (Brown et al. 2007). In future simultaneous 2-photon imaging of intravascular and tissue pO_2 would allow direct measurements the pO_2 gradient as a function of the depth and distance to the closest capillary, arteriole or venule, and calculation of the microscopic distribution of $CMRO_2$.

15.2.1.5 Optical Imaging of NADH Intrinsic Fluorescence

Optical imaging of intrinsic β-nicotinamide adenine dinucleotide (NADH) tissue fluorescence has drawn some attention in recent years, motivated by the early work of Britton Chance and colleagues (Chance et al. 1962). NADH is the principal electron carrier in glycolysis, the Krebs cycle and the mitochondrial respiratory chain. NADH is generated during glycolysis in the cytosol, shuttled to mitochondria (directly or via electron shuttles) and subsequently oxidized to NAD^+ in the electron

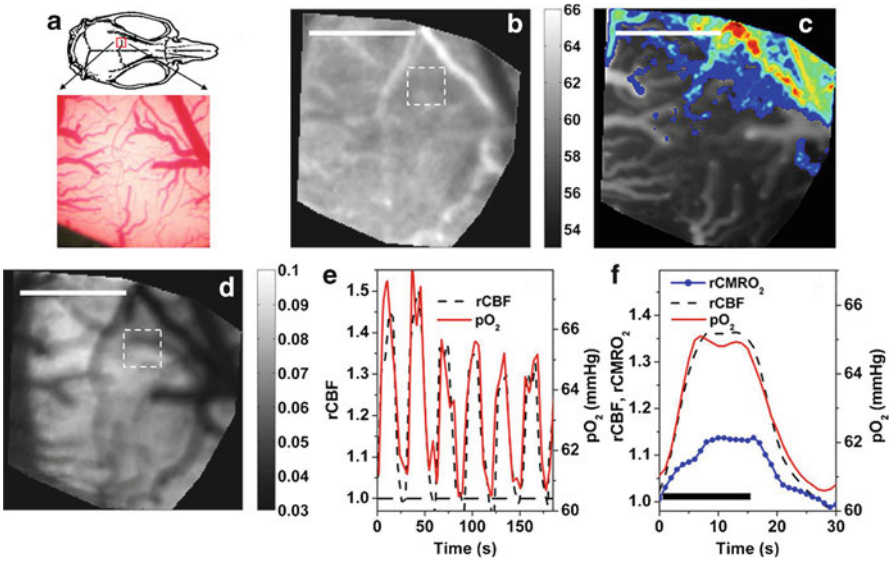

Fig. 15.6 Imaging of pO_2 by measuring the phosphorescence lifetime of an oxygen-sensitive probe Oxyphor R2 during forepaw stimulation. (**a**) Position of the cranial window and photograph of the cortical vasculature. (**b**) Baseline pO_2 map. (**c**) Composite image consisting of phosphorescence intensity (*gray*) and the functional CBF response (*color*). (**d**) Speckle contrast image of baseline flow. (**e**) Time-courses of pO_2 (*red solid curve*) and rCBF (*black dashed curve*) during several stimulation sequences. Both pO_2 and rCBF values were averaged over the area marked by rectangles in (**b**) and (**d**). (**f**) Average pO_2, rCBF, and calculated $rCMRO_2$ averaged over six stimulation trials. Duration of the stimulus is marked by the black horizontal bars in (**e**) and (**f**) Scale bar is 1 mm (Reproduced with permission from (Sakadzic et al. 2009))

transport chain, establishing a potential across the inner mitochondrial membrane, enabling the production of ATP. In mitochondria, the oxidation is followed by regeneration of NADH from NAD^+ during the TCA cycle. In the cytosol, conversion of pyruvate into lactate (with a subsequent secretion of lactate into the extracellular space) decreases the NADH pool but on a slower time scale (Hu and Wilson 1997). Thus, although a close correlation between NADH oxidation and oxygen consumption has been reported (see (Turner et al. 2007) for a recent review), interpretation of the ratio of NADH/NAD^+ can be complex, depending on the balance of $CMRO_2$ and non-oxidative glycolysis.

Since NADH is auto-fluorescent while NAD^+ is not, intrinsic NADH fluorescence serves as an indicator of the cellular redox state. Previous studies *in vivo* established that on a macroscopic level NADH auto-fluorescence of brain tissue decreases in response to stimulation, cortical spreading depression or seizures throughout the duration of the stimulus as far as blood flow is not compromised, and increases in response to hypoxia or ischemia. A recent 2-photon microscopy study in a hippocampal brain slice revealed that astrocytes have a higher resting NADH fluorescence than neurons and respond to stimulation of Schaffer collaterals with an

increase in NADH signal (Kasischke et al. 2004). However, NADH behavior *in vitro* might differ from *in vivo* because of the limited O_2 availability in absence blood flow and O_2 carriers (Devor et al. 2009). Future 2-photon studies are required to establish metabolic imaging biomarkers on a single cell level *in vivo*.

15.2.1.6 Voltage-Sensitive Dyes Imaging

Voltage-sensitive dyes (VSD) imaging provides a unique tool for visualizing real-time neuronal activity in space and time (Cohen and Lesher 1986; Grinvald et al. 1988). The dye molecules bind to the external surface of the excitable membranes of neurons and act as molecular transducers that transform changes in membrane potential into optical signals. Following a stimulus, but also during the spontaneous neuronal activity, there is a change in membrane potential in excitable brain tissue that produces a change in the absorption or the emitted fluorescence of the dye. The optical signal represents a spatial integral of membrane potentials over all membranes in a given area. Since dendritic arborizations constitute a large percentage of the total membrane area, voltage-sensitive dye signals reflect potential changes that result mostly from synaptic activity (Ebner and Chen 1995; Ferezou et al. 2006). In common practice, a well is built around a cortical exposure and filled with the dye solution. The dye is left for 1–1.5 h to impregnate the brain. Next, the staining solution in the well is replaced multiple times with fresh buffered saline to remove any unbound dye molecules, and the well is sealed. The cortex is illuminated using an epi-illumination system with appropriate excitation and emission filters (e.g., 630 and 665 nm respectively, using RH 1691) and a dichroic mirror. Fluorescent images are acquired using a cooled CCD camera usually at 200 Hz or above.

Respiration and heartbeat represent dominant sources of noise in VSD imaging experiments (Shoham et al. 1999). Bleaching and photodynamic damage provide an additional constraint for the number of trials that can be acquired to improve the single-to-noise ratio (SNR). To reduce the noise from breathing and heart pulsation, the data acquisition is usually synchronized with ventilation and electrocardiogram, with a subsequent subtraction of blank (no stimulus) trials.

Similar to optical imaging of intrinsic signals, voltage-sensitive optical measurements are done from the cortical surface and do not posses laminar (depth) resolution. The signal at every pixel represents an integral of the response though the whole depth of light penetration. It has been demonstrated that dyes RH-1691, RH-1692, and RH-1838 stain the cortex to a depth of at least 1 mm (Shoham et al. 1999).

15.2.2 Laminar Electrophysiological Recordings

Although VSD and fluorescent ionic indicators, such as calcium-sensitive dyes, become increasingly popular, electrophysiological recordings are still considered "the gold standard" for measurements of neuronal activity. Most of the recordings *in vivo* are performed using extracellular metal or glass microelectrodes.

Electrophysiological recordings with extracellular microelectrodes or microelectrode arrays measure electrical potentials with respect to a distant site – usually a reference electrode that is attached to the skull. In this configuration, the measured potential reflects spikes of multiple neurons superimposed on other lower frequency waves related mostly to synaptic activity. The spiking (multiple unit activity, MUA) and synaptic (local field potential, LFP) activity can be separated by high- and low-pass filtering, respectively. This separation is based on the fact that spikes are fast events lasting ~ 1 ms, whereas synaptic potentials typically range from 10 to 100 ms.

Intracellular recording from single cells can be made *in vivo* using either "sharp" or "patch" configurations. In contrast to extracellular recordings that usually sample many cells in the neighborhood of the electrode tip, intracellular recordings are made from one cell at a time. Until recently, these recordings could not be targeted to a particular cell type, which made studies of infrequent cell types very difficult. Recently, a new approach has been described that uses 2-photon microscopy and cell-type-specific labeling to guide patch electrodes to specific cells - "2-photon guided patch" (Margrie et al. 2003). In principle, this method can be combined with other 2-photon measurements such as measurements of vascular diameters and RBC velocity.

Whereas intracellular recordings provide the ultimate single-cell resolution, they are impractical for estimation of population activity and reconstruction of circuit dynamics. For that reason, MUA and LFP measurements have been extensively employed in studies of neurovascular coupling. However, a growing body of recent data reviewed below (see Sect. 15.4.1) increasingly suggest that cell-type specific release of vascular mediator can play a central role in regulation of blood flow. These data emphasize the need for computational methods for extraction of cell type-specific activity from MUA and LFP that can be validated through intracellular recordings.

The cortical column can be considered as a processing unit of the cerebral cortex (Simons 1978). However, within a given column, processing is organized according to cortical lamina. Different cortical layers contain distinct neuronal types, and cortical connections in different areas have characteristic laminar origins and terminations (Thomson and Bannister 2003). Therefore, depth-resolved (laminar) recordings increase our ability to extract more detailed information on the activity within the cortical circuit. To obtain a laminar depth profile, one can record sequentially, inserting one microelectrode at different depths. However, this method is time-consuming and inevitably inaccurate due to elastic properties of the cortical tissue. An alternative is to use a one-dimentional multielectrode array with multiple contacts spaced at equal intervals (Fig. 15.7) (Ulbert et al. 2001; Devor et al. 2003). Using multielectrode arrays, simultaneous measurements of MUA and LFP are made throughout the entire cortical depth. The depth is estimated based on the contact number when the top contact is positioned at the cortical surface using visual control. In our practice, the recorded potential is amplified and filtered into two signals: a low-frequency LFP part (0.1–500 Hz, sampled at 2 kHz with 16 bits) and a high-frequency MUA part (150–5,000 Hz, sampled at 20 kHz with 12 bits), see (Ulbert et al. 2001) for details. MUA is further digitally bandpass filtered between 750 Hz and 5,000 Hz using a zero phase-shift second order Butterworth filter, and then rectified to provide the MUA. The MUA data is usually smoothed along the time axis using a Gaussian kernel of 1 ms full width at 1/e of peak amplitude. Dense mapping using extracellular

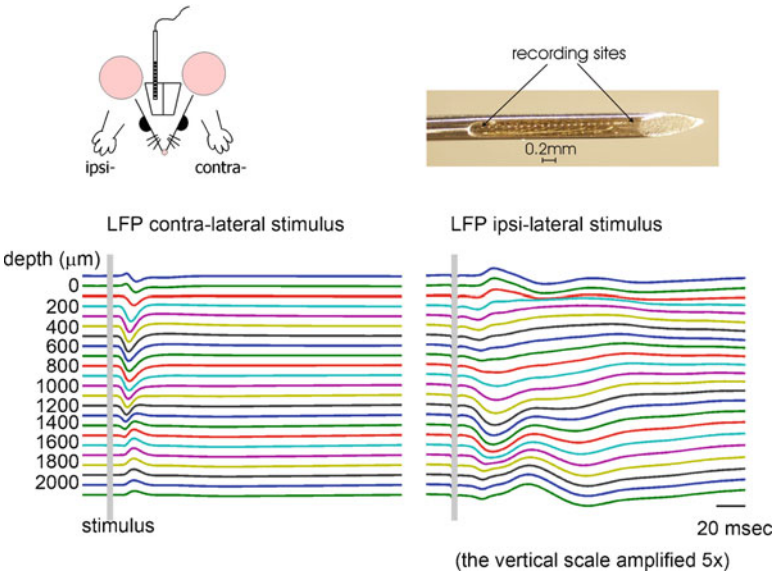

Fig. 15.7 Laminar recordings of LFP in response to contra- and ipsilateral forepaw stimulation

microelectrodes (2–4 MΩ, FHC) is performed prior to insertion of the array to determine the location of the maximal neuronal response.

The size of the laminar electrode (diameter = 300 μm in Ulbert et al. (2001)) is comparable to the size of a cortical column. However, recordings using a laminar electrode and sequential recordings using a single microelectrode at different penetration depths yielded similar results (Rappelsberger et al. 1981). Due to different spatial sensitivity of the recording of spikes and synaptic potentials, LFP signals are recorded from a bigger area. Specifically, MUA represents a weighted sum of the extracellular action potentials of neurons within a sphere of ~ 100 μm radius (Buzsaki 2004; Somogyvari et al. 2005; Pettersen and Einevoll 2008; Pettersen et al. 2008), with the electrode in the center. LFP, on the other hand, appears to reflect a weighted average of dendro-somatic components of synaptic signals of a neuronal population within a few hundred micrometers or more of the electrode tip (Pettersen et al. 2008).

15.3 Modeling Approaches

Our general conceptual framework for modeling the relationship between physiological variables and imaging observables (forward models), as well as the coupling between physiological variables (physiological models) is illustrated in Fig. 15.8. In this framework, spiking activity of each neuronal population is associated with two parallel processes: release of vasoactive messenger molecules and energy metabolism

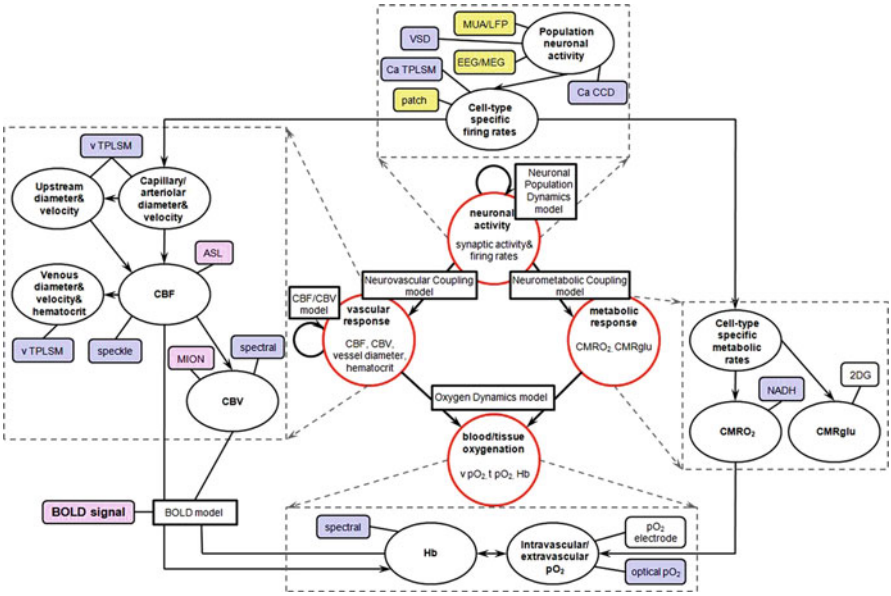

Fig. 15.8 Theoretical framework. Experimental observables are indicated by rounded rectangles (*yellow for electrophysiological; blue for optical; pink for MR-based*). The physiological parameters of interest are indicated by black ovals, and the relationships between physiological variables and observables are indicated by arrows. The computational models, linking physiological parameters and measurements, are indicated by black rectangles. vTPLSM and Ca TPLSM stand for 2-photon laser scanning microscopy measurements of vascular diameters/velocities and calcium indicators, respectively. CBV, cerebral blood volume; MION, MRI contrast agent monocrystalline iron oxide nanocolloid used for measuring of CBV; CMRglu, cerebral metabolic rate of glucose; v pO_2, intravascular pO_2; t pO_2, tissue pO_2; Hb, deoxyhemoglobin

(Neurovascular and Neurometabolic Coupling models). The resulting vascular and metabolic response then lead to spatiotemporal changes in blood flow, volume and oxygenation, as specified by the Oxygen Dynamics model. In the following, we introduce a mathematical modeling framework that is used to capture the relationship between the physiological variables, and show how the physiological parameters can be estimated from the experimental observables.

15.3.1 Multi-modality Integration: A Bayesian Modeling Framework

A key goal of multi-modality integration is to derive estimates of unknown physiological variables with the greatest possible spatial and temporal accuracy, by exploiting the relative strengths of different imaging modalities. Bayesian estimation provides a convenient and general mathematical framework for formulating this

integration problem. Specifically, we aim to estimate the spatiotemporal behavior of various electrophysiological variables ('$\boldsymbol{\beta}_E(\mathbf{r},t)$' : [membrane potential, action potentials, trans-synaptic currents]), metabolic variables ('$\boldsymbol{\beta}_M(\mathbf{r},t)$' : [$CMRO_2$]), and vascular/hemodynamic variables ('$\boldsymbol{\beta}_H(\mathbf{r},t)$' : [vessel diameters, flow, volume, oxygen concentration]), from a given set of experimental observables. The relevant observables are **electric/magnetic:** '$\mathbf{Y}_{EM}(\mathbf{r},t)$' = [MUA, LFP, EEG, MEG]; **optical:** '$\mathbf{Y}_{OPT}(\mathbf{r},t)$' = [spectral/speckle, NIRS]; and **magnetic resonance**: '$\mathbf{Y}_{MRI}(\mathbf{r},t)$' = [BOLD, ASL, MION]). These observables reflect the electrical ('$\boldsymbol{\beta}_E(\mathbf{r},t)$'), metabolic ('$\boldsymbol{\beta}_M(\mathbf{r},t)$') and hemodynamic ('$\boldsymbol{\beta}_H(\mathbf{r},t)$') state of the brain at time 't' and location '$\mathbf{r}$' in the brain. Using Bayes' Rule, assuming independent noise processes for the different observables ($\mathbf{Y}_{EM}$, $\mathbf{Y}_{OPT}$, $\mathbf{Y}_{MRI}$), and assuming that $\mathbf{Y}_{EM}$ reflect only electrophysiological parameters, and $\mathbf{Y}_{OPT}$, $\mathbf{Y}_{MRI}$ reflect only hemodynamic and metabolic variables, we get

$$P(\beta_E,\beta_M,\beta_H|\mathbf{Y}_{EM},\mathbf{Y}_{OPT},\mathbf{Y}_{MRI}) \propto P(\mathbf{Y}_{EM}|\beta_E)\bullet P(\mathbf{Y}_{OPT}|\beta_M,\beta_H)\bullet P(\mathbf{Y}_{MRI}|\beta_M,\beta_H)\bullet P(\beta_M,\beta_H|\beta_E)\bullet P(\beta_E) \tag{15.3}$$

The left hand side of this equation represents the *a posteriori* probability of the physiological parameters $\boldsymbol{\beta}_E(\mathbf{r},t)$, $\boldsymbol{\beta}_M(\mathbf{r},t)$,and $\boldsymbol{\beta}_H(\mathbf{r},t)$, given all observables '$\mathbf{Y}_i(\mathbf{r},t)$', as well as *a priori* information, from which the *maximum a posteriori probability* (MAP) estimates and confidence intervals for the electrical variables of interest can be obtained (Schmidt et al. 1999; Dale and Halgren 2001; Friston 2005). The term $P(\mathbf{Y}_{EM}|\boldsymbol{\beta}_E)$ represents the forward solution for the electric/magnetic observables, given the electrophysiological parameters. The *a priori* information about the electrophysiological parameters are encoded in $P(\boldsymbol{\beta}_E)$, reflecting the coupling between these parameters (captured by the Neuronal Population Dynamics model in Fig. 15.8). The mathematical relationship between the electric/magnetic observables and electrophysiological parameters is developed in more detail in Sect. 15.3.2, below.

The term $P(\boldsymbol{\beta}_M,\boldsymbol{\beta}_H|\boldsymbol{\beta}_E)$ reflects the coupling between electrophysiological activity (e.g., firing and/or synaptic activity of specific cell types), and hemodynamic and metabolic parameters (e.g., $CMRO_2$ and arteriolar dilation; captured by the Neurovascular Coupling, Neurometabolic Coupling, and Oxygen Dynamics models in Fig. 15.8). The terms $P(\mathbf{Y}_{OPT} \mid \boldsymbol{\beta}_M, \boldsymbol{\beta}_H)$ and $P(\mathbf{Y}_{MRI} \mid \boldsymbol{\beta}_M,\boldsymbol{\beta}_H)$ represent the optical and MRI forward solutions, respectively. Characterization of these functions, for the measurement modalities and physiological parameters of interest, is detailed in Sect. 15.3.3, below.

15.3.2 Modeling of Neuronal Populations from Laminar Microelectrode Recordings

15.3.2.1 Forward Modeling of Extracellular Potentials

The potentials recorded by extracellular electrodes stem from the ionic electrical currents going through the membranes of neurons and other cells in the vicinity of the electrode contacts. These transmembrane currents force small electrical currents

to be driven through the low-resistance extracellular medium which, following Ohms electrical circuit law, lead to spatial variations in the extracellular potential. The low resistance of the extracellular medium implies that the extracellular potential differences will be small, typically less than a millivolt, i.e., much smaller than the typical neuronal membrane potentials of about 70 mV.

The extracellular potentials generated by transmembrane currents can be calculated using *volume conductor theory* (Nunez and Srinivasan 2006). Here the extracellular medium is envisioned as smooth and continuous and transmembrane currents entering and leaving the extracellular space are represented as *volume current sources*. The fundamental relationship between the extracellular potential φ recorded at a position $\boldsymbol{r}$ due to a transmembrane current I_0 at a position $\boldsymbol{r}_0$ is given by (Hämäläinen et al. 1993; Nunez and Srinivasan 2006)

$$\varphi(\boldsymbol{r},t) = \frac{1}{4\pi\theta}\frac{I_0(t)}{|\boldsymbol{r}-\boldsymbol{r}_0|}. \tag{15.4}$$

Here $\boldsymbol{r}$ and $\boldsymbol{r}_0$ are position *vectors*, σ is the *extracellular conductivity*, and the extracellular potential φ is chosen to be zero infinitely far away from the transmembrane current.

Several assumptions lie behind this simple formula, in particular the *quasistatic approximation of Maxwell's equations*. This approximation amounts to omitting time derivatives of the electric and magnetic fields from the original Maxwell's equations. Then the electric field $\boldsymbol{E}$ in the extracellular medium is related to the extracellular potential φ via $\boldsymbol{E} = -\nabla\varphi$. For frequencies inherent in neuronal activity, i.e., less than a few thousand hertz, the quasistatic approximation seems to be well fulfilled (Hämäläinen et al. 1993). Assumptions have also been made about the electrical properties of the extracellular medium: The current density $\boldsymbol{j}$ is assumed to be proportional to the electrical field, i.e., $\boldsymbol{j} = \sigma\boldsymbol{E}$. Further, the extracellular conductivity is assumed to be purely ohmic, i.e., σ has no imaginary part from capacitive effects (Nunez and Srinivasan 2006; Logothetis et al. 2007). Finally, the formula assumes σ to be the same everywhere and also the same in all directions (Logothetis et al. 2007). More discussion on these assumptions, and also ways of generalizing Eq. 15.4 when they do not apply, can be found in (Pettersen et al. 2012).

The formula in Eq. 15.4 forms the basis for so called *forward modeling* of extracellular potentials, i.e., it describes how a transmembrane current due to neuronal activity contributes to this potential. A convenient feature of the forward-modeling scheme is that due to the linearity of Maxwell's equations, the contributions to the extracellular potential from the various neuronal sources add up linearly. Thus the net extracellular potential from activity in an entire neuron can be found simply by adding contributions of the form in Eq. 15.4 from transmembrane currents from all parts of the neuron. In general, compartmental modeling, using simulation tools like NEURON (Carnevale and Hines 2006) and Genesis (Bower and Beeman 1998), must be used to calculate the transmembrane currents acting as sources for the extracellular potential. However, if all transmembrane currents and their spatial positions are known, the extracellular potential can in principle be computed at any point.

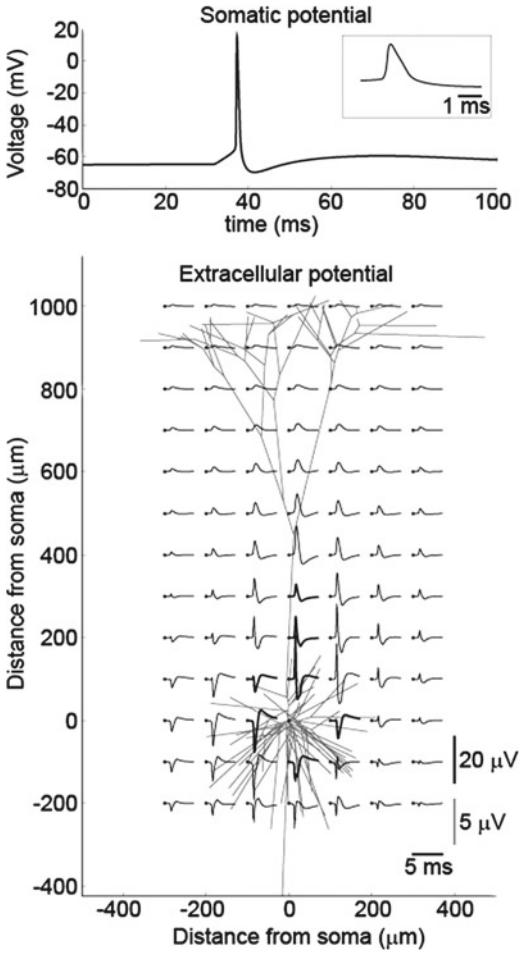

Fig. 15.9 Intracellularly and extracellularly recorded action potentials. The model is a reconstructed pyramidal neuron taken from Mainen and Sejnowski (1996). A synaptic stimuli similar to what is called "stimulus input pattern 1" in Pettersen et al. (2008) is used. Top panel: Membrane potential in soma during an action potential. Inset shows the membrane potential trace in a 5 ms time window around the action potential. Lower panel: Calculated extracellular potentials based on a variant of the forward-modeling formula in Eq. 15.4 assuming an isotropic, homogenous and purely conductive extracellular medium with $\sigma = 0.3$ S/m. The extracellular potentials are shown for the same 5 ms as in the membrane potential inset in the top panel. All distances are in micrometers

In Fig. 15.9 we illustrate this forward-modeling scheme by showing the calculated extracellular potential for a compartmental neuron model firing an action potential. The top panel shows a characteristic membrane potential trace for an action potential calculated by the simulation tool NEURON using a model pyramidal neuron constructed by Mainen and Sejnowski (Mainen and Sejnowski 1996). This neuron model has several types of active ion channels spread across the neuronal membrane, and the membrane potential trace has a characteristic shape with a fast depolarization followed by an almost equally fast repolarization, and eventually a longer after-hyperpolarization. The corresponding calculated extracellular spike pattern is shown at different positions in the lower panel. These extracellular potentials are found from evaluating a sum over numerous terms (one for each compartment) of the type in Eq. 15.4 where $I_0(t)$ corresponds to transmembrane currents found for each compartment in the NEURON simulation (see (Pettersen et al. 2008)

for details). Several features are noteworthy. The extracellular spike has a much lower amplitude than the intracellular action potential. Even close to the soma the amplitude is less than a few tens of microvolts, more than a factor thousand smaller than the intracellular amplitude. Also, the magnitude of the extracellular spike decays rapidly with distance from the neuronal soma. Moreover, not only the size, but also the shape of the extracellular potential vary significantly with position: for example, the shape around the apical (upper) dendrites is typically inverted compared to around the basal (lower) dendrites, and the spikes further away from the soma are generally less sharp. The example in Fig. 15.9 demonstrates that *positive and negative phases of extracellular potentials, such as LFP, cannot be treated as excitation and inhibition* – the sign of the potential changes depending on the location of the recording relative to the activated neuronal population.

Due to the linearity of the forward-modeling scheme the calculation of extracellular potentials can straightforwardly be extended to *populations* of neurons. The computation time grows linearly with the number of neurons, and the calculation of extracellular potentials from joint activity in populations with thousands of morphologically reconstructed neurons can be done on present-day desktop computers (Pettersen et al. 2008).

15.3.2.2 Estimation of Current-Source Density (CSD)

If we introduce the quantity

$$C(\boldsymbol{r},t) \equiv I_0(t)\delta^3(\boldsymbol{r}-\boldsymbol{r}_0), \tag{15.5}$$

where $\delta^3(r)$ is the three-dimensional Dirac δ-function, the forward-modeling formula in Eq. 15.4 can be reformulated as

$$\varphi(\boldsymbol{r},t) = \frac{1}{4\pi\sigma}\iiint_V \frac{C(\boldsymbol{r}',t)}{|\boldsymbol{r}-\boldsymbol{r}'|}d^3\boldsymbol{r}'. \tag{15.6}$$

Here the volume integral goes over all transmembrane currents. The quantity $C(\boldsymbol{r},t)$ corresponds to a *current source density (CSD)*, i.e., the volume density of current entering or leaving the extracellular medium at position $\boldsymbol{r}$ (Nicholson and Freeman 1975; Mitzdorf 1985; Nunez and Srinivasan 2006). A negative $C(\boldsymbol{r},t)$ corresponds to current leaving the extracellular medium and is thus conventionally called a *sink*. Likewise, current entering the extracellular medium is called a *source*.

The CSD distribution from activity in a single or numerous neurons could in principle be described as a sum over point-like CSD contributions as described by Eq. 15.5. However, in practice the CSD is generally considered to be a more coarse-grained measure describing the net transmembrane current entering or leaving a volume a few tens of micrometers across (Nicholson and Freeman 1975). As the

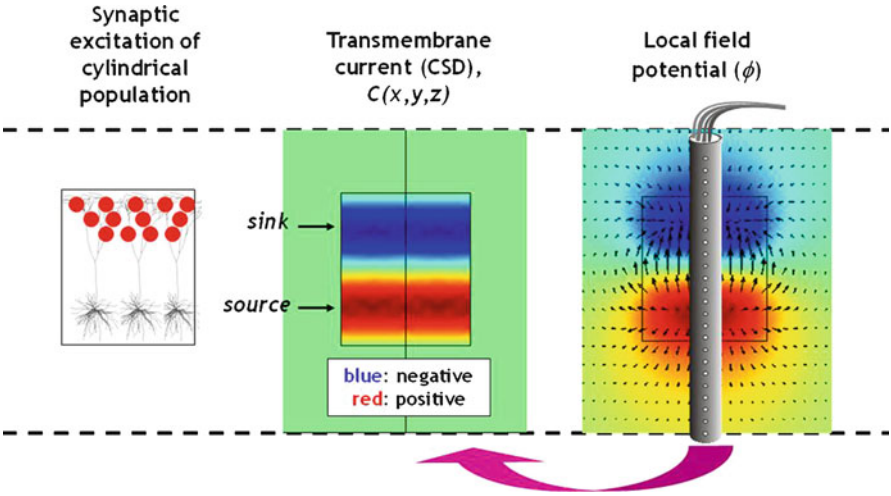

Fig. 15.10 Schematic illustration of principle behind CSD analysis. In the example a cylindrical population of pyramidal neurons receives synaptic excitation in their apical dendrites (*left panel*), resulting in a cylindrically symmetric (*columnar*) CSD distribution with an apical current *sink* accompanied by a basal current *source* due to return currents (*middle panel*). A linear (*laminar*) multielectrode (see Sect. 15.2.2) inserted into the population would measure a corresponding LFP (*right panel*), and the task of CSD analysis is to estimate the CSD distribution $C(\boldsymbol{r},t)$ based on the LFP recordings $\varphi(r_i,t)$, $(i = 1,\ldots,N_c)$ at the N_c electrode contacts

CSD is easier to relate to the underlying neuronal activity than the extracellular potential itself, CSD analysis has become a standard tool for analysis of the low-frequency part (LFP) of such potentials recorded with linear (laminar) multielectrodes (Nicholson and Freeman 1975; Pettersen et al. 2006). The principle behind such analysis is illustrated in Fig. 15.10.

While Eq. 15.6 gives the numerical recipe for calculating the extracellular potential given the CSD, a formula providing the opposite relationship can also be derived. For the case with a position- and direction-independent extracellular conductivity σ one finds (Nicholson and Freeman 1975; Nunez and Srinivasan 2006)

$$\sigma\nabla^2\varphi(\boldsymbol{r},t) = -C(\boldsymbol{r},t). \tag{15.7}$$

This equation, called Poisson's equation, is well known from standard electrostatics where it describes another problem, namely how potentials are generated by electrical charges (with the conductivity σ replaced by the dielectric constant ε (Jackson 1998).

CSD estimation has typically been based on LFP recordings with laminar (linear) multielectrode arrays (see Sect. 15.2.2) with a constant inter-contact distance h inserted perpendicularly to the cortical surface (Rappelsberger et al. 1981; Mitzdorf 1985; Di et al. 1990; Schroeder et al. 2001; Ulbert et al. 2001; Einevoll et al. 2007). Cortical tissue has a prominent laminar structure where changes in the lateral directions are

much smaller than in the vertical direction. It has thus been common to assume homogeneous (constant) CSD in the lateral (*xy*) plane, i.e., perpendicular to the laminar electrode oriented in the *z*-direction (unlike the example in Fig. 15.10 where the CSD is non-zero only inside a finite column). Variation of the extracellular potential in the *x*- and *y*-directions can then be neglected, so that Eq. 15.7 simplifies to its one-dimensional version:

$$\sigma \frac{d^2\phi(z,t)}{dz^2} = -C(z,t). \tag{15.8}$$

The *"standard"* estimator for the CSD at electrode position z_j has thus been (Nicholson and Freeman 1975)

$$C(z_j) = -\sigma \frac{\phi(z_j + h) - 2\phi(z_j) + \phi(z_j - h)}{h^2} \tag{15.9}$$

or variations thereof including additional spatial smoothing filters (Freeman and Nicholson 1975, Ulbert et al. 2001).

The standard estimation formula in Eq. 15.9 has several limitations. For one, the formula only predicts the CSD at the $N_c - 2$ interior contact positions. (This problems gets even more severe with the analogous analysis for two- or three-dimensional cartesian recording grids (Leski et al. 2007) where a higher fraction of the contacts is at the surface.) Secondly, the estimation scheme relies on equidistant electrode contacts and is thus vulnerable to malfunction of individual contacts. Further, the one-dimensional scheme breaks down when the CSD varies significantly in the lateral direction.

In Pettersen et al. (2006) we introduced the *inverse CSD (iCSD)* method to alleviate these problems. The core idea behind iCSD is to exploit the forward-modeling scheme in Eq. 15.6: with an assumed form of the CSD distribution parameterized by *N* unknown parameters, the forward solution can be calculated and inverted to give estimates of these *N* parameters based on *N* recorded potentials. This iCSD approach has several inherent advantages: (1) The method does not rely on a particular regular arrangement of the *N* electrode contacts recording the LFP signals, but can be straightforwardly be generalized to all sorts of multielectrode geometries (Pettersen et al. 2006; Leski et al. 2007). (2) A priori knowledge, such as estimates of the lateral size of columnar activity or discontinuities and direction dependence of the extracellular conductivity, can be built directly into the iCSD estimator (Pettersen et al. 2006; Einevoll et al. 2007; Pettersen et al. 2008). (3) Unlike the standard CSD method, the iCSD method can also predict CSD at the positions of the boundary electrode contacts.

More detailed information about the iCSD method can be found in Pettersen et al. (2006) and Leski et al. (2007). Moreover, a MATLAB toolbox, *CSDPlotter*, for iCSD estimation based on laminar multielectrodes has been developed and can be downloaded from *http://software.incf.org/*.

15.3.2.3 Extraction of Population-Specific Synaptic Connections and Firing Rates

Even if CSD is a more localized and intuitive measure of neuronal activity than LFP, its interpretation is nevertheless difficult. Transmembrane dendritic currents from multiple populations of neurons contribute to CSD. Ideally one would like to be able to interpret the LFP in terms of activity in individual neuronal populations as this would give more insight into the organization and functioning of the cortical circuits. In a series of papers Barth and collaborators pursued such an scheme by use of principal component analysis (PCA) of the CSD (Barth et al. 1989; Barth et al. 1990; Di et al. 1990; Barth and Di 1991), and in their study of stimulus-evoked data from the rat barrel cortex they identified putative cortical populations in supra- and infragranular layers of the barrel column (Di et al. 1990). PCA is one of several statistical methods where functions of two variables (here electrode contact positions and time) are expanded into sums over spatiotemporally separable functions, i.e., functions that can be written as a product of a spatial function and a temporal function. This can be done in an infinite number of ways, and additional constraints are needed to make the expansion unique. In PCA, for example, the functions (i.e., components) are constrained to be orthogonal both in space and time.

We recently introduced a new analysis method, *Laminar Population Analysis (LPA)*, where we instead of assuming somewhat arbitrary mathematical constraints used *physiological* constraints to specify the population expansion of laminar-electrode data (Einevoll et al. 2007). As a consequence the expansion is not only compatible with the physiology, each component also has a clear physiological interpretation. The basic underlying constraint inherent in LPA is that the observed LFP is evoked by the firing of action potentials in the modelled neuronal populations. An experimental measure of this population firing is obtained from the high-frequency component (>500–750 Hz) of the laminarly recorded extracellular potentials, i.e., the multi-unit activity (MUA) (Schroeder et al. 2001; Ulbert et al. 2001; Pettersen et al. 2008; Blomquist et al. 2009). Thus both the LFP and MUA signals are used in the analysis, unlike in CSD analysis where only the LFP signals are used. The outcomes of LPA are (1) identification of the relevant laminar cortical populations and their vertical spatial position and extent, (2) estimates of the firing-rates of these populations, and (3) estimates of the spatiotemporal LFP signature (and CSD signature) following action-potential firing in the individual populations (Einevoll et al. 2007).

The fundamental equations of LPA analysis are

$$\phi_{\mathrm{MUA}}(z_i,t) = \sum_{n=1}^{\mathrm{N_p}} M_n(z_i) r_n(t) \tag{15.10}$$

$$\phi_{\mathrm{LFP}}(z_i,t) = \sum_{n=1}^{\mathrm{N_p}} L_n(z_i)(h * r_n)(t) \tag{15.11}$$

In Eq. 15.10 the MUA signal $\varphi_{\mathrm{MUA}}(z_i,t)$, essentially the rectified high-frequency part of the extracellular signal sampled at the various electrode contacts positioned at z_i $(i=1,\ldots,N_c)$, is modelled as as a sum over spatiotemporally separable contributions from several neuronal populations. Here N_p is the number of populations, and $r_n(t)$ represents the firing rate of population n. Modeling studies indeed found this MUA signal to be well correlated with the true population firing rate for stimulus-evoked, trial-averaged data (Pettersen et al. 2008). $M_n(z_i)$ is the MUA spatial profile associated with action-potential firing in population n. This spatial profile will in general depend on the physiological properties of the neurons in the population as well the distribution of their spatial positions in the cortical lamina. The size of the extracellular signature of an action potential decays rapidly with distance from the neuronal soma, and the horizon of visibility is typically less than 100 μm (Somogyvari et al. 2005). The MUA is thus a very localized measure of neuronal firing, and the MUA spatial profile $M_n(z_i)$ appears to be mainly determined by the vertical spread of somas of the neurons belonging to the same population.

Next, in Eq. 15.11 the LFP data is assumed to be driven by the same population firing rates $r_n(t)$ seen in the MUA data: Firing of an action potential of a neuron in population n will lead to postsynaptic transmembrane currents (including both the ligand-gated synaptic currents and consequent return currents) which in turn contribute to the LFP. Consequently, it is assumed that the LFP data can be decomposed into contributions from each of the neuronal populations as implied by Eq. 15.11. Here $(h * r_n)(t)$ is the temporal convolution between $h(t)$ and $r_n(t)$, and $L_n(z_i)$ represents the spatial profile of the contribution to the LFP data following action-potential firing in population n. The temporal coupling kernel $h(t)$ accounts for the temporal delay and spread in the generation of the LFP following firing of neurons in population n. In Einevoll et al. (2007) exponentially decaying coupling kernels were used. A graphical illustration of the principle behind LPA can be found in the left panel of Fig. 15.11.

In Einevoll et al. (2007) the method was applied to stimulus-averaged laminar-electrode data from barrel cortex of anesthetized rat following single whisker deflections. The numerical task was to identify the spatial profiles ($M_n(z_i)$, $L_n(z_i)$), population firing rates $r_n(t)$, and parameters of the temporal coupling kernel $h(t)$ giving the minimum deviations between the model MUA and LFP signals and the experimental data $\varphi_{\mathrm{MUA}}(z_i,t)$ and $\varphi_{\mathrm{MUA}}(z_i,t)$, respectively. The data were found to be well accounted for by a model with four cortical populations: one supragranular, one granular, and two infragranular populations. Further, the spatial LFP population signatures $L_n(z_i)$ were further used to estimate the synaptic connection pattern between the various populations using a new *LFP template-fitting technique* (Einevoll et al. 2007). Here the estimated $L_n(z_i)$ for each laminar population n was decomposed into sums over LFP population templates found by forward modeling with morphologically reconstructed neurons, so that the values of the fitted weights provided specific predictions about the synaptic connections. Results from this analysis are shown in the right panel of Fig. 15.11.

In a recent study we took LPA a step further and used the estimated population firing rates $r_n(t)$ to extract population firing-rate *models* for both thalamocortical and intracortical signal transfer in the rat barrel system (Blomquist et al. 2009). Here the

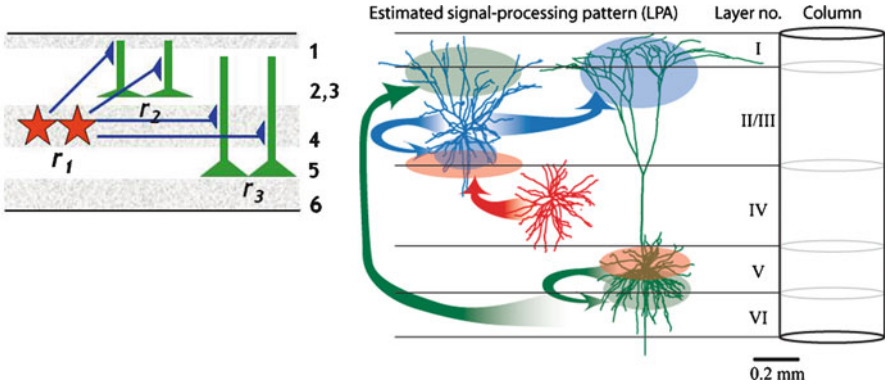

Fig. 15.11 Laminar Population Analysis. *Left panel*: Illustration of principle behind *Laminar Population Analysis (LPA)*. Three populations are considered in the sketch: a granular population of stellate cells with firing rate r_1 , a supergranular population of pyramidal neurons with firing rate r_2, and an infragranular population of pyramidal neurons with firing rate r_3 . In LPA the population firing rates are assumed to be related to the MUA signal via Eq. 15.10 and also give rise to the LFP signal via their postsynaptic effects, as captured by Eq. 15.11. In the panel this is illustrated for the LFP contribution from the stellate population, i.e., $L_1(z_i)(h * r_1)(t)$. The spatial form of $L_1(z_i)$ will be determined by the total efferent action of the stellate-cell population onto its postsynaptic targets (schematically illustrated with solid lines and triangular synapses). Right panel: Illustration of some results from LPA analysis from Einevoll et al. (2007) on estimation of functional synaptic connection patterns between populations in a barrel column in rat somatosensory cortex. The arrows indicate pre- and postsynaptic populations while the same-colored ellipsoids indicate the region of the dendrites receiving synaptic inputs (assuming that the synaptic connections are predominantly excitatory). For example, the stellate population (*red*) was found to have a strong projection onto the basal dendrites of the supergranular population, and both the supergranular and infragranular populations were found to have a projections onto their own basal dendrites. For more information and results, see Einevoll et al. (2007)

laminar-electrode recordings were supplemented with simultaneous thalamic single-electrode recordings. These experimentally extracted cortical and thalamic firing rates were in turn used to identify population firing-rate models formulated either as integral equations or as more common differential equations. Optimal model structures and model parameters were identified by minimizing the deviation between model firing rates and the experimentally extracted population firing rates. For the thalamocortical transfer the experimental data was found to favor a model with fast feedforward excitation from thalamus to the layer IV laminar population combined with a slower inhibitory process due to feedforward and/or recurrent connections. The intracortical population firing rates were found to exhibit strong temporal correlations and simple feedforward firing-rate models were found to be sufficient to account for the data. Thus while the thalamocortical circuit was found to be optimally stimulated by rapid changes in the thalamic firing rate, the intracortical circuits were found to be low-pass and respond strongest to slowly varying inputs from the cortical layer IV population.

LPA, combined with the abovementioned LFP template-fitting technique and/or the population rate-model extraction method, promise to be a useful tool for extraction

of information on neuronal population activity from the new generation of silicon-based multielectrodes (Buzsaki 2004). However, new analysis tools still needs to be developed, and the forward-modeling technique outlined above will be essential not only in the development of the tools, but also in generating model data against which the new tools can be tested.

In the examples above, neuronal populations are defined according to the cortical depth. In the future we hope to extend the approach to cell-type specific populations with the ultimate goal of reconstructing vasoactive transmitter release from each of the relevant neuonal populations across stimulus conditions (see Sect. 15.4.1).

15.3.3 Modeling of Microscopic Vascular Dynamics and Oxygen Consumption

15.3.3.1 Vascular Anatomical Network (VAN) Modeling

Use of reduced or "lumped" models of the vascular and oxygen transport responses is increasingly common in fMRI analyses (reviewed in (Obata et al. 2004)). Although a reasonable fit to measurement data can be obtained with such models (Huppert et al. 2007), the resulting lumped or effective model parameters, e.g., vessel compliance, cannot be directly compared against microscopic properties nor can predictions be made about the spatial pattern of the hemodynamic response. We have developed a dynamic mechanistic *Vascular Anatomical Network (VAN)* model, which incorporates biophysically realistic parameters at the microscopic scale. This approach can be used with either stylistic vascular geometry (Boas et al. 2008), or a realistic geometry derived from 2-photon measurements of an *in vivo* vascular network (Devor et al. 2008b; Fang et al. 2008).

The VAN model represents the vascular tree as a set of branching, cylindrical segments, with a specified topology/geometry, incorporates biophysically realistic parameters at the microscopic scale, and allows a consistent calculation of flow characteristics (resistance, pressure changes, etc.) and O_2 dynamics (hemoglobin saturation in different compartments and average tissue pO_2) (Fang et al. 2008). The activity of specific neurons cause dynamic changes in the diameter of the arterioles/capillaries (that serves as an input to VAN), resulting in CBF changes due to the altered vascular resistance due to these vessel diameter changes. The incorporation of oxygen dynamics enables estimation of intra- and extravascular microscopic oxygenation changes.

The VAN model uses a network of resistors and non-linear capacitors to model the relationship between blood flow, volume, resistance, and pressure (Fig. 15.12). In this framework, the active vessel diameter changes in the arteriolar compartments lead to a change in resistance and, thus a change in CBF proportional to the pressure drop across the compartment. As the arteriolar resistance decreases, pressure shifts downstream into the compliant capillaries and venules resulting in their compliant dilation and secondary blood volume and flow increases. Oxygen dynamics

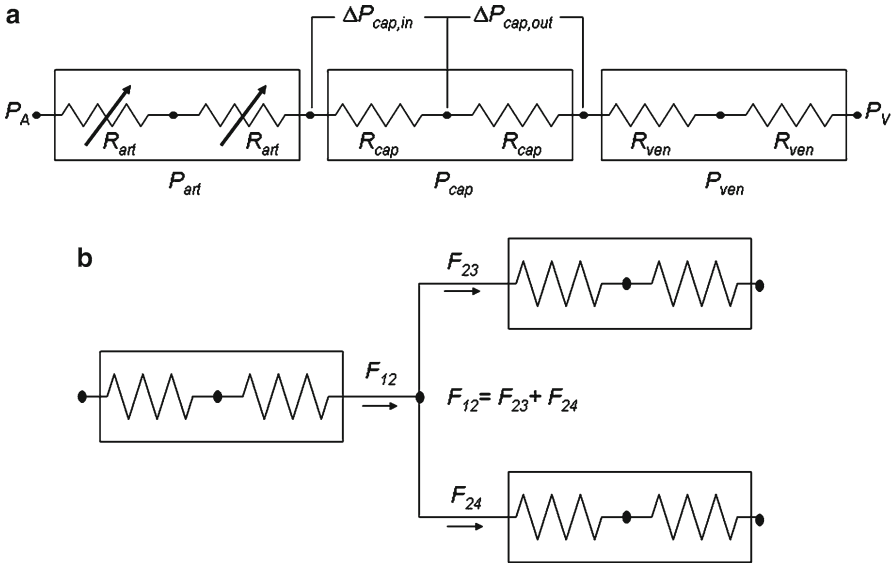

Fig. 15.12 VAN flow-volume dynamics. For more details see (Boas et al. 2008)

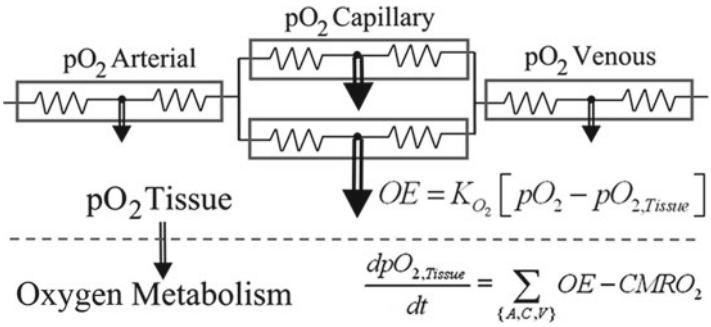

Fig. 15.13 VAN oxygen dynamics. For more details see (Boas et al. 2008)

is incorporated into the network as illustrated in Fig. 15.13. Vessel dilation and constriction, and $CMRO_2$, arising from the firing rates of excitatory and inhibitory neurons, serve as inputs to the model, resulting in predictions of CBF, cerebral blood volume (CBV), and pO_2 in blood and tissue, as functions of time and space.

One question that this VAN model has addressed is the origin of a "surround" hemodynamic negativity that has been observed in response to brain activation (Cox et al. 1993; Woolsey et al. 1996; Takashima et al. 2001; Devor et al. 2005; Devor et al. 2007; Devor et al. 2008b). The question was whether this surround negativity arises from passive redistribution of blood flow to support center increases, or whether neuronal processes are involved that are actively vasoconstricting the

vessels. As detailed in (Boas et al. 2008), the VAN model showed that localized arterial dilation induced a chain of passive events in both a center region of interest and in the surrounding vessels such that, concurrent with increases in flow and oxyhemoglobin in the center, there was a passive decrease in flow and oxyhemoglobin in the surround. The VAN model predicted that the observed surround decreases are at least partially due to passive vessel properties that create a local redistribution of blood. However, a comparison with experimental data suggested that the incorporated vessel properties are not sufficient to account for the magnitudes of decreases in the surround. Several factors may contribute to this discrepancy. A likely explanation is active vasoconstriction of arteries and arterioles through activation of the smooth muscles that line them (Cox et al. 1993; Hamel 2004; Lauritzen 2005; Hamel 2006; Devor et al. 2007; Devor et al. 2008b), or active changes in the diameter of capillaries (Peppiatt et al. 2006). Active vasoconstriction could be induced by the release of neurotransmitters or neuropeptides, and may be associated with center-surround electrophysiological patterns of activity consisting of center excitation and surround inhibition (Faraci and Breese 1993; Faraci and Heistad 1998; Takashima et al. 2001; Derdikman et al. 2003; Cauli et al. 2004; Devor et al. 2007; Devor et al. 2008b).

Further evolution of VAN model and validation against experimental data will lead to further insights on the regulation of blood flow by specific vascular branches of the arterioles and capillaries, the role of retrograde vasodilation, the oxygen delivery to the tissue from arterioles versus capillaries versus venules, and flow and dilation induced changes in hematocrit (Hillman et al. 2007) to name a few. While VAN modeling is too complex and ill-constrained to allow routine fitting to experimental data from macroscopic fMRI and optical measures, the interpretation of the "lumped" compartment models is derived from this underlying anatomical detail. Thus, VAN model will illuminate issues with the assumptions of the "lumped" models used to analyze human fMRI and optical imaging data (see Sect. 15.3.3.2 below).

15.3.3.2 Calculation of the Metabolic Rate of O_2

Why Study $CMRO_2$?

In contrast to the diversity of measurement methods that can be applied to study neuronal and vascular activity with high resolution and precision in animal models, human imaging studies are limited by the existing non-invasive tools, mainly fMRI, PET and EEG/MEG. Among them, fMRI has been widely used for cognitive studies and is beginning to make inroads into clinical applications (D'Esposito et al. 2003; Guadagno et al. 2003; Hodics and Cohen 2005; Teasell et al. 2005). However, as was mentioned in the Introduction, the BOLD fMRI signal depends on the balance of the changes in CBF and $CMRO_2$, and therefore is sensitive to the baseline CBF conditions. In other words, the BOLD signal in response to the same increase in neuronal activity is expected to change given different baseline CBF. Therefore, a

major focus in the field has been in development methods for extraction of $CMRO_2$ that supposedly provides a better surrogate measure of neuronal activity and is insensitive of the baseline vascular conditions.

The Challenging Task of Measuring $CMRO_2$

In human imaging, the primary physiological variables related to cerebral blood flow and energy metabolism are CBF, cerebral metabolic rate of glucose (CMRGlc) and $CMRO_2$, and a general goal is to be able to quantify these variables in a local brain region. The accepted standard for CBF measurements is a microsphere experiment, in which labeled microspheres are injected arterially (Yang and Krasney 1995). Because the microspheres are too large to pass through the capillaries, they stick in the tissue, and the local concentration of microspheres then directly reflects the local CBF. With an appropriate measurement of the injected arterial bolus, the local CBF can be quantified in absolute units of ml blood/ml tissue-min. For human studies with MRI, ASL methods approach the ideal microsphere experiment because the delivery of magnetically labeled blood is measured only 1–1.5 s after creation of the labeled blood, so there is little time for the labeled blood to pass through the capillary bed and clear from tissue (Buxton 2005).

For CMRGlc methods there is also an accepted standard based on injection of radioactively labeled deoxyglucose (DG), a chemically modified form of glucose (Sokoloff et al. 1977; Phelps et al. 1981) (see also Sect. 15.4.4). Deoxyglucose is similar enough to glucose that the initial stages of uptake from blood and metabolism in the cytosol are similar to glucose. However, when the DG reaches a certain stage in the metabolic pathway the chemical difference between glucose and DG is critical, and the DG is not further metabolized and remains in the tissue. By waiting sufficiently long for unmetabolized DG to diffuse back into blood and clear from the tissue, the remaining radioactive label in tissue directly reflects the rate of metabolism of glucose. As with the CBF measurement with microspheres, an appropriate measurement of the arterial concentration over time makes it possible to measure CMRGlu in absolute units of micromoles/100 ml tissue-min. Technically, this method measures the metabolic rate of DG, and a correction is needed to account for rate constant differences between glucose and DG. Given the need for this correction, at first glance it might seem that a more direct way to measure CMRGlu would be to inject radioactively labeled glucose itself. The essential problem, however, is that measurement of the concentration of the radioactive label does not distinguish between the label in glucose and the label in products of metabolism of glucose (e.g., with carbon-14 the net concentration of label reflects labeled CO_2 as well as glucose). In short, the DG technique is effective because it acts in a similar fashion to microspheres in a CBF measurement: the delivery of the agent reflects the appropriate physiological rate (CBF or CMRGlu), and the agent then sticks in the tissue so that the concentration can be readily measured.

Although O_2 metabolism is a key element of brain function, $CMRO_2$ is much more difficult to measure than CBF or CMRGlu. Currently there is no accepted

"gold standard" for such measurements, and no established methods for measuring dynamic $CMRO_2$ changes. In essence, this is because there is no experiment equivalent to the microsphere or DG experiment in which a single measurement reflects $CMRO_2$ alone. For this reason, $CMRO_2$ must be estimated from multiple measurements analyzed within the context of an appropriate mathematical model of the physiology and the measured quantities. This adds a layer of complexity to $CMRO_2$ estimates, and raises associated concerns about the accuracy of the $CMRO_2$ estimates related to the assumptions and limitations of the experimental methods and models used. The following sections review current approaches for combining multi-modal measurements to estimate changes in $CMRO_2$.

The Importance of the O_2 Extraction Fraction

A primary physiological relationship that often underlies methods for estimating $CMRO_2$ is the connection between CBF, $CMRO_2$ and the O_2 extraction fraction (E):

$$CMRO_2 = E \cdot CBF \cdot [O_2]_a \tag{15.12}$$

where $[O_2]_a$ is the arterial concentration of O_2. The extraction fraction E is defined as the fraction of O_2 delivered to the capillary bed that is extracted from the blood and metabolized in tissue, and so is closely related to the venous O_2 concentration. Note that this relationship follows simply from mass balance and the definition of the terms. The product of CBF and $[O_2]_a$ is the rate of delivery of O_2 to the capillary bed, and multiplying by E gives the net rate of metabolism of O_2. Both CBF and $CMRO_2$ are referred to a unit volume (or mass) of tissue. For example, a consistent set of values and associated units for these variables, typical for the human brain, would be: $CMRO_2$ (160 μmol/100 ml tissue-min), CBF (50 ml blood/100 ml tissue-min), E (0.4, dimensionless, ranging from 0 to 1), and $[O_2]_a$ (8 mM blood).

Often the fractional change in a variable is the desired quantity, and absolute values may not be essential. For example, in considering a dynamic change from a baseline state due to neuronal activation, it is often useful to consider the CBF normalized to its baseline value (f) and the $CMRO_2$ normalized to its baseline value (m), related by:

$$m = f \frac{E}{E_0} \tag{15.13}$$

where the subscript "0" denotes values in the baseline state. Note, though, that this relationship is essentially a steady-state relationship, and for rapid changes faster than the capillary transit time, the dynamic definition of E would need to be reconsidered. Nevertheless, this basic relationship is usually assumed to be accurate in most applications.

Several approaches for estimating $CMRO_2$ involve combining measurements sensitive to E (e.g., OISI and BOLD imaging) with a measurement of the normalized CBF change. The ratio of O_2 extraction fractions is directly related to the venous

deoxyhemoglobin concentrations. If Hb_v and HbT_v are the venous deoxyhemoglobin and venous total hemoglobin concentrations, respectively, and Hb_{v0} and HbT_{v0} are the corresponding values in the baseline state, then:

$$\frac{E}{E_0} = \frac{Hb_v / Hb_{v0}}{HbT_v / HBT_{v0}} \tag{15.14}$$

The central goal in estimating $CMRO_2$ changes is then to estimate E/E_0 from the measured data, combine this with a measurement of the normalized CBF change (f), and calculate the relative $CMRO_2$ change from Eq. 15.13.

Estimating $CMRO_2$ with PET

The leading method for measuring $CMRO_2$ in human studies uses positron emission tomography (PET) and molecules labeled with ^{15}O, a positron emitting radionuclide (Mintun et al. 1984). The primary measurement is the uptake of ^{15}O after injection of ^{15}O labeled O_2, providing a measurement that depends on E and CBF. However, such a measurement cannot distinguish between extracted O_2, labeled blood pool O_2 and labeled water produced as a product of O_2 metabolism produced throughout the body and circulated to the brain. The appropriate arterial input curves must distinguish between ^{15}O labeled O_2 and ^{15}O labeled water, requiring frequent arterial blood sampling and separate analysis of whole blood and plasma ^{15}O concentrations. In addition, the study must be repeated with two additional labeled molecules: ^{15}O labeled water to measure CBF, and ^{15}O labeled carbon monoxide to measure blood pool contributions. Taken together, these three measurements provide enough information to estimate $CMRO_2$, with the modeling assumption that all of the extracted O_2 is metabolized. Because of the requirement for three separate studies, this approach measures steady-state $CMRO_2$, and has limited capability for dynamic studies. More recently, variations of this method have been developed to provide a more streamlined approach (Kudomi et al. 2007; Kudomi et al. 2009) and to adapt this method to the challenges of animal studies (Yee et al. 2006). Although technically challenging to apply, the PET method is currently the closest to an accepted standard of $CMRO_2$ measurement.

Estimating $CMRO_2$ Changes with Optical Intrinsic Signal Imaging (OISI)

With the OISI techniques described earlier (Sect. 15.2.1.1), the changes in oxyhemoglobin (ΔHbO), deoxyhemoglobin (ΔHb) and total hemoglobin (ΔHbT) can be measured dynamically, potentially providing the opportunity for measuring dynamic changes in $CMRO_2$. The general approach is to use the measured data to estimate E/E_0, and combine this with a separate measurement of the CBF change to estimate the $CMRO_2$ change from Eq. 15.13 (Mayhew et al. 2000; Jones et al. 2001; Dunn et al. 2005; Royl et al. 2008). There are two challenges related to this approach

that require modeling assumptions. The first is that E/E_0 depends on hemoglobin changes normalized to their baseline values, but the measurements are of differences (e.g., ΔHb), and the baseline values Hb_0 and HbT_0 are not known. Typically, assumed values are used for the baseline concentrations (but see (Dunn et al. 2005)). The second challenge is that the relevant hemoglobin concentrations are the venous values (Eq. 15.14), but the measured values sample the full vasculature. Several studies have used the simple assumption that the ratios in Eq. 15.14 for the venous blood are the same as those measured for the total vasculature. Jones and colleagues (Jones et al. 2001) explicitly described the assumptions involved by introducing two new parameters, γ_r and γ_t, defined as:

$$\gamma_r = \frac{\Delta Hb_v / Hb_{v0}}{\Delta Hb / Hb_0} \quad \gamma_t = \frac{\Delta HbT_v / HbT_{v0}}{\Delta HbT / HbT_0} \tag{15.15}$$

The simplest assumption, that $\gamma_r = 1$ and $\gamma_t = 1$ is often used, although more detailed vascular modeling, such as the VAN model described above (Sect. 15.3.3.1), should make possible more realistic estimates of these parameters. In particular, a number of human imaging studies have suggested that the changes in blood volume with activation occur predominantly on the arterial side (Lee et al. 2001; Ito et al. 2005; Kim et al. 2007). Recent 2-photon studies in animals are consistent with implications of these macroscopic fMRI measurements, reporting no change in venous diameters (Hillman et al. 2007; Tian et al. 2008). Therefore, γ_t could be substantially smaller than one.

Estimating $CMRO_2$ Changes with fMRI

The BOLD response also is sensitive to changes in blood oxygenation associated with brain activation. Deoxyhemoglobin is paramagnetic, and distorts the magnetic field around blood vessels, and these field distortions slightly reduce the net MR signal from what it would be if there was no deoxyhemoglobin present. With activation CBF increases more than $CMRO_2$, and the reduction of local deoxyhemoglobin leads to an increase of the MR signal. This BOLD signal change is often modeled as (Davis et al. 1998):

$$\frac{\Delta S}{S_0} = M\left[1 - \frac{Hb_v}{Hb_{v0}}\left(\frac{E}{E_0}\right)^{\beta}\right] \tag{15.16}$$

where S_0 is the baseline signal, M is a scaling parameter that defines the maximum possible BOLD signal change, and β is a parameter usually taken to be equal to 1.5, based on Monte Carlo simulations of the signal decay process due to the deoxyhemoglobin (Boxerman et al. 1995). The venous hemoglobin ratio is taken to be the venous volume ratio, and this is modeled as a power law relationship with the CBF change. Specifically, the assumption used is that the hemoglobin ratio in Eq. 15.16

is equal to f^{α}, with $\alpha = 0.38$ based on early measurements of the relationship between CBF and total blood volume (Grubb et al. 1974). In terms of the normalized changes in CBF and $CMRO_2$, the BOLD signal change is then modeled as:

$$\frac{\Delta S}{S_0} = M\left[1 - f^{\alpha}\left(\frac{m}{f}\right)^{\beta}\right] \tag{15.17}$$

The scaling parameter M depends on baseline state conditions (Hb_{v0} and E_0), as well as the image acquisition method and the magnetic field strength. For this reason, M should be measured rather than assumed. To do this, Davis and colleagues (Davis et al. 1998) introduced the calibrated BOLD method, in which both the BOLD and CBF responses are measured for the neuronal activation experiment and also for a hypercapnia experiment in which the subject breathes a gas with a CO_2 concentration of about 5%. The idea of this calibration experiment is that mild hypercapnia is thought to increase CBF without changing $CMRO_2$. Using Eq. 15.17 with the assumption that $m = 1$, measurement of local BOLD and CBF changes to hypercapnia allow calculation of M, and using this value of M with the measured BOLD and CBF responses to neuronal activation allows calculation of m, the relative $CMRO_2$ change, for the activation experiment.

A key assumption in the calibrated BOLD method is that mild hypercapnia does not alter $CMRO_2$. There is experimental support for the latter assumption (Sicard and Duong 2005), but recently has been questioned (Zappe et al. 2008). High levels of arterial CO_2 depress brain activity, and so the central question is whether the lower levels used in the calibrated BOLD experiment are having a significant effect on $CMRO_2$. One complication in trying to address this central question with animal studies is that the key physiological parameter is arterial CO_2 content, rather than inspired CO_2 content (typically 5% in calibrated BOLD studies). Awake humans often increase ventilation rate during hypercapnia, reducing the effect on arterial CO_2, so for the same inspired CO_2 concentration the resulting change in arterial CO_2 can be larger in an animal experiment in which ventilation is controlled. The issue of $CMRO_2$ changes with hypercapnia needs further study as a potential systematic error in the calibrated BOLD method.

The estimates of $CMRO_2$ change with the calibrated BOLD experiment also depend on the assumed values of the parameters α and β. As in the OISI experiment, there is an assumption about how the venous blood volume change is related to the overall blood volume change. In the context of calibrated BOLD this is described by the parameter α rather than γ_t, but the same underlying assumption is involved. Given the data mentioned above suggesting that most of the blood volume change with activation is on the arterial side, a lower value of α may be more accurate. The parameter β was originally introduced as an approximate description of numerical simulations for deoxyhemoglobin in vessels of different sizes (Boxerman et al. 1995). The same amount of deoxyhemoglobin in a larger vein is more effective at reducing the net MR signal than it is in a smaller capillary, and this leads to the nonlinearity (Ogawa et al. 1993). However, the use of $\beta = 1.5$, rather than 1.0,

also fortuitously allows the Davis model to describe additional sources of signal variation – that were not included in the original derivation – due to intravascular signal changes and blood/tissue exchange signal changes (Buxton et al. 2004; Leontiev and Buxton 2007; Leontiev et al. 2007). In addition, the use of the same equation for estimating *M* and then for estimating *m* tends to reduce errors related to the assumed values of α and β. For these reasons, the Davis model is likely to be more robust than one would expect based on the original assumptions.

Estimating $CMRO_2$ Changes with Tissue pO_2 Measurements

A somewhat different approach to estimating $CMRO_2$ changes uses measurements of the tissue concentration of O_2 in combination with a measurement of the CBF change (Caesar et al. 2008). Tissue O_2 concentration can be measured dynamically with an appropriate electrode, and the values are usually calibrated as an equivalent partial pressure P_{O2} expressed in units of mm Hg or kilopascals (1 kPa = 7.5 mmHg). A typical value for brain tissue is 25 mmHg, corresponding to a concentration of about 0.03 mM.

The central modeling assumption is that $CMRO_2$ is associated with a passive diffusion of O_2 down a concentration gradient from capillary plasma to the mitochondria:

$$CMRO_2 = k\left[P_{O_2}(cap) - P_{O_2}(tissue)\right] \tag{15.18}$$

where *k* includes the solubility and diffusion coefficient of O_2 as well as factors related to capillary geometry and capillary density. The usual assumption is that the capillary geometry remains fixed, so that the increased gradient needed to support an increased O_2 flux (increased $CMRO_2$) must come from increasing the difference between capillary and tissue P_{O2} values. This is equivalent to assuming constant *k* as CBF and $CMRO_2$ change. The capillary P_{O2}, in turn, depends on *E* and a model for the O_2-hemoglobon saturation curve. Taken together, Eqs. 15.12 and 15.18 provide two equations relating the four variables CBF, $CMRO_2$, *E* and tissue P_{O2}. Measurement of the change in two of these variables, such as tissue P_{O2} and CBF, then allows calculation of the changes in the other two, $CMRO_2$ and *E*.

The basic principles outlined above are at the heart of estimating $CMRO_2$ from tissue P_{O2} data, but the details of how this is done can vary considerably. With a distributed model, such as the VAN model described above, the calculations can be done numerically along all of the vessels rather than explicitly calculating average capillary values, and this approach could in principle take into account changes in capillary density as well. Usually, though, the parameter *k* is assumed to remain constant during dynamic changes in CBF and $CMRO_2$. This is equivalent to assuming that there is no capillary recruitment.

In applying this approach, a central challenge is to properly model the O_2-hemoglobin saturation curve. Most of the O_2 in blood is bound to hemoglobin, but

it is the small plasma concentration that drives the diffusion gradient for O_2 flux into tissue. While it is reasonable to assume that O_2 bound to hemoglobin and O_2 dissolved in plasma are in fast equilibrium, this equilibrium curve changes as O_2 is removed from blood and CO_2 is added. The sigmoidal shape of the O_2-hemoglobin saturation curve is often characterized by a parameter P_{50}, the plasma P_{O2} for 50% saturation of hemoglobin. The interesting complexity of O_2 transport is that P_{50} shifts to higher values down the length of the capillary, which has the effect of raising capillary P_{O2} and facilitating unloading of O_2 from hemoglobin. More detailed simulations of O_2 transport are needed to test the accuracy of the assumptions typically used in estimating $CMRO_2$ from tissue pO_2 measurements.

15.3.4 Alternative MRI Methods for Estimating $CMRO_2$

Although the calibrated BOLD approach is currently the most widely used method for estimating $CMRO_2$ changes with MRI data, newer methods under development may provide useful experimental tools for assessing $CMRO_2$. One of the earliest approaches was to use inhalation of O_2 labeled with ^{17}O (Arai et al. 1990; Arai et al. 1991; Fiat and Kang 1992, 1993). Two different experimental approaches have been proposed for using ^{17}O. The earliest exploits a particular magnetic property of ^{17}O: when incorporated into a water molecule, it acts as a relaxation agent, altering the relaxation times of hydrogen nuclei. In this way the presence of ^{17}O labeled water can be detected with standard proton MRI as a change in relaxation rate. However, when the ^{17}O is incorporated in an O_2 molecule it does not have this relaxation property. This creates an interesting scenario in which ^{17}O inhaled as O_2 is not visible with standard proton MRI until the ^{17}O has been incorporated into water by O_2 metabolism in the mitochondria. The rate of appearance of labeled water is then proportional to local $CMRO_2$. To quantify this, however, requires additional measurement of the arterial input function (concentration of the label in arterial blood), and accounting for recirculation of the labeled water. Despite early interest in this approach, it has not been widely used to date due to the complexity involved in addressing these quantitation issues (similar to issues in the PET studies described earlier), combined with the high cost of ^{17}O.

A more recent approach for using ^{17}O exploits the fact that ^{17}O exhibits nuclear magnetic resonance, and so can be directly detected with MR spectroscopy methods (Zhang et al. 2004; Zhu et al. 2005). In this way, the ^{17}O is used as a detectable oxygen label analogous to the use of ^{15}O in PET studies. The same issues of determining the arterial input function remain, but MRI provides ways to do this. Although still hampered by the high cost of ^{17}O, this approach has the potential to provide useful estimates of $CMRO_2$.

Finally, another MRI approach is to measure the local venous O_2 saturation of hemoglobin. The idea is to exploit the fact that the T_2 relaxation time of blood depends on the hemoglobin saturation through the same mechanisms related to the magnetic properties of deoxyhemoglobin that underlie the BOLD effect.

The experimental challenge is to isolate the signal of venous blood and measure the T_2. A recent method called TRUST combines ideas from arterial spin labeling and T_2 measurement to estimate the T_2 in the sagittal sinus, and this is converted to an estimate of hemoglobin saturation with a calibration curve (Lu and Ge 2008; Lu et al. 2008; Xu et al. 2009). The venous saturation then directly gives an estimate of *E*, and combining this with a measurement of CBF using ASL techniques makes possible an estimate of $CMRO_2$. In this initial method looking at the sagittal sinus it is a global estimate of $CMRO_2$, but techniques for extending this approach to local measurements of venous T_2 are under development. A potential challenge for modeling this experiment is that the calibration curve relating blood T_2 with hemoglobin saturation could differ between subjects, particularly due to hematocrit variations, and the potential effect on quantitation accuracy still needs to be investigated.

15.4 What Have We Learned about Neurovascular Coupling from Experimental Measurements of Neuronal, Vascular and Metabolic Activity?

A large number of recent studies have used a wide variety of measurement techniques to address the relationship between neuronal, metabolic and hemodynamic signals on multiple scales. The tools range from non-invasive methods such as fMRI, PET, and EEG/MEG to microscopic imaging of single cells and single vessels. These efforts produced consistent evidence across studies and experimental paradigms and helped settling some of the principles of neurovascular and neurometabolic coupling (Table 15.1). Some other, unexplained or controversial, findings challenge current "working hypotheses" and drive the ongoing investigations. While reviewing this literature, it is constructive to keep in mind the limitations of different measurement methods and other potentially crucial differences in the experimental paradigms between the studies that might have produced seemingly contradicting data. Testing of working hypotheses requires not only collection of high quality empirical measurements but also use of computational analyses to bridge the findings across spatial scales and integrate the components in a multiparameter space of neurovascular physiology.

15.4.1 Cell-Type Specific Regulation of Blood Flow

Of particular note, our recent *in vivo* data, along with *in vitro* data from other labs, increasingly suggest that differential vascular control originates from activation of specific neuronal sub-populations through release of specific vasoactive agents (Table 15.1, findings 1 and 2). *In vitro* (brain slice) studies in cerebral and cerebellar cortices have demonstrated that spiking of specific types of neurons can cause

Table 15.1 Main recent findings in understanding of neurovascular coupling with respect to further questions

Main findings	Questions raised	References
1. Different neuronal cell types cause vasodilation or vasoconstriction of cerebral arterioles *in vitro*.	**Q1.** What are the neuronal cell types that cause vasodilation or vasoconstriction *in vivo*? How is it reflected in the hemodynamic response (that is also sensitive to oxygen consumption)?	(Cauli et al. 2004; Hamel 2004, 2006; Rancillac et al. 2006), see also (Kocharyan et al. 2008)
2. Predominant neuronal inhibition is related to vasoconstriction and negative BOLD fMRI response (at least in sensory cortices).	**Q2.** Are all inhibitory neuronal types vasoactive? Do all of them cause vasoconstriction *in vivo*?	(Shmuel et al. 2006; Alonso et al. 2007; Bressler et al. 2007; Devor et al. 2007; Boas et al. 2008; Devor et al. 2008b)
3. Hemodynamic response is non-linearly coupled to multiunit spiking activity (MUA) and local field potential (LFP); the exact relationship depends on the stimulus.	**Q3.** How can we model the relationship between MUA/LFP to neuronal activity in specific cell types? If we knew this relationship and also the vasoactive effect of each neuronal type (finding 1), could we predict macroscopic vascular response from macroscopic measures of neuronal activity?	(Devor et al. 2003; Jones et al. 2004; Nemoto et al. 2004; Sheth et al. 2004; Devor et al. 2005)
4. Astrocytes release vasodilators *in vivo* and *in vitro*.	**Q4.** Is all vasodilaton mediated by astrocytes?	(Zonta et al. 2003; Mulligan and MacVicar 2004; Takano et al. 2006; Gordon et al. 2008)
5. Astrocytes release vasoconstrictors *in vitro*.	**Q5.** Can astrocytes mediate vasoconstriction *in vivo*? Do they respond to activity of cortical inhibitory interneurons?	(Metea and Newman 2006; Blanco et al. 2008)
6. a) Increase in glucose consumption can happen in presence of vasoconstriction and a decrease in blood flow in areas with predominant neuronal inhibition. b) CBF response is not affected by artificially increasing baseline oxygenation.	**Q6.** Does this finding imply that there is no causal relationship between accumulation of energy metabolites and increases in blood flow? Alternatively, both energy metabolites and neurotransmitters can affect flow but neurotransmitters have a dominant effect.	(Devor et al. 2008b; Lindauer et al. 2009)
7. Arteries/arterioles and capillaries can both dilate and constrict in response to stimulus.	**Q7.** How can we model macroscopic vascular response as a function of microscopic dilation and constriction?	(Devor et al. 2007; Boas et al. 2008; Devor et al. 2008b; Stefanovic et al. 2008)
8. Veins do not change their diameter in response to stimulus (either short or long) but respond by change in blood flow and hematocrit.	**Q8.** Prominent models of fMRI response assume venous dilation (e.g. "Balloon" model (Buxton et al. 1998)). These models need to be revised to reflect new experimental data.	(Vanzetta et al. 2005; Hillman et al. 2007)
9. Vasodlilation propagates along diving arterioles towards the cortical surface *in vivo*.	**Q9.** What is the location of the initial dilation? Is there dependence on the branching order? Does dilation in layer IV precede that in other cortical layers?	(Tian et al. 2008)
10. Exchange of oxygen happens not only from capillaries but also from diving arterioles and their branches.	**Q10.** What is the temporal profile of tissue oxygenation at different distances from the feeding arterioles in response to stimulus? How can we combine these oxygenation profiles with microscopic dilation and constriction (Q7) to model microscopic hemodynamic response?	(Kasischke et al. 2011; Takano et al. 2007; Fang et al. 2008)

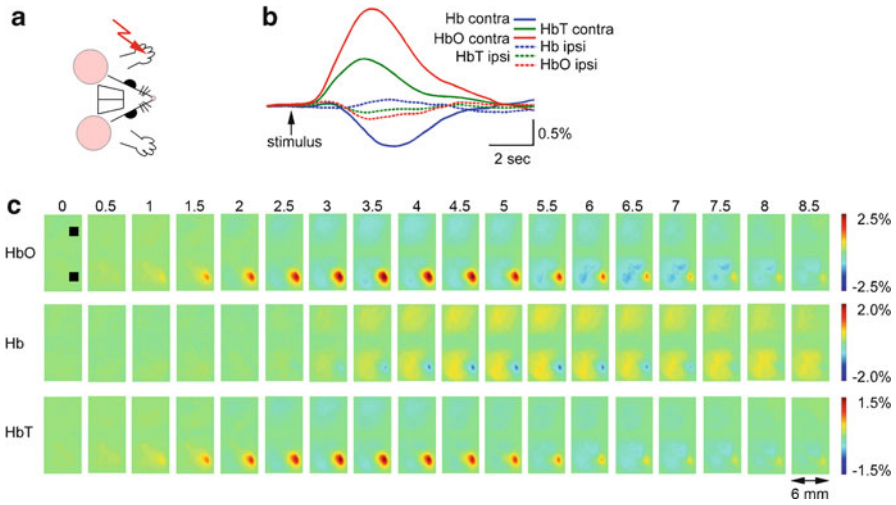

Fig. 15.14 Bilateral spectral imaging of blood oxygenation and volume in response to somatosensory stimulation. (**a**) A schematic representation of bilateral experimental paradigm. SI is exposed on both sides. The signals are imaged bilaterally in the response to stimulation of one (*left*) forepaw. (**b**) Time-courses of contralateral and ipsilateral signal in response to electrical forepaw stimulus (2 s, 3 Hz) extracted from regions of interest (ROIs) shown in (**c**). The contralateral response is shown by solid lines, the ipsilateral response is shown by dotted lines. Colorcode: Hb, blue; HbO, red; HbT, green. (**c**) Spatially smoothed ratio images of Hb, HbO and HbT response. Times in seconds relative to the stimulus onset are denoted above the images. Each image corresponds to the signal during the activation divided by the prestimulus baseline. The black rectangles denote the ROIs centered on the earliest detectable HbT response. For more information see (Devor et al. 2007; Devor et al. 2008b)

dilation or constriction of nearby arterioles (Cauli et al. 2004; Rancillac et al. 2006). *In vivo* studies in the primary somatosensory cortex (SI) in the rat, using spectral and laser speckle optical imaging, VSD and 2-photon microscopy, have demonstrated that a decrease in blood oxygenation and flow (Fig. 15.14) correlated with arteriolar constriction (Fig. 15.15) and increased neuronal inhibition (Fig. 15.16) (Devor et al. 2007; Devor et al. 2008b). This is in agreement with a previous fMRI study that showed a correspondence of negative BOLD to neuronal inhibition (Shmuel et al. 2006). The vasoconstriction was abolished by blocking of neuronal activity (Devor et al. 2008b) and was found on the arterial side while venous diameters stayed unchanged (Hillman et al. 2007; Tian et al. 2008). These findings suggest an active process rather than a passive "blood steal". This conclusion was further supported by a modeling study using VAN (Boas et al. 2008).

In healthy cortical circuits excitation is always coupled to inhibition. In SI, the balance between excitation and inhibition is temporary tilted during a response to a sensory stimulus to generate a net increase in excitation followed by a net increase in inhibition (Simons and Carvell 1989; Moore and Nelson 1998; Pinto et al. 2000; Derdikman et al. 2003). This can be easily observed with VSD that report mostly synaptic polarization changes of apical pyramidal dendrites (Ferezou et al. 2006)

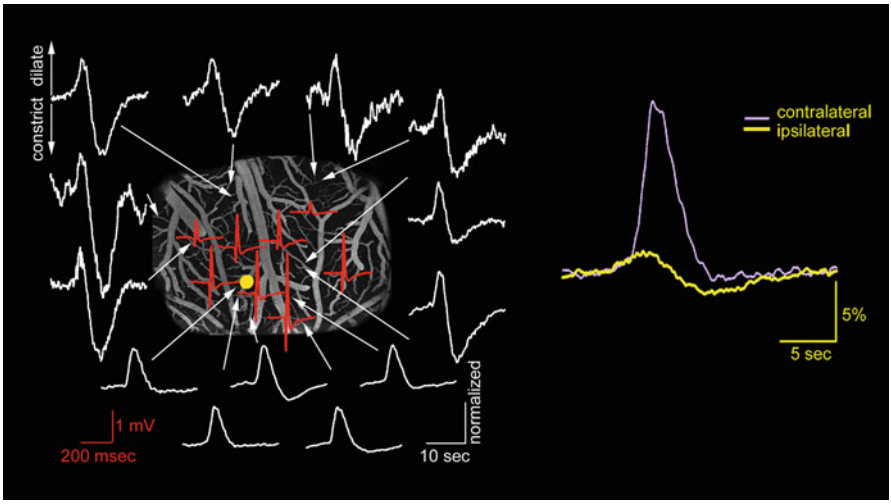

Fig. 15.15 Two-photon imaging of vascular dilation and constriction to a somatosensory stimulus. *On the left:* Diameter changes were measured in single surface arterioles in response to electrical stimulation of contralateral forepaw (1 s, 3 Hz). Increase in the diameter is plotted upward, and decrease is plotted downward. The time-courses are normalized by the peak dilation amplitude. Electrophysiological response to the stimulus was mapped using a ball electrode. Recorded surface potentials (*red traces*) are overlaid on the image of the brain surface vasculature. Both vasodilatation and vasoconstriction are present at all locations. The degree of vasodilation decreases with an increase of distance from the center of neuronal activity (the largest surface potential amplitude). *On the right:* arteriolar diameter changes in response to contralateral stimulus (*blue*) and ipsilateral stimulus (*yellow*) measured at the location marked by a yellow dot on the image of the brain vasculature. For more information see (Devor et al. 2007; Devor et al. 2008b)

(Fig. 15.16). Importantly, neuronal activity is fast, so that both the excitatory and inhibitory phases of the neuronal response occur before the onset of blood flow response. Thus, the vasculature reacts "at once" to the accumulated transmitters released during both phases of neuronal response. This is the main rational behind integration of neuronal measurements over the time window of the response in studies that compared neuronal and hemodynamic measurements over a range of stimulus conditions (Devor et al. 2003; Devor et al. 2005). For example, in SI a sensory stimulus usually elicits an increase in MUA during the VSD depolarization followed by a very small decrease that occurred during the VSD hyperpolarization (Fig. 15.17). The decrease might be below the detection threshold for low-impedance laminar electrodes with large recording contacts, but can be observed using high-impedance electrodes with small tips. However, since the decrease is small, the integral MUA response would indicate an overall increase in neuronal firing (as was discussed above, cell-type specific firing rates cannot be inferred from MUA alone, see Sect. 15.3.2.3).

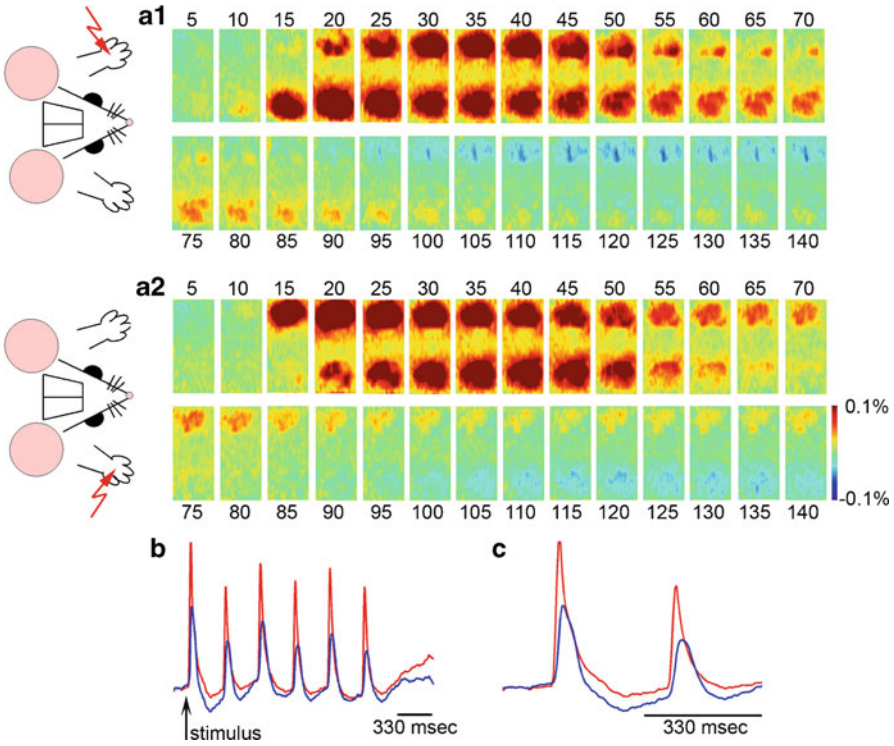

Fig. 15.16 Bilateral VSD imaging of neuronal polarization changes following a somatosensory stimulus. (**a**) Temporal evolution of VSD response to electrical forepaw stimulation (2 s, 3 Hz). The response to the first stimulus in the train is shown. Times relative to the stimulus onset are indicated above the images. A1 and A2 show the response to stimulation of left and right forepaw, respectively. (**b**) Signal time-course extracted from the contralateral (*red*) and ipsilateral (*blue*) hemispheres. The ROIs are shown by red dotted line in A1. (**c**) Zoom in on the response to the first two stimuli. For more information see (Devor et al. 2007; Devor et al. 2008b)

Moreover, synaptic inhibition does not necessarily have to be accompanied by a decrease in firing rate. For example, inhibitory inputs to apical dendrites of layer V pyramidal cells are far enough from the cell body, so that hyperpolarization decays along the membrane before reaching the cell body. Therefore, the hyperpolarization of dendrites in layer I might not affect the generation of action potentials that happens in the initial segment of the axon emerging from the cell body in layer V. Under these conditions, an increase in inhibition would not reduce the firing rate. On contrary, since the inhibitory synaptic inputs result from firing of local inhibitory interneurons, the overall firing might increase.

With respect to the role that neuronal transmitters play in communication of neuronal activity to the nearby arterioles (Cauli et al. 2004; Hamel 2004, 2006; Rancillac et al. 2006), some neurotransmitters are directly vasoactive (Cauli et al. 2004; Hamel 2004, 2006) or trigger a synthesis of vasoactive messengers. For example, the major

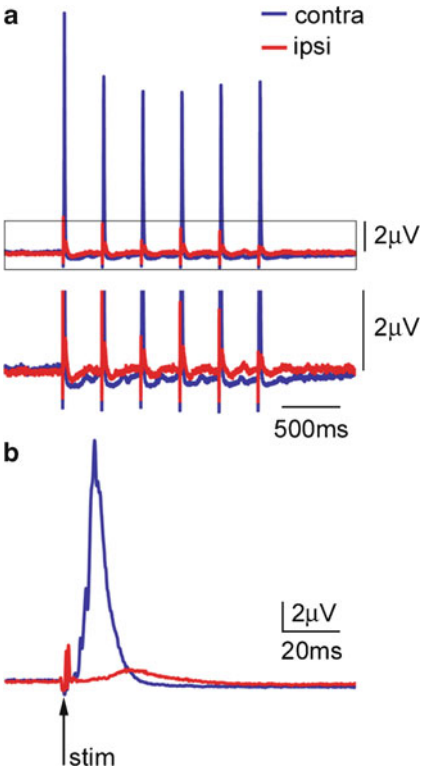

Fig. 15.17 Changes in population firing rate in response to a somatosensory stimulus. (**a**) MUA in response to an electrical forepaw stimulation (2 s, 3 Hz). The response was averaged across the cortical depth to improve signal-to-noise ratio. Responses to contra- and ipsilateral stimuli are superimposed (blue and red, respectively). The part within a rectangle is expanded below. A small decrease in MUA is evident for both stimulus conditions. (**b**) The response to the first stimulus in the train is expanded. Black arrow points to a stimulus artifact indicating stimulus onset

excitatory neurotransmitter, glutamate, causes activation of NMDA receptors that elevate intracellular concentration of calcium and trigger synthesis of a vasodilator nitric oxide (NO) by a neuronal enzyme called nitric oxide synthase (nNOS) (Iadecola and Niwa 2002). Moreover, it has been shown that released glutamate activates astrocytes that can release additional dilators (see Sect. 15.4.3 below) (for recent reviews see (Iadecola and Nedergaard 2007; Koehler et al. 2009)). Thus, neuronal excitation is expected to cause dilation of surround arterioles.

Application of $GABA_A$ agonist muscimol has been reported to cause dilation in brain slices (Fergus and Lee 1997). However, inhibitory interneurons release not only GABA but also other signaling molecules called neuropeptides. In particular, firing in cortical interneurons containing neuropeptides somatostatin and neuropeptide Y was shown to cause arteriolar vasoconstriction *in vitro* (Cauli et al. 2004). The majority of these interneurons, namely Martinotti cells, extend their axons to neighboring cortical columns and thus are in a good position to mediate the phenomenon known as "surround inhibition" (Simons and Carvell 1989; Takashima et al. 2001; Derdikman et al. 2003; Devor et al. 2007). Therefore, activation of these neurons is expected to result in surround vasoconstriction. In this respect, *in vivo* imaging data demonstrated that surround inhibition was correlated with arteriolar vasoconstriction

and a decrease in blood oxygenation, or "negative BOLD" (Devor et al. 2007; Boas et al. 2008). Nevertheless, direct *in vivo* evidence showing that selective activation of Martinotti cells, or release of somatostatin, correlates with vasoconstriction is missing.

Assuming that neurotransmitter/neuropeptide release during synaptic transmission might be a critical factor in generation of the hemodynamic response (Cauli et al. 2004; Hamel 2004, 2006; Rancillac et al. 2006), activation of the same cortical circuit by different inputs can lead to different degrees of vasodilation and vasoconstriction, reflecting differential engagement of particular cell types. *In vivo* data are consistent with this hypothesis. Specifically, vasodilation and an increase in blood flow were observed in the forepaw area of SI following stimulation of the contralateral forepaw, while the same area showed vasoconstriction and a decrease in flow following stimulation of the ipsilateral forepaw. In the former, the circuit was excited by thalamic inputs to layer IV, whereas in the latter the ipsilateral SI was activated via transcallosal afferents synapsing below and above layer IV (Wise and Jones 1976; White and DeAmicis 1977; Koralek et al. 1990).

15.4.2 Linearity of Neurovascular Coupling and the Relationship between the Hemodynamic Signals and MUA/LFP

A number of previous studies from our group and others suggest a complex relationship between neuronal firing (MUA) and LFP on the one hand, and the hemodynamic response on the other (Table 15.1, finding 3). These studies have shown that the degree of linearity in neurovascular relationship depends strongly on the stimulus paradigm (Sheth et al. 2004), and that important discrepancies between hemodynamic and electrophysiological measures can be observed under certain conditions (Devor et al. 2008b). Yet, as we have discussed above, it is likely that activation of specific types of neurons as opposed to the dynamics of multiunit spiking or synaptic activity is likely to determine the vascular response.

The following example demonstrates that not only the inverse solution (prediction of MUA and LFP from the hemodynamic response) is an ill-defined problem, but even the forward solution (prediction of the hemodynamic response given the MUA and LFP) can be ambiguous without *a priori* knowledge of stimulus conditions. In this example, paired tactile stimuli were delivered to single whiskers at different time delays (Fig. 15.18a). Electrophysiological recordings of MUA and LFP were performed from layer II/III at the location of the maximal response to stimulation of the second whisker (the "principal barrel" of the second whisker). Spectral imaging of Hb, HbO and HbT were performed simultaneously with the MUA/LFP recordings. In Fig. 15.18b the peak response of Hb, Hb and HbT is plotted against the peak MUA and LFP. In contrast to other studies, the scatter plots in Fig. 15.18b cannot be approximated nether by a linear or any nonlinear continuous function.

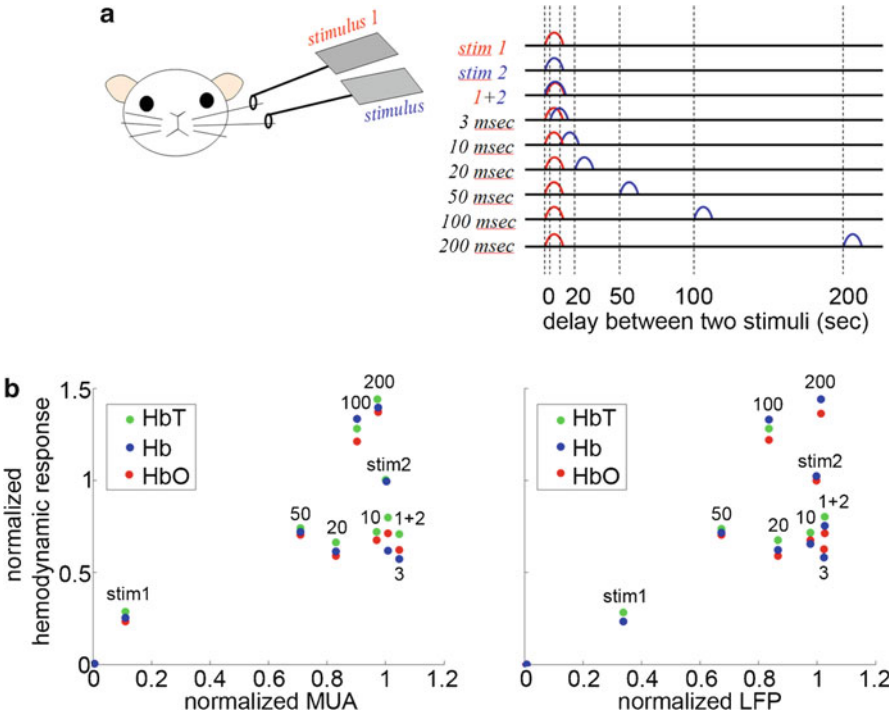

Fig. 15.18 Paired whisker stimulus paradigm with a varying delay. (**a**) Two single neighboring whiskers were stimulated at different delays. Stimulus conditions: first whisker alone, second whisker alone, both whiskers simultaneously, second following first after X msec delay where X = [3 10 20 50 100 200 500 800 1000 1500 2000]. (**b**) Hb (*blue*), HbO (*red*) and HbT (*green*) as a function of MUA (*left*) and LFP (*right*) across stimulus conditions. For each parameter all values are normalized to stimulation of the second whisker alone. Conditions are indicated above data points

What is so different about the paired whisker paradigm that makes it impossible to fit a curve to the relationship between the MUA/LFP and the hemodynamic parameters as has been done in other studies that varied stimulus amplitude, duration, and frequency? As we discussed above, the neuronal response to a sensory stimulus in SI is biphasic, consistent with an increase in excitation followed by an increase in inhibition. In the paired paradigm, the second whisker is deflected before the relaxation of the neuronal response to the first one. Thus, the response to the first whisker sets up neuronal activity, and the response to the second whisker rides on top of this on-going activity, either net excitatory or net inhibitory depending on timing. As different neuronal cell types vary in their frequency response, excitability and relaxation time, stimulation of the second whisker at different delays from the first results in differential engagement of particular cell types and, therefore, in a different hemodynamic response depending on the net neuronal activity. These cell-type specific differences cannot be easily extracted from measurements of MUA and LFP, in particular if only a single-location LFP measurement is available.

In contrast, if we knew the behavior of the neuronal circuit under each one of the stimulus conditions and could reconstruct the activity of each one of the vasoactive cell types, it is conceivable that we could predict the corresponding vasodilation and vasoconstriction.

The issue of linearity of neurovascular coupling is sometimes being confused with the issue of additive properties of hemodynamic responses. Anders Dale and colleagues used one, two and three separate short-lasting visual stimuli to test the former (Dale and Buckner 1997). Individual stimuli were spaced far enough in time to allow relaxation of the neuronal activity between the stimuli. Under these conditions, they were able to confirm that the hemodynamic response to two consecutive stimuli could be modeled as a sum of the responses to each of the stimuli alone. These and other experiments showed that using a rapid presentation, hemodynamic response to each stimulus condition can be recovered as long as neuronal activity recovers between the consecutive stimuli (in the case of the paired whisker paradigm, neuronal activity has to recover between one paired stimulus to the next).

Thus, testing the linearity of neurovascular coupling does not require long interstimulus intervals: the interval just has to be long enough to allow neuronal relaxation. For example, if neuronal activity X evokes hemodynamic response Y, a series of two separate X events with a complete neuronal relaxation between them will evoke a linear sum of Y in the response to the fist X and another Y in the response to the second X. However, if the neuronal activity changes in amplitude to 2X, the hemodynamic response can be either 2Y (linear coupling), <2Y (sublinear), or >2Y (supralinear).

15.4.3 Astrocytes as Neurovascular Mediators

A growing body of literature indicates that astrocytes not only provide a metabolic support for neurons (Magistretti et al. 1999; Rouach et al. 2008) but also release vasoactive molecular mediators ("gliotransmitters") and thus can play a key role in neurovascular communication (Table 15.1, findings 4 and 5) (for recent reviews see (Agulhon et al. 2008; Koehler et al. 2009)). Anatomically, the astrocytes are well-positioned to serve as a bridge between neurons and blood vessels, with processes associated with neuronal synapses and processes that contact the blood vessels (Fig. 15.19). Experiments in brain slices have shown that astrocytes respond to neuronal activity by elevation in intracellular calcium concentration (Simard et al. 2003; Zonta et al. 2003; Gordon et al. 2008). Although astrocytes express receptors for numerous neurotransmitters and neuropeptides, most of the studies have focused on glutamate. Specifically, it has been shown that glutamate activates metabotropic receptors (mGluR) that cause calcium influx from intracellular stores (Porter and McCarthy 1996; Zonta et al. 2003). In addition, activation of astrocytic GABA receptors also has been shown to produce calcium transients (Nilsson et al. 1993). Other receptors, including ACh, NA, VIP, somatostatin and more, are less understood although most of them are also metabotropic and their activation is expected

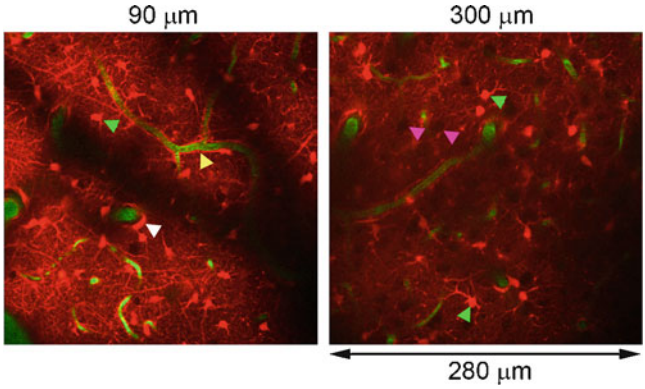

Fig. 15.19 Astrocytic endfeet outline microvasculature. Two single images of astrocytes (labeled with SR101, *red*) and blood vessels (labeled by intravascular fluorescein dextran, *green*) at different depths. Astrocytes (*green arrowheads*) are present throughout the cortical depth; their endfeet wrap around diving arterioles (*white arrowhead*) and capillaries (*yellow arrowhead*). Neurons are not labeled and appear as black holes (*magenta arrowheads*)

to elevate astrocytic calcium concentration. The elevation of intracellular calcium in turn can trigger synthesis and release of gliotransmitters. Both dilators (epoxyeicosatrienoic acids (EETs) and prostaglandins) and constrictors (20-hydroxyeicosatetraenoic acid (20-HETE)) are synthesized in calcium-dependent manner from common precursors (reviewed in (Straub and Nelson 2007)). In fact, slice studies demonstrated that elevation of astrocytic calcium (spontaneous or evoked by neuronal activity) can cause both dilation and constriction of nearby arterioles (Zonta et al. 2003; Mulligan and MacVicar 2004). Since astrocytes are coupled by gap junctions, signals can propagate throughout the astrocytic network and thus might be involved in propagation of vascular response along the vessels. Some of the variability in vascular response observed in slices (dilation or constriction) can be explained by the baseline state of smooth muscle cells in the absence of normal blood pressure and flow (Blanco et al. 2008). An *in vivo* study have has supported the finding that astrocytic calcium increase has vasoactive consequences (usually dilation, but rare case of constriction were also observed) (Takano et al. 2006).

Furthermore, natural sensory stimulation *in vivo* induces transient calcium responses both in neurons and astrocytes (Wang et al. 2006; Schummers et al. 2008). In the majority of these studies, astrocytic calcium transients were significantly delayed with respect to the onset of stimulation, neuronal response, and known dynamics of vascular responses. In fact, a recent study in ferret visual cortex, where both calcium and hemodynamic responses were measured, reported an increase in blood volume preceding an increase in astrocytic calcium by several seconds (Schummers et al. 2008) (see also (Koehler et al. 2009) for further discussion on the discrepancy of astrocytic and blood flow response time scales). Moreover, laser Doppler studies suggest that blocking astrocytic transmission does not affect the blood flow response during the first couple of seconds, but reduces the amplitude of

the flow response during prolong stimulation (Liu et al. 2008; Shi et al. 2008). Finally, arteriolar smooth muscle cells express a variety of receptors for neurotransmitters and neuropeptides suggesting that vascular diameters can be regulated independently of astrocytic activity (Hamel 2006).

One study stands apart from others with respect to the kinetics of astrocytic calcium response (Winship et al. 2007). This study reported that a small percent of astrocytes exhibited a fast response to whisker stimulation similar to nearby neurons. The astrocytes in this study were identified based on labeling with SR101. This opens a possibility of heterogeneity within the astrocytic population. The other possibility is that a small percent of SR101 labeled cells were actually neurons. While it has been shown that SR101 exclusively labels astrocytes using topical loading, Winship et al. (2007) injected the dye into the tissue that might have resulted in a small percent of neuronal uptake. The apparent fast response in a small number of astrocytes could also result from a technical error related to the employed subtraction procedure. Nevertheless, it is possible that astrocytes are heterogeneous across and within cortical layers. For example, we know that neurons in layer IV have higher metabolism than in other layers reflected by higher density of cytochrome oxidase (Woolsey et al. 1996). Thus, it is conceivable that astrocytes in layer IV might have faster or more efficient responses to elevated neuronal activity. Noteworthy neurovascular coupling can differ between brain regions, e.g., between SI and the olfactory bulb (Petzold et al. 2008).

15.4.4 Is There a Feedback Vasodilation Signaling Related to Increased Metabolism?

Theoretically, blood flow response can be controlled not only in a feed forward manner via neuronal release, but also by a feedback from accumulation of energy metabolites related to increased neuronal activity. In fact, coupling of blood flow and glucose metabolism is always assumed as a general rule in PET literature (Fox and Raichle 1986; Fox et al. 1988; Raichle and Mintun 2006). However, a recent study, using electrophysiological and optical imaging methods and 2-deoxyglucose (2DG) autoradiography, suggests that blood flow response is not coupled to glucose consumption under all conditions (Devor et al. 2008b). In this study, 2DG uptake was examined bilaterally following stimulation of one (right) forepaw. The results showed a bilateral increase in glucose consumption with a small but significant increase in the ipsilateral SI (Fig. 15.20, red arrows; for statistical quantification see (Devor et al. 2008b), their Fig. 15.5). The authors ruled out potential neuronal deactivation or blood stealing effects by showing that vasoconstriction was observed on arterial side, depended on local neuronal activity, and was observed in the presence of increased MUA (reflecting the spiking response both excitatory and inhibitory cells). Voltage-sensitive dyes imaging data, acquired under the same stimulus conditions, showed that vasoconstriction and negative hemodynamic response can be explained by an increased engagement of synaptic inhibition ((Devor et al. 2008b),

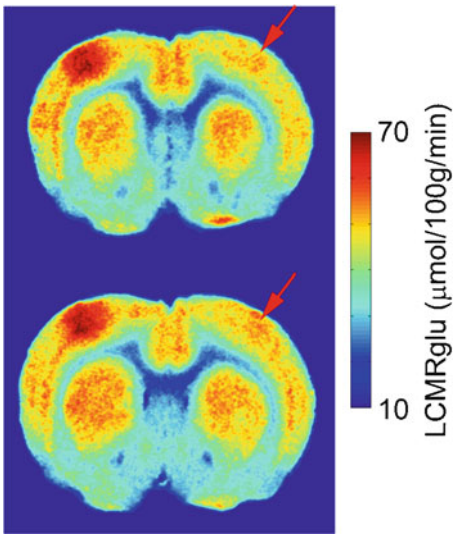

Fig. 15.20 2DG-autoradiography in response to a unilateral stimulation. Consecutive non-adjacent coronal brain sections through the forepaw region of SI are shown. The color scale is expressed in units of local cerebral metabolic rate of glucose, LCMRglu (μmol/100 g/min). *Red arrows* point to a weak ipsilateral label uptake

their Supplementary Fig. 15.2). Moreover, increased inhibition was a common denominator between the ipsilateral results in Devor et al. (2008b) and their previous study considering the "surround" contralateral SI region (Devor et al. 2007). These data are consistent with the idea that some of the inhibitory vasoactive messengers (e.g., somatostatin or neuropeptide Y) can actively cause vasoconstriction and "negative BOLD". Dissociation of vascular and metabolic responses in the ipsilateral SI finding does not rule out the possibility that certain metabolites can have a vasoactive effect (Ido et al. 2004; Mintun et al. 2004; Gordon et al. 2008). Rather, it indicates that blood flow response is not determined by the tissue energy consumption and other factors, such as release of neurotransmitters and neuropeptides, can play a dominant role in the regulation of blood flow (Table 15.1, finding 6).

It has been showed that neuronal stimulation produces adenosine, a potent vasodilator (Rubio et al. 1975). However, most of adenosine release in healthy brain is associated not with ATP utilization but with propagation of vasodilation along arteriolar walls (Iliff et al. 2003; Ohata et al. 2006). Thus, the involvement of adenosine in functional increases in CBF *per se* does not support the "metabolic" hypothesis but rather illustrates the importance of propagation of dilatory response from microvasculature to feeding vessels on the pial surface. Nevertheless, adenosine and energy metabolites, such as a glycolytic product lactate, might play a key role in dilation response under pathological conditions. For instance, it has been demonstrated that extracellular adenosine and lactate facilitate dilation *in vitro* under hypoxia (Gordon et al. 2008).

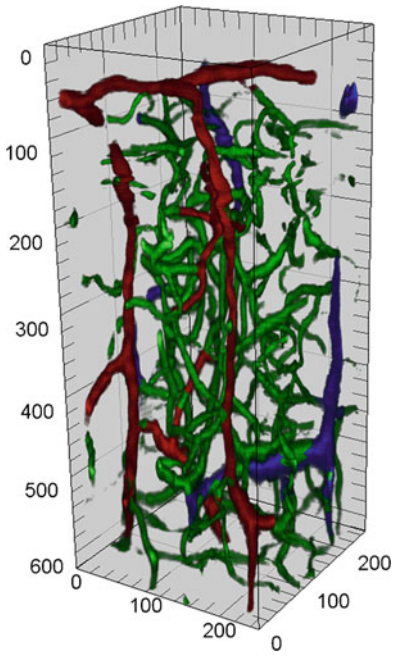

Fig. 15.21 Reconstruction of microvasculature within a 250 × 250 × 600 µm cube of SI cortical tissue. Arterioles are in red, veins in blue and capillaries in green. Top corresponds to the cortical surface

15.4.5 Compartment- and Depth-Specificity of the Vascular Response

In cerebral cortex, pial arteries give rise to smaller arterioles that dive into the cortex at a close to 90°angle. The diving arterioles branch as they dive to feed the local capillary beds. Venules and veins collect the deoxygenated blood from the capillaries and bring it back to the cortical (pial) surface (Fig. 15.21). Thus, measurement modalities with a limited depth penetration and no laminar resolution, such as optical imaging of intrinsic signals, are biased to the largest arteries and veins that lie on the pial surface. However, dilation of feeding arteries and oxygenation changes in draining surface veins are delayed relative to the onset of dilation in tissue microvasculature (Tian et al. 2008). Therefore, not only the initial dip (Malonek and Grinvald 1996) but also the initial changes in HbT can be used for localization of neuronal activity. In fact, examination of the temporal evolution of ratio images (divided by the baseline image) reveals than the first detectable HbO and HbT signals are well localized. As the dilation propagates to the surface, the pial arteries become visible (Fig. 15.22, red arrowheads). The draining veins appear later in images of HbO and Hb (Fig. 15.22, black arrowheads). Speckle contrast images are noisier and, therefore, the surface vasculature is less visible.

In contrast to optical imaging of intrinsic signals, 2-photon microscopy provides the ultimate single-vessel resolution down to ~ 600 µm below the surface. Two-photon

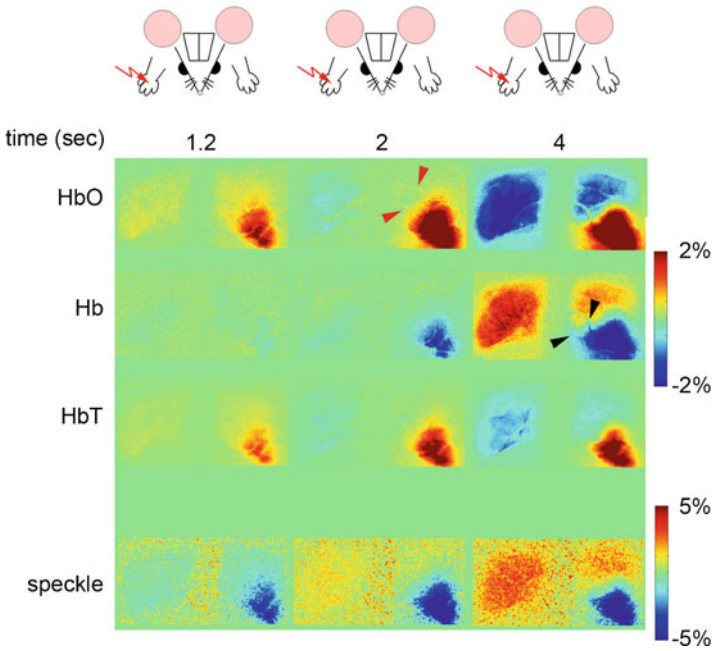

Fig. 15.22 Evolution of intrinsic imaging signals in response to a forepaw stimulus. Bilateral ratio images of HbO, Hb, HbT and speckle contrast are shown. Red and black arrows point to the surface arteries and veins, respectively. Negative change in speckle contrast corresponds to an increase in speed of RBCs (an increase in CBF)

measurements indicate that both arteries/arterioles and capillaries have a biphasic response to stimulus with initial dilation followed by a constriction (Devor et al. 2007; Boas et al. 2008; Devor et al. 2008b; Tian et al. 2008) (Table 15.1, finding 7). Arteriolar walls contain smooth muscle cells and their diameter can be actively controlled by vasoactive mediators (for review see (Iadecola 2004; Lauritzen 2005; Hamel 2006)). Recently, it has been shown in a brain slice preparation that capillary diameters can be actively controlled by perycites - single-cell contractile cells found most often at capillary branching points. This mechanism might be responsible for the capillary dilation observed *in vivo* (Stefanovic et al. 2008; Tian et al. 2008).

Although venules and veins are not surrounded by a wall of smooth muscle cells and cannot dilate actively, it has been proposed that they can passively swell during a functional increase in CBF (Buxton et al. 1998; Mandeville et al. 1999). In fact, a hypothetical increase in venous volume has been used to explain some prominent features of BOLD response, such as “post-stimulus undershoot” (Buxton et al. 1998). Recent experimental studies using 2-photon imaging found no indication of change in venous diameters (Table 15.1, finding 8) (Hillman et al. 2007; Tian et al. 2008). These findings are consistent with observations based on another optical technology, Laminar Optical Tomography (LOT) (Hillman et al. 2004; Hillman et al. 2007),

and also with intrinsic (spectral) imaging data (Vanzetta et al. 2005). Interestingly, 2-photon imaging of small surface venules in rat SI provided evidence of an increase in density of RBCs ("hematocrit") in response to a somatosensory stimulus (Hillman et al. 2007).

Because the largest veins run on the pial cortical surface, oxygenation changes detected from the top cortical layer are expected to be delayed relative to deeper layers (Hillman et al. 2007). In addition, our recent *in vivo* 2-photon data demonstrate that dilation propagates to the surface from deeper layers (Tian et al. 2008) (Table 15.1, finding 9). These studies raise a possibility of laminar differences in functional dilation onset. These findings are in agreement with our recent OCT study that observed a delayed response in superficial cortical regions (<200 μm) consistent with retrograde ("upstream") vasodilation (Chen et al. 2008). Importantly, propagation of neuronal activity within a cortical column happens within a couple of milliseconds. The hemodynamic response is much slower: the onset of dilation in response to a brief single-whisker deflection occurs well past the return of neuronal activity to the baseline. For that reason, any laminar hemodynamic/vascular delays are unlikely to be explained by neuronal propagation between cortical layers: on the hemodynamic time scale, neurons respond virtually simultaneously throughout the cortical depth.

15.4.6 Oxygen Availability on the Microscopic Scale

As we discussed in Sect. 15.3.3.2, there are no tools today that allow a direct and dynamic measurement of O_2 consumption. However, O_2 availability has been measured in a number of ways. A number of recent studies have employed polarographic sensors, also called "O_2 electrodes", to measure a partial pressure of O_2 (pO_2) in the tissue (Thompson et al. 2003; Viswanathan and Freeman 2007). These studies demonstrated a drop in tissue pO_2 confined to areas of SI receiving direct thalamic inputs (principal cortical columns). This initial pO_2 drop has been interpreted as an increase in O_2 consumption prior to an increase in CBF, analogous to the "initial dip" often observed by intrinsic optical imaging (Malonek and Grinvald 1996). A followed increase in pO_2 presumably reflected vasodilation and an increase in CBF. While these findings are in general register with intrinsic imaging studies, some timing discrepancies exist. Specifically, the decrease in tissue pO_2 has been reported lasting as long as 10 s (Viswanathan and Freeman 2007), considerably longer than what is usually observed optically (Vanzetta and Grinvald 2001). Some of this can be explained by a slow reaction time of pO_2 sensors. Moreover, the pO_2 measurements can vary considerably depending on micropositioning of the sensor, and sensors need to be calibrated frequently.

Optical measurements of O_2 using phosphorescent lifetime probes are still in infancy, but new and better dyes are being developed and tested (Vanzetta and Grinvald 1999; Dunphy et al. 2002). In contrast to O_2 electrodes, O_2-dependent quenching of phosphorescence can provide a 2-dimensional map of both intravascular

pO_2 if injected i.v. and extravascular pO_2 if microinjected in the tissue. Moreover, phosphorescence lifetime can be combined with 2-dimensional imaging of blood flow using simultaneous laser speckle contrast imaging (Sakadzic et al. 2009). Simultaneous acquisition of spatiotemporal maps of pO_2 and blood flow during functional activation is critical to distinguish between the contribution of CBF and oxygen consumption to functional changes in hemoglobin oxygenation, such as BOLD response. In fact, measurement of pO_2 alone cannot be used to infer neither BOLD response, nor tissue O_2 metabolism. For example, an increase in CBF in areas of baseline neuronal activity (no evoked neuronal response) would lead to an increase in measured tissue pO_2. Thus, one has to measure both O_2 availability and blood flow to predict BOLD or draw conclusions regarding $CMRO_2$.

A couple of recent studies used optical imaging of NADH that provides an indirect tool for looking at processes related to O_2 consumption. Interpretation of NADH images is challenging due to a complex relationship between the cellular processes both producing and oxidizing NADH to a non-fluorescent NAD^+ (for a recent review see (Turner et al. 2007)). Specifically, NADH (and pyruvate) is produced in the cytosol during glycolysis and oxidized during conversion of pyruvate to lactate. NADH is also both produced and oxidized in the mitochondria (during the TCA cycle and oxidative phosphorylation, respectively). If all processes would happen simultaneously and at the same rate, one might expect to see no change in NADH fluorescence. However, thermodynamic studies show that glycolysis occurs faster than the conversion of pyruvate to lactate and empirical optical data show that changes in NADH fluorescence can be observed in neurons and astrocytes following an increase in neuronal activity (Kasischke et al. 2004; Takano et al. 2007). In register with the idea that neurons use mostly oxidative phosphorylation while astrocytes use mostly glycolysis (Magistretti et al. 1999), 2-photon NADH imaging in astrocytes in brain slice preparations revealed an early dip in NADH fluorescence, sensitive to blocking of postsynaptic neuronal activity, followed by an increase in fluorescence in astrocytes (Kasischke et al. 2004). Further *in vivo* 2-photon studies with cellular resolution are needed to elucidate NADH dynamics in neurons and astrocytes under healthy conditions.

In the classical view, the extraction of O_2 and glucose into the tissue occur at the capillary level. However, recent optical data suggest that O_2 travels into the tissue also through the walls of penetrating arterioles and their branches (Hillman et al. 2007; Kasischke et al. 2011; Takano et al. 2007) (Table 15.1, finding 10). Future modeling studies are required to determine to what extent this effect would contribute to the macroscopic BOLD signal (Fig. 15.23).

15.5 Open Questions and Outlook

The methods described above provide a powerful battery of tools for developing a deeper understanding of the fundamental physiological mechanisms linking neuronal activity, blood flow and energy metabolism. A central goal of understanding

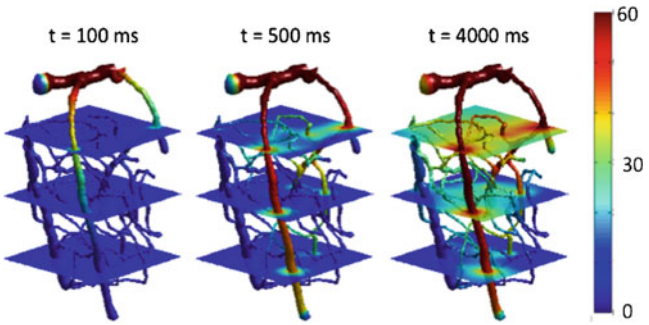

Fig. 15.23 VAN simulation of tissue pO_2. VAN simulation in a 250×250×450 μm subset following an inflow of O_2 from a pial artery at t=0 ms. Baseline pO_2 was 10 mmHg. A steady-state pO_2 is achieved within 4 s

these basic mechanisms is to lay a firm foundation for interpreting noninvasive functional neuroimaging data in humans, with the BOLD effect as a primary example. Given the widespread use of BOLD imaging for brain mapping studies, it is remarkable how small an impact it has had on clinical practice. A key problem is that, because of the physiological complexity of the BOLD response, it is difficult to interpret the magnitude of the response in a quantitative, physiologically meaningful way. For this reason BOLD-fMRI provides a robust index of where neuronal activity is changing, but it is much more difficult to interpret the magnitude, and even polarity, of the change. So it is not surprising that the most promising clinical applications of fMRI to date have been in pre-surgical planning, where the central question is the location of activity changes. However, because the BOLD response is sensitive to key physiological variables (CBF and $CMRO_2$), there is the potential for the development of fMRI into a quantitative probe of physiological function.

Quantitative applications of fMRI require a multi-modal imaging approach. A simple example described earlier is how the combination of a CBF measurement with a BOLD measurement in the calibrated BOLD experiment can yield an estimate of the $CMRO_2$ change, more than either measurement alone provides. The key to achieving such gains with multi-modal imaging, though, is a comprehensive theoretical framework that accurately describes the dependence of each of the measured signals on the underlying physiological variables. To establish that theoretical framework requires systematic studies in animal models to address key questions. For our example of quantitative BOLD imaging, a central concern is the role played by blood volume changes in affecting the signal. Changes on the capillary or venous side could alter the local deoxyhemoglobin content, altering the signal through a BOLD mechanism, but in addition arterial volume changes also could affect the measured signal by exchanging blood and extravascular water carrying different MR signals. To accurately model these effects requires a detailed understanding of volume and hematocrit changes at each stage of the vascular tree (Hillman et al. 2007; Srinivasan et al. 2009). This information can be provided by 2-photon microscopy,

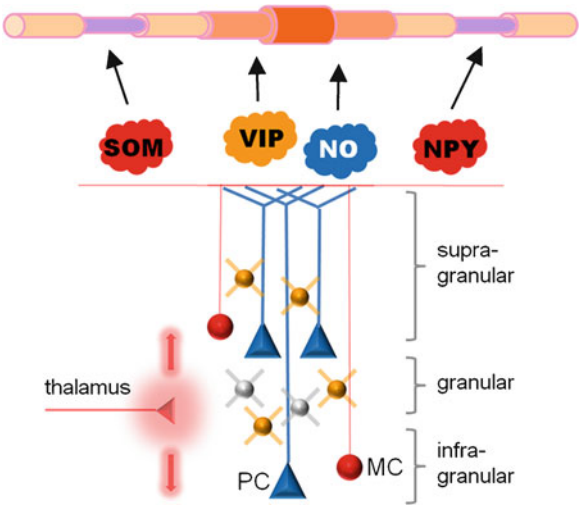

Fig. 15.24 A cartoon of cerebral vasoactive circuit. PC: pyramidal cell; MC: Martinotti cell

and integrated within a multi-scale vascular model, such as the VAN model, to produce macroscopic average behavior appropriate for the spatial scale of imaging. The same approach can be used to address other modeling assumptions noted in Sect. 15.3.

An important area where detailed studies in animal models can shed light on the interpretation of the BOLD response is in understanding the dynamics. Quantitative BOLD applications in human tend to focus on steady-state changes, but the BOLD response exhibits rich dynamics that are still poorly understood. Phenomena such as the initial dip, the post-stimulus undershoot, and the dependence of the time scale of the dynamics on the baseline state are all measurable in human subjects, but still poorly understood in terms of the underlying physiology. Dynamic studies such as those described above will be able to characterize the dynamics of vascular volume at all levels of the vascular tree, as well as the dynamics of CBF and $CMRO_2$ changes. Combined with an appropriate vascular model these measurements will provide a deeper understanding of the origins of these dynamic features of the BOLD response.

According to our current working hypothesis on dynamic regulation of CBF in SI, vasodilation and vasoconstriction result from activation of distinct neuronal subpopulations through release of an array of vasoactive agents (Fig. 15.24). Specifically, the biphasic behavior of arteriolar diameter change observed with 2-photon microscopy is consistent with a "push-pull" mechanism where simultaneously released dilatory and constrictive agents compete as antagonistic forces, with their strengths proportional to the number of released molecules (Devor et al. 2007; Devor et al. 2008b). In agreement with this idea, a simple computational analysis in Devor et al. (2007) shows that the biphasic diameter changes can easily be obtained as a weighted sum of a dilatory and constrictive effects with very similar time-courses and simultaneous onset times.

Figure 15.24 illustrates the idea of the cell-type specific control of cerebral CBF in SI with respect to an incoming sensory input (this figure by no means provides a summary of all the relevant molecular messengers or vasoactive cell types). In SI, thalamic afferents terminate in layer IV (Fig. 15.24, "granular"), and excitation propagates fast up and down the column (red arrows) and to the surround columns. The excitation is always coupled with inhibition because of the wiring of cortical circuits (Lefort et al. 2009). Arteriolar dilation is dominated by excitation in pyramidal cells (PC, Fig. 15.24) and release of glutamate with a subsequent release of NO (via activation of NMDA receptors in NOS-positive neurons), accompanied by release of other dilators such as VIP from VIP-positive interneurons and possibly GABA. Arteriolar constriction, on the other hand, is driven by mainly by activation of somatostatin- and neuropeptide Y-positive inhibitory interneurons, e.g., Martinotti cells (MC, Fig. 15.24).

Cortical columns receiving direct thalamic inputs, respond to a sensory stimulus with a net excitation, while columns in the surround and also those in ipsilateral SI respond with a net inhibition. Although not all inhibitory transmitters are contractile, a net increase in spiking of the inhibitory interneurons might increase the relative strength of the vasoconstrictive force. It has been argued that the hemodynamic response is better correlated with synaptic activity than with spiking (Logothetis 2002). Given that 95% of synapses in primary somatosensory cortex (SI) are local, firing of neurons is expected to be tightly coupled to release of the respective neuro transmitters that drives dilation and constriction (directly or via astrocytes).

Ideally, we would like to directly and simultaneously record neuronal activity for each cell type to reconstruct the release of all the relevant transmitters. Currently this is not feasible using the available experimental tools. However, population-specific activity can be extracted using neuromodeling approaches such as LPA. Moreover, computational methods such as LPA are required for extraction of cell type-specific population activity from macroscopic EEG/MEG data. The general idea is that if we could model the relationship between these macroscopic neuronal measures and activity in specific cell types and given known vasoactive effect of each neuronal population, we could predict macroscopic vascular response from macroscopic measures of neuronal activity.

Although potential vasoactive neuronal cell types have been identified *in vitro* (Cauli et al. 2004), further *in vivo* studies are needed to validate these predictions. In this respect, a recent progress in genetic labeling and remote control of identified neuronal populations will play a central role in unraveling the vasoactive role of cell types with known phenotypes. Inhibitory neurons of the same cell types are coupled by electrotonic junctions and thus discharge synchronously (Beierlein et al. 2000; Mann-Metzer and Yarom 2000; Deans et al. 2001; Beierlein et al. 2003). This synchronous discharge should produce synchronous release of vasoactive mediators leading to vasodilation or vasoconstriction. Thus, one can perform a spike-triggered averaging of vascular responses, with regard to spontaneous activity in a particular neuronal cell type. A complementary approach would be to test the relevant transmitters by local applications *in vivo.* Cell-type specific regulation of CBF would also imply that lessons learned from the cerebral cortex cannot be easily extrapolated

to other brain areas with different structures and signaling molecules such as cerebellum or basal ganglia. Indeed, dopaminergic transmission in basal ganglia is likely to play an important vasoactive role. In addition, projections from basal forebrain, raphe nuclei, locus coeruleus, and others might modulate the local vascular tone, CBF baseline and ΔCBF.

Key insights into regulation of CBF can be gained by studying vascular responses across the cortical depth and vascular compartments. In contrast to the previous attempts to differentiate compartment-specific responses while using technologies with low spatial resolution, 2-photon microscopy with the ultimate single-vessel resolution already produces some definite results regarding arteriolar and capillary response to a sensory stimulus under normal conditions (Chaigneau et al. 2003; Chaigneau et al. 2007; Devor et al. 2007; Devor et al. 2008b; Devor et al. 2008a) and redistribution of flow following an intervention (Nishimura et al. 2006; Schaffer et al. 2006; Nishimura et al. 2007). Given the current limitation of 2-photon penetration depth to ~600 μm (layer IV in a mouse), additional technologies are needed to reach the bottom cortical layers. In this respect, recent advances in OCT technology hold promise for imaging of dilation and flow throughout the cortical depth (Aguirre et al. 2006; Chen et al. 2008; Srinivasan et al. 2009; Srinivasan et al. 2010a; Srinivasan et al. 2010b). Specifically, knowledge of where dilation starts (e.g. in the capillary bed in layer IV) and how it propagates throughout the vascular network, will help in screening possible scenarios of neurovascular regulation using experimental or computational approaches.

Another consideration regarding screening possible scenarios of neurovascular regulation is related to time scales and baseline conditions. For example, most astrocytic imaging studies *in vivo* reported slow rises in intracellular calcium with delays considerably longer than known dynamics of hemodynamic/vascular responses (Schummers et al. 2008). It needs to be investigated further if astrocytes are a heterogeneous population with respect to their response kinetics, laminar distribution or metabolic efficiency (Winship et al. 2007). In brain slices, calcium waves have been shown to trigger vasodilation or constriction (Simard et al. 2003). However, because of the extremely slow vascular responses *in vitro*, the slice results are not conclusive in the context of time scales comparison. The other slice-related issue is pathological oxygenation conditions in the absence of hemoglobin circulation. In fact, it has been shown that lowering oxygenation in the bath from the usual 95% to 20% compromises neuronal activity in thin organotypic hippocampal slice cultures (Huchzermeyer et al. 2008). Thus, many of the results obtained in slices, in particular regarding metabolic regulation of vascular diameters, fall into the category of pathophysiology. The metabolic pathways elucidated by these studies are likely to be critical under conditions of stroke and hypoxia (Gordon et al. 2008).

Indeed, in addition to these basic studies providing a firmer foundation for current functional neuroimaging methods, a clear goal is to identify how the coupling of neuronal activity, blood flow, and energy metabolism is altered in disease. Again a multi-modal imaging approach is likely to be essential, because all the normal mechanisms are called into question. With stroke, and a reduction of neurons and proliferation of glial cells, how is the CBF response changed? In neurodegenerative

disease, are there early signs of dysfunction in the way CBF or $CMRO_2$ are coupled to neuronal activity? In general, under what circumstances do compromised CBF and $CMRO_2$ responses begin to limit neuronal function? What mechanisms could lead to changes in the dynamics of the BOLD response, due either to disease or to healthy aging?

In future, developments in imaging technology and targeted genetic labeling will allow directly control of firing patterns in identified single cells and cellular populations, while measuring the resultant vascular, metabolic and neuronal response across spatial scales. These future experiments will provide important insights into pathways of neurovascular communication and will identify vasoactive messengers, release of which drives stimulus-evoked hemodynamic signals. The wide range of measurements will need to be integrated within a comprehensive theoretical framework that quantitatively models the steps from activity of specific neuronal cell types to vascular and metabolic changes to BOLD fMRI signals. Ultimately, identification of macro- and microscopic hemodynamic "signatures" of activation in populations of neurons with known phenotype and neurotransmitter content will greatly extend the utility of fMRI as a quantitative probe of physiology for both basic and clinical neuroscience applications.

For translation to human imaging, computational methods are required for neuronal population activity from combined EEG/MEG and fMRI data. The proper interpretation of such multimodal noninvasive imaging measures critically depends on accurate forward models, linking each of the imaging observables to the underlying physiological parameters, along with physiological models, linking the different physiological parameters themselves. Given such models, it should in principle be possible to obtain quantitative spatiotemporal estimates of the relevant physiological parameters, using a Bayesian estimation framework, as outlined above. It should be noted, however, that the accuracy of the resulting estimates will be limited by the accuracy of the models used. Further work is therefore needed to extend and validate the models, under a broad range of normal- and pathophysiological conditions.

Acknowledgements The authors would like you to acknowledge Klas M. Pettersen, Henrik Linden, Ivan C. Teng and Peifang Tian for help with making some of the figures, and the financial support from the following NIH grants: R01NS051188, R01NS057198, R21EB009118 (to Anna Devor), R01EB000790 (to Anders M. Dale), R01NS057476 (to David A. Boas) and R01 NS036722 (to Richard R. Buxton) and Research Council of Norway (eVITA, FRIBIOMOL to Gaute T. Einevoll).

References

Aguirre AD, Chen Y, Fujimoto JG, Ruvinskaya L, Devor A, Boas DA (2006) Depth-resolved imaging of functional activation in the rat cerebral cortex using optical coherence tomography. Opt Lett 31:3459–3461

Agulhon C, Petravicz J, McMullen AB, Sweger EJ, Minton SK, Taves SR, Casper KB, Fiacco TA, McCarthy KD (2008) What is the role of astrocyte calcium in neurophysiology? Neuron 59:932–946

Akkin T, Dave DP, Milner TE, Rylander HG (2004) Detection of neural activity using phase-sensitive optical low-coherence reflectometry. Opt Express 12:2377–2386
Alonso BD, Lowe AS, Dear JP, Lee KC, Williams SC, Finnerty GT (2008) Sensory inputs from whisking movements modify cortical whisker maps visualized with functional magnetic resonance imaging. Cereb Cortex 18(6):1314–1325
Arai T, Nakao S, Mori K, Ishimori K, Morishima I, Miyazawa T, Fritz-Zieroth B (1990) Cerebral oxygen utilization analyzed by the use of oxygen-17 and its nuclear magnetic resonance. Biochem Biophys Res Commun 169:153–158
Arai T, Mori K, Nakao S, Watanabe K, Kito K, Aoki M, Mori H, Morikawa S, Inubushi T (1991) In vivo oxygen-17 nuclear magnetic resonance for the estimation of cerebral blood flow and oxygen consumption. Biochem Biophys Res Commun 179:954–961
Ayata C, Shin HK, Salomone S, Ozdemir-Gursoy Y, Boas DA, Dunn AK, Moskowitz MA (2004) Pronounced hypoperfusion during spreading depression in mouse cortex. J Cereb Blood Flow Metab 24:1172–1182
Baker BJ, Kosmidis EK, Vucinic D, Falk CX, Cohen LB, Djurisic M, Zecevic D (2005) Imaging brain activity with voltage- and calcium-sensitive dyes. Cell Mol Neurobiol 25:245–282
Barth DS, Di S (1991) Laminar excitability cycles in neocortex. J Neurophysiol 65:891–898
Barth DS, Di S, Baumgartner C (1989) Laminar cortical interactions during epileptic spikes studied with principal component analysis and physiological modeling. Brain Res 484: 13–35
Barth DS, Baumgartner C, Di S (1990) Laminar interactions in rat motor cortex during cyclical excitability changes of the penicillin focus. Brain Res 508:105–117
Beierlein M, Gibson JR, Connors BW (2000) A network of electrically coupled interneurons drives synchronized inhibition in neocortex. Nat Neurosci 3:904–910
Beierlein M, Gibson JR, Connors BW (2003) Two dynamically distinct inhibitory networks in layer 4 of the neocortex. J Neurophysiol 90:2987–3000
Bizheva K, Unterhuber A, Hermann B, Povazay B, Sattmann H, Drexler W, Stingl A, Le T, Mei M, Holzwarth R, Reitsamer HA, Morgan JE, Cowey A (2004) Imaging ex vivo and in vitro brain morphology in animal models with ultrahigh resolution optical coherence tomography. J Biomed Opt 9:719–724
Blanco VM, Stern JE, Filosa JA (2008) Tone-dependent vascular responses to astrocyte-derived signals. Am J Physiol Heart Circ Physiol 294:H2855–H2863
Blomquist P, Devor A, Indahl UG, Ulbert I, Einevoll GT, Dale AM (2009) Estimation of thalamocortical and intracortical network models from joint thalamic single-electrode and cortical laminar-electrode recordings in the rat barrel system. PLoS Comput Biol 5:e1000328
Boas DA, Jones SR, Devor A, Huppert TJ, Dale AM (2008) A vascular anatomical network model of the spatio-temporal response to brain activation. Neuroimage 40:1116–1129
Bolay H, Reuter U, Dunn AK, Huang Z, Boas DA, Moskowitz MA (2002) Intrinsic brain activity triggers trigeminal meningeal afferents in a migraine model. Nat Med 8:136–142
Bower JM, Beeman D (1998) The Book of GENESIS: Exploring Realistic Neural Models with the GEneral NEural SImulation System, 2nd edn. Springer, New York
Boxerman JL, Hamberg LM, Rosen BR, Weisskoff RM (1995) MR contrast due to intravascular magnetic susceptibility perturbations. Magn Reson Med 34:555–566
Bressler D, Spotswood N, Whitney D (2007) Negative BOLD fMRI response in the visual cortex carries precise stimulus-specific information. PLoS One 2:e410
Briers JD (2001) Laser Doppler, speckle and related techniques for blood perfusion mapping and imaging. Physiol Meas 22:R35–R66
Brown GG, Perthen JE, Liu TT, Buxton RB (2007) A primer on functional magnetic resonance imaging. Neuropsychol Rev 17:107–125
Buxton RB (2005) Quantifying CBF with arterial spin labeling. J Magn Reson Imaging 22:723–726
Buxton RB, Wong EC, Frank LR (1998) Dynamics of blood flow and oxygenation changes during brain activation: the balloon model. Magn Reson Med 39:855–864
Buxton RB, Uludag K, Dubowitz DJ, Liu TT (2004) Modeling the hemodynamic response to brain activation. Neuroimage 23(Suppl 1):S220–S233

Buzsaki G (2004) Large-scale recording of neuronal ensembles. Nat Neurosci 7:446–451
Caesar K, Offenhauser N, Lauritzen M (2008) Gamma-aminobutyric acid modulates local brain oxygen consumption and blood flow in rat cerebellar cortex. J Cereb Blood Flow Metab 28:906–915
Carnevale NT, Hines ML (2006) The NEURON book. Cambridge University Press, Cambridge
Cauli B, Tong XK, Rancillac A, Serluca N, Lambolez B, Rossier J, Hamel E (2004) Cortical GABA interneurons in neurovascular coupling: relays for subcortical vasoactive pathways. J Neurosci 24:8940–8949
Chaigneau E, Oheim M, Audinat E, Charpak S (2003) Two-photon imaging of capillary blood flow in olfactory bulb glomeruli. Proc Natl Acad Sci USA 100:13081–13086
Chaigneau E, Tiret P, Lecoq J, Ducros M, Knopfel T, Charpak S (2007) The relationship between blood flow and neuronal activity in the rodent olfactory bulb. J Neurosci 27:6452–6460
Chance B, Cohen P, Jobsis F, Schoener B (1962) Intracellular oxidation-reduction states in vivo. Science 137:499–508
Chen Y, Aguirre AD, Ruvinskaya L, Devor A, Boas DA, Fujimoto JG (2008) Optical coherence tomography (OCT) reveals depth-resolved dynamics during functional brain activation. J Neurosci Methods 178(1):162–173
Cohen LB, Lesher S (1986) Optical monitoring of membrane potential: methods of multisite optical measurement. Soc Gen Physiol Ser 40:71–99
Cox SB, Woolsey TA, Rovainen CM (1993) Localized dynamic changes in cortical blood flow with whisker stimulation corresponds to matched vascular and neuronal architecture of rat barrels. J Cereb Blood Flow Metab 13:899–913
D'Esposito M, Deouell LY, Gazzaley A (2003) Alterations in the BOLD fMRI signal with ageing and disease: a challenge for neuroimaging. Nat Rev Neurosci 4:863–872
Dale AM, Buckner RL (1997) Selective averaging of rapidly presented individual trails using fMRI. Hum Brain Mapp 5:329–340
Dale AM, Halgren E (2001) Spatiotemporal mapping of brain activity by integration of multiple imaging modalities. Curr Opin Neurobiol 11:202–208
Dale AM, Liu AK, Fischl BR, Buckner RL, Belliveau JW, Lewine JD, Halgren E (2000) Dynamic statistical parametric mapping: combining fMRI and MEG for high-resolution imaging of cortical activity. Neuron 26:55–67
Davis TL, Kwong KK, Weisskoff RM, Rosen BR (1998) Calibrated functional MRI: mapping the dynamics of oxidative metabolism. Proc Natl Acad Sci USA 95:1834–1839
Deans MR, Gibson JR, Sellitto C, Connors BW, Paul DL (2001) Synchronous activity of inhibitory networks in neocortex requires electrical synapses containing connexin36. Neuron 31:477–485
Derdikman D, Hildesheim R, Ahissar E, Arieli A, Grinvald A (2003) Imaging spatiotemporal dynamics of surround inhibition in the barrels somatosensory cortex. J Neurosci 23:3100–3105
Devor A, Dunn AK, Andermann ML, Ulbert I, Boas DA, Dale AM (2003) Coupling of total hemoglobin concentration, oxygenation, and neural activity in rat somatosensory cortex. Neuron 39:353–359
Devor A, Sakadzic S, Yucel MA, Teng IC, Kasischke KA, Boas DA (2009) In vivo functional NADH imaging with single-cell resolution. In: Society for Neurosciences. Meeting Planner. Chicago, IL: Society for Neuroscience, 2009. Online
Devor A, Shih AY, Tsai PS, Blinder P, Tian P, Teng IC, Kleinfeld D (2008a) Two-photon laser scanning microscopy as a tool to study cortical vasodynamics under normal and ischemic conditions In: Roe AW (ed) Imaging the brain with optical methods. Springer http://www.springer.com/biomed/neuroscience/book/978-1-4419-0451-5
Devor A, Ulbert I, Dunn AK, Narayanan SN, Jones SR, Andermann ML, Boas DA, Dale AM (2005) Coupling of the cortical hemodynamic response to cortical and thalamic neuronal activity. Proc Natl Acad Sci USA 102:3822–3827
Devor A, Tian P, Nishimura N, Teng IC, Hillman EM, Narayanan SN, Ulbert I, Boas DA, Kleinfeld D, Dale AM (2007) Suppressed neuronal activity and concurrent arteriolar vasoconstriction may explain negative blood oxygenation level-dependent signal. J Neurosci 27:4452–4459

Devor A, Hillman EM, Tian P, Waeber C, Teng IC, Ruvinskaya L, Shalinsky MH, Zhu H, Haslinger RH, Narayanan SN, Ulbert I, Dunn AK, Lo EH, Rosen BR, Dale AM, Kleinfeld D, Boas DA (2008b) Stimulus-induced changes in blood flow and 2-deoxyglucose uptake dissociate in ipsilateral somatosensory cortex. J Neurosci 28:14347–14357

Di S, Baumgartner C, Barth DS (1990) Laminar analysis of extracellular field potentials in rat vibrissa/barrel cortex. J Neurophysiol 63:832–840

Draijer M, Hondebrink E, van Leeuwen T, Steenbergen W (2008) Review of laser speckle contrast techniques for visualizing tissue perfusion. Lasers Med Sci 24(4): 639–651

Drexler W, Morgner U, Kartner FX, Pitris C, Boppart SA, Li XD, Ippen EP, Fujimoto JG (1999) In vivo ultrahigh-resolution optical coherence tomography. Opt Lett 24:1221–1223

Dunn AK, Bolay H, Moskowitz MA, Boas DA (2001) Dynamic imaging of cerebral blood flow using laser speckle. J Cereb Blood Flow Metab 21:195–201

Dunn AK, Devor A, Dale AM, Boas DA (2005) Spatial extent of oxygen metabolism and hemodynamic changes during functional activation of the rat somatosensory cortex. Neuroimage 27:279–290

Dunn AK, Devor A, Bolay H, Andermann ML, Moskowitz MA, Dale AM, Boas DA (2003) Simultaneous imaging of total cerebral hemoglobin concentration, oxygenation, and blood flow during functional activation. Opt Lett 28:28–30

Dunphy I, Vinogradov SA, Wilson DF (2002) Oxyphor R2 and G2: phosphors for measuring oxygen by oxygen-dependent quenching of phosphorescence. Anal Biochem 310:191–198

Ebner TJ, Chen G (1995) Use of voltage-sensitive dyes and optical recordings in the central nervous system. Prog Neurobiol 46:463–506

Einevoll GT, Pettersen KH, Devor A, Ulbert I, Halgren E, Dale AM (2007) Laminar population analysis: estimating firing rates and evoked synaptic activity from multielectrode recordings in rat barrel cortex. J Neurophysiol 97:2174–2190

Fang-Yen C, Chu MC, Seung HS, Dasari RR, Feld MS (2004) Noncontact measurement of nerve displacement during action potential with a dual-beam low-coherence interferometer. Opt Lett 29:2028–2030

Fang Q, Sakadzic S, Ruvinskaya L, Devor A, Dale AM, Boas DA (2008) Oxygen advection and diffusion in a three- dimensional vascular anatomical network. Opt Express 16:17530–17541

Faraci FM, Breese KR (1993) Nitric oxide mediates vasodilatation in response to activation of N-methyl-D-aspartate receptors in brain. Circ Res 72:476–480

Faraci FM, Heistad DD (1998) Regulation of the cerebral circulation: role of endothelium and potassium channels. Physiol Rev 78:53–97

Ferezou I, Bolea S, Petersen CC (2006) Visualizing the cortical representation of whisker touch: voltage-sensitive dye imaging in freely moving mice. Neuron 50:617–629

Fergus A, Lee KS (1997) GABAergic regulation of cerebral microvascular tone in the rat. J Cereb Blood Flow Metab 17:992–1003

Fiat D, Kang S (1992) Determination of the rate of cerebral oxygen consumption and regional cerebral blood flow by non-invasive 17O in vivo NMR spectroscopy and magnetic resonance imaging: Part 1. Theory and data analysis methods. Neurol Res 14:303–311

Fiat D, Kang S (1993) Determination of the rate of cerebral oxygen consumption and regional cerebral blood flow by non-invasive 17O in vivo NMR spectroscopy and magnetic resonance imaging. Part 2. Determination of CMRO2 for the rat by 17O NMR, and CMRO2, rCBF and the partition coefficient for the cat by 17O MRI. Neurol Res 15:7–22

Filosa JA, Bonev AD, Straub SV, Meredith AL, Wilkerson MK, Aldrich RW, Nelson MT (2006) Local potassium signaling couples neuronal activity to vasodilation in the brain. Nat Neurosci 9(11):1397–1403

Finikova OS, Lebedev AY, Aprelev A, Troxler T, Gao F, Garnacho C, Muro S, Hochstrasser RM, Vinogradov SA (2008) Oxygen microscopy by two-photon-excited phosphorescence. Chemphyschem 9:1673–1679

Fox PT, Raichle ME (1986) Focal physiological uncoupling of cerebral blood flow and oxidative metabolism during somatosensory stimulation in human subjects. Proc Natl Acad Sci USA 83:1140–1144

Fox PT, Raichle ME, Mintun MA, Dence C (1988) Nonoxidative glucose consumption during focal physiologic neural activity. Science 241:462–464

Freeman JA, Nicholson C (1975) Experimental optimization of current source-density technique for anuran cerebellum. J Neurophysiol 38(2):369–82.

Friston KJ (2005) Models of brain function in neuroimaging. Annu Rev Psychol 56:57–87

Frostig RD, Lieke EE, Ts'o DY, Grinvald A (1990) Cortical functional architecture and local coupling between neuronal activity and the microcirculation revealed by in vivo high-resolution optical imaging of intrinsic signals. Proc Natl Acad Sci USA 87:6082–6086

Gobel W, Kampa BM, Helmchen F (2007) Imaging cellular network dynamics in three dimensions using fast 3D laser scanning. Nat Methods 4:73–79

Gordon GR, Choi HB, Rungta RL, Ellis-Davies GC, Macvicar BA (2008) Brain metabolism dictates the polarity of astrocyte control over arterioles. Nature 456(7223):745–749

Grinvald A (1992) Optical imaging of architecture and function in the living brain sheds new light on cortical mechanisms underlying visual perception. Brain Topogr 5:71–75

Grinvald A, Hildesheim R (2004) VSDI: a new era in functional imaging of cortical dynamics. Nat Rev Neurosci 5:874–885

Grinvald A, Frostig RD, Lieke E, Hildesheim R (1988) Optical imaging of neuronal activity. Physiol Rev 68:1285–1366

Grinvald A, Lieke E, Frostig RD, Gilbert CD, Wiesel TN (1986) Functional architecture of cortex revealed by optical imaging of intrinsic signals. Nature 324:361–364

Grubb RL Jr, Raichle ME, Eichling JO, Ter-Pogossian MM (1974) The effects of changes in PaCO2 on cerebral blood volume, blood flow, and vascular mean transit time. Stroke 5:630–639

Guadagno JV, Calautti C, Baron JC (2003) Progress in imaging stroke: emerging clinical applications. Br Med Bull 65:145–157

Hämäläinen M, Hari R, Ilmoniemi R, Knuutila J, Lounasmaa O (1993) Magnetoencephalography theory, instrumentation, and applications to noninvasive studies of the working human brain. Rev Mod Phys 65:413–497

Hamel E (2004) Cholinergic modulation of the cortical microvascular bed. Prog Brain Res 145:171–178

Hamel E (2006) Perivascular nerves and the regulation of cerebrovascular tone. J Appl Physiol 100:1059–1064

Hillman EM, Boas DA, Dale AM, Dunn AK (2004) Laminar optical tomography: demonstration of millimeter-scale depth-resolved imaging in turbid media. Opt Lett 29:1650–1652

Hillman EM, Devor A, Bouchard MB, Dunn AK, Krauss GW, Skoch J, Bacskai BJ, Dale AM, Boas DA (2007) Depth-resolved optical imaging and microscopy of vascular compartment dynamics during somatosensory stimulation. Neuroimage 35:89–104

Hodics T, Cohen LG (2005) Functional neuroimaging in motor recovery after stroke. Top Stroke Rehabil 12:15–21

Hu Y, Wilson GS (1997) A temporary local energy pool coupled to neuronal activity: fluctuations of extracellular lactate levels in rat brain monitored with rapid-response enzyme-based sensor. J Neurochem 69:1484–1490

Huang D, Swanson EA, Lin CP, Schuman JS, Stinson WG, Chang W, Hee MR, Flotte T, Gregory K, Puliafito CA et al (1991) Optical coherence tomography. Science 254:1178–1181

Huber R, Adler DC, Srinivasan VJ, Fujimoto JG (2007) Fourier domain mode locking at 1050 nm for ultra-high-speed optical coherence tomography of the human retina at 236,000 axial scans per second. Opt Lett 32:2049–2051

Huchzermeyer C, Albus K, Gabriel HJ, Otahal J, Taubenberger N, Heinemann U, Kovacs R, Kann O (2008) Gamma oscillations and spontaneous network activity in the hippocampus are highly sensitive to decreases in pO2 and concomitant changes in mitochondrial redox state. J Neurosci 28:1153–1162

Huppert TJ, Allen MS, Diamond SG, Boas DA (2009) Estimating cerebral oxygen metabolism from fMRI with a dynamic multicompartment Windkessel model. Hum Brain Mapp 30: 1548–1567

Huppert TJ, Allen MS, Benav H, Jones PB, Boas DA (2007) A multicompartment vascular model for inferring baseline and functional changes in cerebral oxygen metabolism and arterial dilation. J Cereb Blood Flow Metab 27:1262–1279

Iadecola C (2004) Neurovascular regulation in the normal brain and in Alzheimer's disease. Nat Rev Neurosci 5:347–360

Iadecola C, Niwa K (2002) Nitric oxide. In: Edvinsson L, Krause DN (eds) Cerebral blood flow and metabolism, 2nd edn. Lippincott Williams & Wilkins, Philadelphia, pp 295–310

Iadecola C, Nedergaard M (2007) Glial regulation of the cerebral microvasculature. Nat Neurosci 10:1369–1376

Ido Y, Chang K, Williamson JR (2004) NADH augments blood flow in physiologically activated retina and visual cortex. Proc Natl Acad Sci USA 101:653–658

Iliff JJ, D'Ambrosio R, Ngai AC, Winn HR (2003) Adenosine receptors mediate glutamate-evoked arteriolar dilation in the rat cerebral cortex. Am J Physiol Heart Circ Physiol 284:H1631–H1637

Ito H, Ibaraki M, Kanno I, Fukuda H, Miura S (2005) Changes in the arterial fraction of human cerebral blood volume during hypercapnia and hypocapnia measured by positron emission tomography. J Cereb Blood Flow Metab 25:852–857

Jackson J (1998) Classical electrodynamics. Wiley, Hoboken, NJ

Jones M, Berwick J, Mayhew J (2002) Changes in blood flow, oxygenation, and volume following extended stimulation of rodent barrel cortex. Neuroimage 15:474–487

Jones M, Berwick J, Johnston D, Mayhew J (2001) Concurrent optical imaging spectroscopy and laser-Doppler flowmetry: the relationship between blood flow, oxygenation, and volume in rodent barrel cortex. Neuroimage 13:1002–1015

Jones M, Hewson-Stoate N, Martindale J, Redgrave P, Mayhew J (2004) Nonlinear coupling of neural activity and CBF in rodent barrel cortex. Neuroimage 22:956–965

Kasischke KA, Vishwasrao HD, Fisher PJ, Zipfel WR, Webb WW (2004) Neural activity triggers neuronal oxidative metabolism followed by astrocytic glycolysis. Science 305:99–103

Kasischke KA, Lambert EM, Panepento B, Sun A, Gelbard HA, Burgess RW, Foster TH, Nedergaard M (2011) Two-photon NADH imaging exposes boundaries of oxygen diffusion in cortical vascular supply regions. J Cereb Blood Flow Metab 31(1):68–81

Kim T, Hendrich KS, Masamoto K, Kim SG (2007) Arterial versus total blood volume changes during neural activity-induced cerebral blood flow change: implication for BOLD fMRI. J Cereb Blood Flow Metab 27:1235–1247

Kleinfeld D, Griesbeck O (2005) From art to engineering? The rise of in vivo mammalian electrophysiology via genetically targeted labeling and nonlinear imaging. PLoS Biol 3:e355

Kleinfeld D, Mitra PP, Helmchen F, Denk W (1998) Fluctuations and stimulus-induced changes in blood flow observed in individual capillaries in layers 2 through 4 of rat neocortex. Proc Natl Acad Sci USA 95:15741–15746

Kocharyan A, Fernandes P, Tong XK, Vaucher E, Hamel E (2008) Specific subtypes of cortical GABA interneurons contribute to the neurovascular coupling response to basal forebrain stimulation. J Cereb Blood Flow Metab 28:221–231

Koehler RC, Roman RJ, Harder DR (2009) Astrocytes and the regulation of cerebral blood flow. Trends Neurosci 32:160–169

Kohl M, Lindauer U, Royl G, Kuhl M, Gold L, Villringer A, Dirnagl U (2000) Physical model for the spectroscopic analysis of cortical intrinsic optical signals. Phys Med Biol 45:3749–3764

Koralek KA, Olavarria J, Killackey HP (1990) Areal and laminar organization of corticocortical projections in the rat somatosensory cortex. J Comp Neurol 299:133–150

Kudomi N, Watabe H, Hayashi T, Iida H (2007) Separation of input function for rapid measurement of quantitative CMRO2 and CBF in a single PET scan with a dual tracer administration method. Phys Med Biol 52:1893–1908

Kudomi N, Hayashi T, Watabe H, Teramoto N, Piao R, Ose T, Koshino K, Ohta Y, Iida H (2009) A physiologic model for recirculation water correction in CMRO2 assessment with 15O2 inhalation PET. J Cereb Blood Flow Metab 29:355–364

Lauritzen M (2005) Opinion: Reading vascular changes in brain imaging: is dendritic calcium the key? Nat Rev Neurosci 6:77–85

Lazebnik M, Marks DL, Potgieter K, Gillette R, Boppart SA (2003) Functional optical coherence tomography for detecting neural activity through scattering changes. Opt Lett 28: 1218–1220

Lee SP, Duong TQ, Yang G, Iadecola C, Kim SG (2001) Relative changes of cerebral arterial and venous blood volumes during increased cerebral blood flow: implications for BOLD fMRI. Magn Reson Med 45:791–800

Lefort S, Tomm C, Floyd Sarria JC, Petersen CC (2009) The excitatory neuronal network of the C2 barrel column in mouse primary somatosensory cortex. Neuron 61:301–316

Leitgeb RA, Schmetterer L, Drexler W, Fercher AF, Zawadzki RJ, Bajraszewski T (2003) Real-time assessment of retinal blood flow with ultrafast acquisition by color Doppler Fourier domain optical coherence tomography. Opt Express 11:3116–3121

Leontiev O, Buxton RB (2007) Reproducibility of BOLD, perfusion, and CMRO2 measurements with calibrated-BOLD fMRI. Neuroimage 35:175–184

Leontiev O, Dubowitz DJ, Buxton RB (2007) CBF/CMRO2 coupling measured with calibrated BOLD fMRI: sources of bias. Neuroimage 36:1110–1122

Leski S, Wojcik DK, Tereszczuk J, Swiejkowski DA, Kublik E, Wrobel A (2007) Inverse current-source density method in 3D: reconstruction fidelity, boundary effects, and influence of distant sources. Neuroinformatics 5:207–222

Lindauer U, Leithner C, Kaasch H, Rohrer B, Foddis M, Fuchtemeier M, Offenhauser N, Steinbrink J, Royl G, Kohl-Bareis M, Dirnagl U (2010) Neurovascular coupling in rat brain operates independent of hemoglobin deoxygenation. J Cereb Blood Flow Metab 30(4):757–768

Liu X, Li C, Falck JR, Roman RJ, Harder DR, Koehler RC (2008) Interaction of nitric oxide, 20-HETE, and EETs during functional hyperemia in whisker barrel cortex. Am J Physiol Heart Circ Physiol 295:H619–H631

Logothetis NK (2002) The neural basis of the blood-oxygen-level-dependent functional magnetic resonance imaging signal. Philos Trans R Soc Lond B Biol Sci 357:1003–1037

Logothetis NK, Kayser C, Oeltermann A (2007) In vivo measurement of cortical impedance spectrum in monkeys: implications for signal propagation. Neuron 55:809–823

Lu H, Ge Y (2008) Quantitative evaluation of oxygenation in venous vessels using T2-Relaxation-Under-Spin-Tagging MRI. Magn Reson Med 60:357–363

Lu H, Zhao C, Ge Y, Lewis-Amezcua K (2008) Baseline blood oxygenation modulates response amplitude: physiologic basis for intersubject variations in functional MRI signals. Magn Reson Med 60:364–372

Magistretti PJ, Pellerin L, Rothman DL, Shulman RG (1999) Energy on demand. Science 283:496–497

Maheswari RU, Takaoka H, Kadono H, Homma R, Tanifuji M (2003) Novel functional imaging technique from brain surface with optical coherence tomography enabling visualization of depth resolved functional structure in vivo. J Neurosci Methods 124:83–92

Mainen ZF, Sejnowski TJ (1996) Influence of dendritic structure on firing pattern in model neocortical neurons. Nature 382:363–366

Malonek D, Grinvald A (1996) Interactions between electrical activity and cortical microcirculation revealed by imaging spectroscopy: implications for functional brain mapping. Science 272:551–554

Mandeville JB, Marota JJ, Ayata C, Zaharchuk G, Moskowitz MA, Rosen BR, Weisskoff RM (1999) Evidence of a cerebrovascular postarteriole windkessel with delayed compliance. J Cereb Blood Flow Metab 19:679–689

Mann-Metzer P, Yarom Y (2000) Electrotonic coupling synchronizes interneuron activity in the cerebellar cortex. Prog Brain Res 124:115–122

Margrie TW, Meyer AH, Caputi A, Monyer H, Hasan MT, Schaefer AT, Denk W, Brecht M (2003) Targeted whole-cell recordings in the mammalian brain in vivo. Neuron 39:911–918

Mayhew J, Johnston D, Berwick J, Jones M, Coffey P, Zheng Y (2000) Spectroscopic analysis of neural activity in brain: increased oxygen consumption following activation of barrel cortex. Neuroimage 12:664–675

Metea MR, Newman EA (2006) Glial cells dilate and constrict blood vessels: a mechanism of neurovascular coupling. J Neurosci 26:2862–2870

Mik EG, van Leeuwen TG, Raat NJ, Ince C (2004) Quantitative determination of localized tissue oxygen concentration in vivo by two-photon excitation phosphorescence lifetime measurements. J Appl Physiol 97:1962–1969

Miller RJ (1988) Calcium signalling in neurons. Trends Neurosci 11:415–419

Mintun MA, Raichle ME, Martin WR, Herscovitch P (1984) Brain oxygen utilization measured with O-15 radiotracers and positron emission tomography. J Nucl Med 25:177–187

Mintun MA, Vlassenko AG, Rundle MM, Raichle ME (2004) Increased lactate/pyruvate ratio augments blood flow in physiologically activated human brain. Proc Natl Acad Sci USA 101:659–664

Mitzdorf U (1985) Current source-density method and application in cat cerebral cortex: investigation of evoked potentials and EEG phenomena. Physiol Rev 65:37–100

Moore CI, Nelson SB (1998) Spatio-temporal subthreshold receptive fields in the vibrissa representation of rat primary somatosensory cortex. J Neurophysiol 80:2882–2892

Mulligan SJ, MacVicar BA (2004) Calcium transients in astrocyte endfeet cause cerebrovascular constrictions. Nature 431:195–199

Narayan SM, Santori EM, Blood AJ, Burton JS, Toga AW (1994) Imaging optical reflectance in rodent barrel and forelimb sensory cortex. Neuroimage 1:181–190

Narayan SM, Esfahani P, Blood AJ, Sikkens L, Toga AW (1995) Functional increases in cerebral blood volume over somatosensory cortex. J Cereb Blood Flow Metab 15:754–765

Nemoto M, Sheth S, Guiou M, Pouratian N, Chen JW, Toga AW (2004) Functional signal- and paradigm-dependent linear relationships between synaptic activity and hemodynamic responses in rat somatosensory cortex. J Neurosci 24:3850–3861

Nemoto M, Nomura Y, Sato C, Tamura M, Houkin K, Koyanagi I, Abe H (1999) Analysis of optical signals evoked by peripheral nerve stimulation in rat somatosensory cortex: dynamic changes in hemoglobin concentration and oxygenation. J Cereb Blood Flow Metab 19: 246–259

Nicholson C, Freeman JA (1975) Theory of current source-density analysis and determination of conductivity tensor for anuran cerebellum. J Neurophysiol 38:356–368

Nilsson M, Eriksson PS, Ronnback L, Hansson E (1993) GABA induces Ca2+ transients in astrocytes. Neuroscience 54:605–614

Nishimura N, Schaffer CB, Friedman B, Lyden PD, Kleinfeld D (2007) Penetrating arterioles are a bottleneck in the perfusion of neocortex. Proc Natl Acad Sci USA 104:365–370

Nishimura N, Schaffer CB, Friedman B, Tsai PS, Lyden PD, Kleinfeld D (2006) Targeted insult to subsurface cortical blood vessels using ultrashort laser pulses: three models of stroke. Nat Methods 3:99–108

Nunez PL, Srinivasan R (2006) Electric fields of the brain: the neurophysics of EEG. Oxford University Press, New York

Obata T, Liu TT, Miller KL, Luh WM, Wong EC, Frank LR, Buxton RB (2004) Discrepancies between BOLD and flow dynamics in primary and supplementary motor areas: application of the balloon model to the interpretation of BOLD transients. Neuroimage 21:144–153

Ogawa S, Menon RS, Tank DW, Kim SG, Merkle H, Ellermann JM, Ugurbil K (1993) Functional brain mapping by blood oxygenation level-dependent contrast magnetic resonance imaging. A comparison of signal characteristics with a biophysical model. Biophys J 64:803–812

Ohata H, Cao S, Koehler RC (2006) Contribution of adenosine A2A and A2B receptors and heme oxygenase to AMPA-induced dilation of pial arterioles in rats. Am J Physiol Regul Integr Comp Physiol 291:R728–R735

Ou W, Nissila I, Radhakrishnan H, Boas DA, Hamalainen MS, Franceschini MA (2009) Study of neurovascular coupling in humans via simultaneous magnetoencephalography and diffuse optical imaging acquisition. Neuroimage 46:624–632

Peppiatt CM, Howarth C, Mobbs P, Attwell D (2006) Bidirectional control of CNS capillary diameter by pericytes. Nature 443:700–704

Pettersen KH, Einevoll GT (2008) Amplitude variability and extracellular low-pass filtering of neuronal spikes. Biophys J. 94(3):784–802.
Pettersen KH, Hagen E, Einevoll GT (2008) Estimation of population firing rates and current source densities from laminar electrode recordings. J Comput Neurosci 24:291–313
Pettersen KH, Linden H, Dale AM, Einevoll GT (2012) Extracellular spikes and CSD. In: Brette R, Destexhe A (eds) Handbook of neural activity measurement Cambridge University Press
Pettersen KH, Devor A, Ulbert I, Dale AM, Einevoll GT (2006) Current-source density estimation based on inversion of electrostatic forward solution: effects of finite extent of neuronal activity and conductivity discontinuities. J Neurosci Methods 154:116–133
Petzold GC, Albeanu DF, Sato TF, Murthy VN (2008) Coupling of neural activity to blood flow in olfactory glomeruli is mediated by astrocytic pathways. Neuron 58:897–910
Phelps ME, Kuhl DE, Mazziota JC (1981) Metabolic mapping of the brain's response to visual stimulation: studies in humans. Science 211:1445–1448
Pinto DJ, Brumberg JC, Simons DJ (2000) Circuit dynamics and coding strategies in rodent somatosensory cortex. J Neurophysiol 83:1158–1166
Polimeni JR, Granquist-Fraser D, Wood RJ, Schwartz EL (2005) Physical limits to spatial resolution of optical recording: clarifying the spatial structure of cortical hypercolumns. Proc Natl Acad Sci USA 102:4158–4163
Porter JT, McCarthy KD (1996) Hippocampal astrocytes in situ respond to glutamate released from synaptic terminals. J Neurosci 16:5073–5081
Raichle ME, Mintun MA (2006) Brain work and brain imaging. Annu Rev Neurosci 29:449–476
Rancillac A, Rossier J, Guille M, Tong XK, Geoffroy H, Amatore C, Arbault S, Hamel E, Cauli B (2006) Glutamatergic control of microvascular tone by distinct GABA neurons in the cerebellum. J Neurosci 26:6997–7006
Rappelsberger P, Pockberger H, Petsche H (1981) Current source density analysis: methods and application to simultaneously recorded field potentials of the rabbit's visual cortex. Pflugers Arch 389:159–170
Ross WN (1989) Changes in intracellular calcium during neuron activity. Annu Rev Physiol 51:491–506
Rouach N, Koulakoff A, Abudara V, Willecke K, Giaume C (2008) Astroglial metabolic networks sustain hippocampal synaptic transmission. Science 322:1551–1555
Royl G, Fuchtemeier M, Leithner C, Megow D, Offenhauser N, Steinbrink J, Kohl-Bareis M, Dirnagl U, Lindauer U (2008) Hypothermia effects on neurovascular coupling and cerebral metabolic rate of oxygen. Neuroimage 40:1523–1532
Rubio R, Berne RM, Bockman EL, Curnish RR (1975) Relationship between adenosine concentration and oxygen supply in rat brain. Am J Physiol 228:1896–1902
Sakadzic S, Yuan S, Dilekoz E, Ruvinskaya S, Vinogradov SA, Ayata C, Boas DA (2009) Simultaneous imaging of cerebral partial pressure of oxygen and blood flow during functional activation and cortical spreading depression. Appl Opt 48:D169–D177
Schaffer CB, Friedman B, Nishimura N, Schroeder LF, Tsai PS, Ebner FF, Lyden PD, Kleinfeld D (2006) Two-photon imaging of cortical surface microvessels reveals a robust redistribution in blood flow after vascular occlusion. PLoS Biol 4:e22
Schmidt DM, George JS, Wood CC (1999) Bayesian inference applied to the electromagnetic inverse problem. Hum Brain Mapp 7:195–212
Schroeder CE, Lindsley RW, Specht C, Marcovici A, Smiley JF, Javitt DC (2001) Somatosensory input to auditory association cortex in the macaque monkey. J Neurophysiol 85:1322–1327
Schummers J, Yu H, Sur M (2008) Tuned responses of astrocytes and their influence on hemodynamic signals in the visual cortex. Science 320:1638–1643
Sheth SA, Nemoto M, Guiou M, Walker M, Pouratian N, Toga AW (2004) Linear and nonlinear relationships between neuronal activity, oxygen metabolism, and hemodynamic responses. Neuron 42:347–355
Shi Y, Liu X, Gebremedhin D, Falck JR, Harder DR, Koehler RC (2008) Interaction of mechanisms involving epoxyeicosatrienoic acids, adenosine receptors, and metabotropic glutamate

receptors in neurovascular coupling in rat whisker barrel cortex. J Cereb Blood Flow Metab 28:111–125
Shmuel A, Augath M, Oeltermann A, Logothetis NK (2006) Negative functional MRI response correlates with decreases in neuronal activity in monkey visual area V1. Nat Neurosci 9:569–577
Shoham D, Glaser DE, Arieli A, Kenet T, Wijnbergen C, Toledo Y, Hildesheim R, Grinvald A (1999) Imaging cortical dynamics at high spatial and temporal resolution with novel blue voltage-sensitive dyes. Neuron 24:791–802
Sicard KM, Duong TQ (2005) Effects of hypoxia, hyperoxia, and hypercapnia on baseline and stimulus-evoked BOLD, CBF, and CMRO2 in spontaneously breathing animals. Neuroimage 25:850–858
Simard M, Arcuino G, Takano T, Liu QS, Nedergaard M (2003) Signaling at the gliovascular interface. J Neurosci 23:9254–9262
Simons DJ (1978) Response properties of vibrissa units in rat SI somatosensory neocortex. J Neurophysiol 41:798–820
Simons DJ, Carvell GE (1989) Thalamocortical response transformation in the rat vibrissa/barrel system. J Neurophysiol 61:311–330
Smith AJ, Blumenfeld H, Behar KL, Rothman DL, Shulman RG, Hyder F (2002) Cerebral energetics and spiking frequency: the neurophysiological basis of fMRI. Proc Natl Acad Sci USA 99:10765–10770
Sokoloff L, Reivich M, Kennedy C, Des Rosiers MH, Patlak CS, Pettigrew KD, Sakurada O, Shinohara M (1977) The [14 C]deoxyglucose method for the measurement of local cerebral glucose utilization: theory, procedure, and normal values in the conscious and anesthetized albino rat. J Neurochem 28:897–916
Somogyvari Z, Zalanyi L, Ulbert I, Erdi P (2005) Model-based source localization of extracellular action potentials. J Neurosci Methods 147:126–137
Srinivasan VJ, Sakadzic S, Gorczynska I, Ruvinskaya S, Wu W, Fujimoto JG, Boas DA (2009) Depth-resolved microscopy of cortical hemodynamics with optical coherence tomography. Opt Lett 34:3086–3088
Srinivasan VJ, Sakadzić S, Gorczynska I, Ruvinskaya S, Wu W, Fujimoto JG, Boas DA (2010a) Quantitative cerebral blood flow with optical coherence tomography. Opt Express 18(3): 2477–2494
Srinivasan VJ, Jiang JY, Yaseen MA, Radhakrishnan H, Wu W, Barry S, Cable AE, Boas DA (2010b) Rapid volumetric angiography of cortical microvasculature with optical coherence tomography. Opt Lett 35:43–45
Stefanovic B, Hutchinson E, Yakovleva V, Schram V, Russell JT, Belluscio L, Koretsky AP, Silva AC (2008) Functional reactivity of cerebral capillaries. J Cereb Blood Flow Metab 28:961–972
Strangman G, Culver JP, Thompson JH, Boas DA (2002) A quantitative comparison of simultaneous BOLD fMRI and NIRS recordings during functional brain activation. Neuroimage 17:719–731
Straub SV, Nelson MT (2007) Astrocytic calcium signaling: the information currency coupling neuronal activity to the cerebral microcirculation. Trends Cardiovasc Med 17:183–190
Takano T, Tian GF, Peng W, Lou N, Libionka W, Han X, Nedergaard M (2006) Astrocyte-mediated control of cerebral blood flow. Nat Neurosci 9:260–267
Takano T, Tian GF, Peng W, Lou N, Lovatt D, Hansen AJ, Kasischke KA, Nedergaard M (2007) Cortical spreading depression causes and coincides with tissue hypoxia. Nat Neurosci 10:754–762
Takashima I, Kajiwara R, Iijima T (2001) Voltage-sensitive dye versus intrinsic signal optical imaging: comparison of optically determined functional maps from rat barrel cortex. Neuroreport 12:2889–2894
Teasell R, Bayona NA, Bitensky J (2005) Plasticity and reorganization of the brain post stroke. Top Stroke Rehabil 12:11–26
Thompson JK, Peterson MR, Freeman RD (2003) Single-neuron activity and tissue oxygenation in the cerebral cortex. Science 299:1070–1072

Thomson AM, Bannister AP (2003) Interlaminar connections in the neocortex. Cereb Cortex 13:5–14

Tian P, Teng IC, May LD, Kurz R, Lu K, Scadeng M, Hillman EM, De Crespigny AJ, D'Arceuil HE, Mandeville JB, Marota JJ, Rosen BR, Liu TT, Boas DA, Buxton RB, Dale AM, Devor A (2010) Cortical depth-specific microvascular dilation underlies laminar differences in blood oxygenation level-dependent functional MRI signal. Proc Natl Acad Sci USA 107(34):15246–15251

Tsien RY (1981) A non-disruptive technique for loading calcium buffers and indicators into cells. Nature 290:527–528

Turner DA, Foster KA, Galeffi F, Somjen GG (2007) Differences in O2 availability resolve the apparent discrepancies in metabolic intrinsic optical signals in vivo and in vitro. Trends Neurosci 30:390–398

Ulbert I, Halgren E, Heit G, Karmos G (2001) Multiple microelectrode-recording system for human intracortical applications. J Neurosci Methods 106:69–79

Vakoc B, Yun S, de Boer J, Tearney G, Bouma B (2005) Phase-resolved optical frequency domain imaging. Opt Express 13:5483–5493

Vanzetta I, Grinvald A (1999) Increased cortical oxidative metabolism due to sensory stimulation: implications for functional brain imaging. Science 286:1555–1558

Vanzetta I, Grinvald A (2001) Evidence and lack of evidence for the initial dip in the anesthetized rat: implications for human functional brain imaging. Neuroimage 13:959–967

Vanzetta I, Hildesheim R, Grinvald A (2005) Compartment-resolved imaging of activity-dependent dynamics of cortical blood volume and oximetry. J Neurosci 25:2233–2244

Villringer A, Chance B (1997) Non-invasive optical spectroscopy and imaging of human brain function. Trends Neurosci 20:435–442

Viswanathan A, Freeman RD (2007) Neurometabolic coupling in cerebral cortex reflects synaptic more than spiking activity. Nat Neurosci 10:1308–1312

Wallace DJ, Zum Alten Borgloh SM, Astori S, Yang Y, Bausen M, Kugler S, Palmer AE, Tsien RY, Sprengel R, Kerr JN, Denk W, Hasan MT (2008) Single-spike detection in vitro and in vivo with a genetic Ca(2+) sensor. Nat Methods 5(9):797–804

Wang X, Lou N, Xu Q, Tian GF, Peng WG, Han X, Kang J, Takano T, Nedergaard M (2006) Astrocytic Ca(2+) signaling evoked by sensory stimulation in vivo. Nat Neurosci 9:816–823

White B, Pierce M, Nassif N, Cense B, Park B, Tearney G, Bouma B, Chen T, de Boer J (2003) In vivo dynamic human retinal blood flow imaging using ultra-high-speed spectral domain optical coherence tomography. Opt Express 11:3490–3497

White EL, DeAmicis RA (1977) Afferent and efferent projections of the region in mouse SmL cortex which contains the posteromedial barrel subfield. J Comp Neurol 175:455–482

Winship IR, Plaa N, Murphy TH (2007) Rapid astrocyte calcium signals correlate with neuronal activity and onset of the hemodynamic response in vivo. J Neurosci 27:6268–6272

Wise SP, Jones EG (1976) The organization and postnatal development of the commissural projection of the rat somatic sensory cortex. J Comp Neurol 168:313–343

Wojtkowski M, Bajraszewski T, Targowski P, Kowalczyk A (2003) Real-time in vivo imaging by high-speed spectral optical coherence tomography. Opt Lett 28:1745–1747

Woolsey TA, Rovainen CM, Cox SB, Henegar MH, Liang GE, Liu D, Moskalenko YE, Sui J, Wei L (1996) Neuronal units linked to microvascular modules in cerebral cortex: response elements for imaging the brain. Cereb Cortex 6:647–660

Xu F, Ge Y, Lu H (2009) Noninvasive quantification of whole-brain cerebral metabolic rate of oxygen (CMRO2) by MRI. Magn Reson Med 62:141–148

Yang SP, Krasney JA (1995) Cerebral blood flow and metabolic responses to sustained hypercapnia in awake sheep. J Cereb Blood Flow Metab 15:115–123

Yaseen MA, Srinivasan VJ, Sakadzic S, Wu W, Ruvinskaya S, Vinogradov SA, Boas DA (2009) Optical monitoring of oxygen tension in cortical microvessels with confocal microscopy. Opt Express 17:22341–22350

Yee SH, Lee K, Jerabek PA, Fox PT (2006) Quantitative measurement of oxygen metabolic rate in the rat brain using microPET imaging of briefly inhaled 15O-labelled oxygen gas. Nucl Med Commun 27:573–581

Zappe AC, Uludag K, Oeltermann A, Ugurbil K, Logothetis NK (2008) The influence of moderate hypercapnia on neural activity in the anesthetized nonhuman primate. Cereb Cortex 18: 2666–2673

Zhang N, Zhu XH, Lei H, Ugurbil K, Chen W (2004) Simplified methods for calculating cerebral metabolic rate of oxygen based on 17O magnetic resonance spectroscopic imaging measurement during a short 17O2 inhalation. J Cereb Blood Flow Metab 24:840–848

Zhu XH, Zhang N, Zhang Y, Zhang X, Ugurbil K, Chen W (2005) In vivo 17O NMR approaches for brain study at high field. NMR Biomed 18:83–103

Zonta M, Angulo MC, Gobbo S, Rosengarten B, Hossmann KA, Pozzan T, Carmignoto G (2003) Neuron-to-astrocyte signaling is central to the dynamic control of brain microcirculation. Nat Neurosci 6:43–50